

DTIC FILE COPY

2

GL-TR-90-0068

**NY-NEX Rayleigh Wave Signal and Noise Analysis at a
Seismic Array**

Christopher J. Center

Weston Observatory
Boston College
381 Concord Road
Weston, MA 02193

DTIC
ELECTE
DEC 24 1990
S D

12 March 1990

Scientific Report No. 4


approved for public release; distribution unlimited

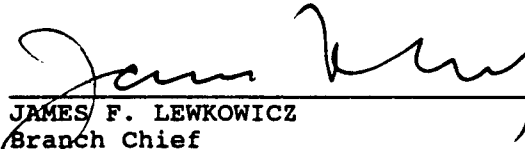
GEOPHYSICS LABORATORY
AIR FORCE SYSTEMS COMMAND
UNITED STATES AIR FORCE
HANSCOM AIR FORCE BASE, MASSACHUSETTS 01731-5000

AD-A230 137

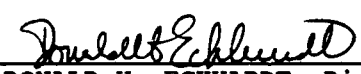
90 12 19 094

"This technical report has been reviewed and is approved for publication"


JAMES C. BATTIS
Contract Manager
Solid Earth Geophysics Branch
Earth Sciences Division


JAMES F. LEWKOWICZ
Branch Chief
Solid Earth Geophysics Branch
Earth Sciences Division

FOR THE COMMANDER


DONALD H. ECKHARDT, Director
Earth Sciences Division

This report has been reviewed by the ESD Public Affairs Office (PA) and is releasable to the National Technical Information Service (NTIS).

Qualified requestors may obtain additional copies from the Defense Technical Information Center. All others should apply to the National Technical Information Service.

If your address has changed, or if you wish to be removed from the mailing list, or if the addressee is no longer employed by your organization, please notify GL/IMA, Hanscom AFB, MA 01731. This will assist us in maintaining a current mailing list.

Do not return copies of this report unless contractual obligations or notices on a specific document requires that it be returned.

REPORT DOCUMENTATION PAGE

Form Approved
OMB No 0704-0188

Public reporting burden for this collection of information is estimated to average 1 hour per response, including the time for reviewing instructions, searching existing data sources, gathering and maintaining the data needed, and completing and reviewing the collection of information. Send comments regarding this burden estimate or any other aspect of this collection of information, including suggestions for reducing this burden, to Washington Headquarters Services, Directorate for Information Operations and Reports, 1215 Jefferson Davis Highway, Suite 1204, Arlington, VA 22202-4302, and to the Office of Management and Budget, Paperwork Reduction Project (0704-0188), Washington, DC 20503.

1. AGENCY USE ONLY (Leave blank) 2. REPORT DATE 3. REPORT TYPE AND DATES COVERED
90 Mar 12 August 1989-December 1989 Scientific#4

4. TITLE AND SUBTITLE 5. FUNDING NUMBERS
NY-NEX Rayleigh Wave Signal and Noise Analysis at a Seismic Array
PE62101F
PR7600
TA09
WUAG
Contract No:
F19628-86-C-0055

6. AUTHOR(S)
Christopher J. Center
7. PERFORMING ORGANIZATION NAME(S) AND ADDRESS(ES)
Weston Observatory
Boston College
381 Concord Road
Weston, MA 02193
8. PERFORMING ORGANIZATION
REPORT NUMBER

9. SPONSORING/MONITORING AGENCY NAME(S) AND ADDRESS(ES)
Geophysics Laboratory
Hanscom AFB, MA 01731-5000
Contract Manager: James C. Battis/LWH
10. SPONSORING/MONITORING
AGENCY REPORT NUMBER
GL-TR-90-0068

11. SUPPLEMENTARY NOTES

12a. DISTRIBUTION/AVAILABILITY STATEMENT 12b. DISTRIBUTION CODE
approved for public release;
distribution unlimited

13. ABSTRACT (Maximum 200 words)

Conventional frequency wave number - processing of array data was used to estimate the azimuths and phase velocities of fundamental mode Rayleigh waves in the geology and ambient noise setting at North Haverhill, New Hampshire. These estimates are compared to true azimuths between known shot to array site locations to determine the horizontal refraction of Rg waves due to the regional geology and the variation of azimuth and phase velocity estimates due to additive noise.

The analysis was based on calculations of the spectral density function $P(K_x, K_y, f)$, a measure of power as a function of frequency and wave number for propagating waves. This study measured 0.3 to 1.0 second period Rg waves with phase velocities ranging from 2.5 to 2.9 km/sec having refraction raypaths with a lateral velocity gradient.

14. SUBJECT TERMS 15. NUMBER OF PAGES
Seismic Analysis 112
Data Processing
16. PRICE CODE

17. SECURITY CLASSIFICATION OF REPORT 18. SECURITY CLASSIFICATION OF THIS PAGE 19. SECURITY CLASSIFICATION OF ABSTRACT 20. LIMITATION OF ABSTRACT
Unclassified Unclassified Unclassified Unclassified

	Contents
CHAPTER 1 INTRODUCTION	1
CHAPTER 2 REGIONAL GEOLOGY	4
2.0 INTRODUCTION	4
2.1 FORMATIONS	4
2.2 GEOLOGIC HISTORY	5
2.3 GEOPHYSICAL PROPERTIES	5
CHAPTER 3 DATA ACQUISITION	8
3.0 INTRODUCTION	8
3.1 SITE INFORMATION	8
3.2 RECORDING HARDWARE	12
3.2.1 Geophysical Data Acquisition System	12
3.2.2 Channel Calibration	14
3.2.3 Array Attributes (Array Calibration)	17
CHAPTER 4 NOISE	19
4.0 INTRODUCTION	19
4.1 NOISE TESTS	19
4.1.1 Test for Normality	20
4.1.2 Test for Stationarity	21
4.1.3 Summary of the Test Results	22
4.2 CHANNEL NOISE	23
4.2.1 Hardware Noise	23
4.2.2 Ambient Noise	23
4.2.3 Digital Noise	24
4.2.4 Summary	25



Availability Codes	
Dist	Avail and/or Special
A-1	

Contents

4.3	ARRAY NOISE	26
4.3.1	Spatial Noise of the Array	26
4.3.2	Ambient Noise of the Array	27
CHAPTER 5	RG WAVE AZIMUTH AND PHASE VELOCITY ESTIMATIONS USING AN ARRAY	29
5.0	INTRODUCTION	29
5.1	DATA PROCESSING	33
5.1.1	Frequency-Wavenumber Spectra	33
5.1.2	Azimuth and Phase Velocity	34
5.1.3	Spatial Coherence	35
5.1.4	Power Spectral Density Sum	35
CHAPTER 6	AZIMUTH AND PHASE VELOCITY RESULTS	37
6.0	INTRODUCTION	37
6.1	SHOT ANALYSIS	38
6.1.1	Shot 6	38
6.1.2	Shot 7	41
6.1.3	Shot 5	44
6.1.4	Shot 8	46
6.1.5	Shot 10	48
6.1.6	Summary	49
6.2	COMPARISON OF GROUP AND PHASE VELOCITY	51
CHAPTER 7	CONCLUSION	53

Appendices

APPENDIX A	THE POWER SPECTRAL DENSITY FUNCTION	56
B	SYMBOLS	58
C	REFERENCES	61

Tables

TABLE 1-1	SITE TO SHOT COORDINATES	3
2-1	NY-NEX VT - NH ROCK FORMATIONS	4
2-2	ROCK VELOCITIES AT 10 BARS PRESSURE	7
3-1	SHOT INFORMATION	10
3-2	SENSOR COORDINATES	11
3-3	SHOT RECORDS	13
3-4	LOW & HIGH GAIN CHANNEL PARAMETERS	16
3-5	DECIBEL CONTOUR LEVELS	18
4-1	GAUSSIAN DISTRIBUTION TEST	22
4-2	AMBIENT NOISE ARRAY RESULTS	28
6-1	SHOT 6 - LINEAR COMPARISONS	40
6-2	SHOT 7 - LINEAR COMPARISONS	43
6-3	SHOT 5 - LINEAR COMPARISONS	45
6-4	SHOT 8 - LINEAR COMPARISONS	47
6-5	ESTIMATION ERROR	49
6-6	AZIMUTHS AND PHASE VELOCITIES	50
6-7	GROUP VELOCITY MEASUREMENTS	52

Figures

FIGURE 1A	GEOLOGIC MAP FOR SHOTS 5, 6, AND THE WO ARRAY	63
1B	GEOLOGIC CROSS-SECTION FOR SHOTS 5, 6, AND THE WO ARRAY	64
2	GEOLOGIC MAP BETWEEN SHOT 7 AND THE WO ARRAY	65
3	NY-NEX SHOT LOCATION MAP	66
4	WO ARRAY TOPOGRAPHY	67
5A	NY-NEX LONG ARRAY COORDINATES	68
5B	NY-NEX SHORT ARRAY COORDINATES	68
6A	NY-NEX SPATIAL WINDOW FUNCTION FOR LONG ARRAY	68
6B	NY-NEX SPATIAL WINDOW FUNCTION FOR SHORT ARRAY	68
7	GDAS HARDWARE DIAGRAM	69
8	LOW AND HIGH GAIN CHANNEL RESPONSES	70
9	NEAR AND FAR SHOT NY-NEX GROUND MOTION	71
10	AMBIENT SEISMIC NOISE	72
11	STATIONARITY TEST	73
12	NORMALITY TEST	74
13	CHANNEL HARDWARE AND AMBIENT SEISMIC NOISE	75
14	PROTECTION RATIO	76
15	QUANTIZATION NOISE	77
16	AMBIENT SEISMIC NOISE OF FREQUENCY-WAVENUMBER SPECTRA	78
17	CONVENTIONAL FREQUENCY-WAVENUMBER SPECTRUM	79
18	COMPARISONS OF WIDEBAND ANALYSIS METHODS	80
19A	SHOT 6 - RAW TIME SERIES	82

FIGURE 19B SHOT 6 - FILTERED TIME SERIES	83
19C SHOT 6 - PSD	84
19D SHOT 6 - SPATIAL COHERENCE, SUM, $c(f)$, $\Phi(f)$	85
20A SHOT 7 - RAW TIME SERIES	86
20B SHOT 7 - FILTERED TIME SERIES	87
20C SHOT 7 - PSD	88
20D SHOT 7 - SPATIAL COHERENCE, SUM, $c(f)$, $\Phi(f)$	89
21 AZIMUTH AND VELOCITY CHANGES AT A BOUNDARY	90
22A SHOT 5 - RAW TIME SERIES	91
22B SHOT 5 - FILTERED TIME SERIES	92
22C SHOT 5 - PSD	93
22D SHOT 5 - SPATIAL COHERENCE, SUM, $c(f)$, $\Phi(f)$	94
23A SHOT 8 - RAW TIME SERIES	95
23B SHOT 8 - FILTERED TIME SERIES	96
23C SHOT 8 - PSD	97
23D SHOT 8 - SPATIAL COHERENCE, SUM, $c(f)$, $\Phi(f)$	98
24A SHOT 10 - RAW TIME SERIES	99
24B SHOT 10 - FILTERED TIME SERIES	100
24C SHOT 10 - PSD	101
24D SHOT 10 - STACK PSD, PSD SUM, $c(f)$, $\Phi(f)$	102
25 RAYPATH GEOGRAPHY	103
26 PHASE VELOCITY DISPERSION	104
27 GROUP VELOCITY DISPERSION	104

1 INTRODUCTION

This thesis concentrates on the processing of seismic data acquired as part of the New York-New England Experiment (NY-NEX) conducted from September 17, 1988 to September 29, 1988. NY-NEX was a joint venture of the United States Air Force, the United States Geological Survey (USGS) and the Geological Survey of Canada (GSC) to measure the seismic velocity structure of the earth's crust and to test seismic methods that could be used to verify nuclear test ban treaties with the Soviet Union. This thesis is appropriate for test ban treaty research because the geology of the experiment area is analogous to that found in the Soviet Union.

NY-NEX was a long range seismic refraction profile experiment that consisted of 23 chemical explosions (shots) located at sites in southern Ontario, northern New York, Vermont, New Hampshire, and central Maine. Each of the shots was buried and consisted of either 2000 or 3000 pounds of explosives with the exception of the easternmost shot which was 6000 pounds.

The seismic analysis described in this thesis is focused on estimating azimuths and phase velocities of crustal, fundamental mode Rayleigh waves (Rg waves) generated by the NY-NEX shots in a frequency range of 0.6 to 3.3 Hz. Rg wave azimuths and phase velocities were measured by an array of seismic sensors and compared to the azimuths and group velocities calculated from known shot and site coordinates (listed in Table 1-1). Rg waves are short-period, fundamental mode, dispersive Rayleigh surface waves that propagate along a free surface with an elliptical particle motion. The particle displacement $u(x,y,z,t)$ of a fundamental mode plane surface wave propagating in the x-y plane is mathematically represented in cartesian coordinates [1] by

$$u(x,y,z,t) = A(z) \exp[j(K_x x + K_y y - \omega t)] \quad (1)$$

where K_x and K_y are the wavenumbers in the x and y directions, ω is the angular

frequency ($\omega = 2\pi f$, where f is the frequency), t is time, and $A(z)$ is the amplitude as a function of depth and frequency. Rg wave velocities vary according to the elastic constants and densities in the near surface layers. For shallow shots in New England, Kafka [2] has shown that Rg waves travel within a group velocity range of 1.9 to 3.4 km/sec in the 0.6 to 3.3 Hz band. The group velocity $U(f)$ is related to the wavenumber K and the phase velocity $c(f)$ by

$$U(f) = R/(t_1 - t_0) = \Delta\omega/\Delta K \approx d\omega/dK \quad (2)$$

and

$$c(f) = \Delta R/(t_m - t_n) = \omega/K \quad (3)$$

where R is the distance from shot (origin time t_0) to site (arrival time t_1), and ΔR is the distance from sensor n (arrival time t_n) to sensor m (arrival time t_m). The frequency-wavenumber (F-K) power spectral density function $P(K_x, K_y, f)$, computed from group-velocity windows of the Weston Observatory (WO) array data, was used to determine the directional and phase velocity characteristics of Rg waves generated from the NY-NEX shots. $P(K_x, K_y, f)$ measures power as a function of frequency and wavenumber for propagating waves and can be used to estimate azimuth and phase velocity. Deviations of the wave direction from the great-circle source azimuth is explained by (a) lateral heterogeneity in the shallow crust along the path between shot and receiver and (b) the effects of additive noise on those estimates.

Table 1-1

SITE TO SHOT COORDINATES

SHOT	EL. (m)	LATITUDE N			LONGITUDE W			DEGR	RANGE (km)	AZIMUTH (deg)
1	95	44	35	24.56	69	44	45.94	1.70	189.26	71.74
2	122	44	33	47.67	70	2	40.32	1.49	165.74	70.34
3	277	44	27	32.23	70	31	21.58	1.13	126.00	60.89
4	317	44	24	41.15	70	58	10.52	0.82	90.86	65.68
5	516	44	20	10.35	71	23	5.88	0.52	57.45	60.01
6	329	44	16	50.40	71	49	52.61	0.24	26.40	32.43
7	460	44	10	42.46	72	14	11.49	0.19	21.33	301.20
8	433	44	9	2.80	72	34	35.72	0.42	46.19	280.15
9	671	44	4	24.56	72	55	57.31	0.67	74.08	268.83
10	35	44	3	13.01	73	23	11.30	0.99	110.47	269.84
11	287	43	59	31.94	73	39	40.10	1.20	133.11	266.35
12	535	43	56	15.55	73	58	57.60	1.43	159.39	265.04
13	524	43	58	4.65	74	15	41.37	1.63	181.37	266.81
14	530	43	59	58.14	74	29	15.95	1.79	199.22	268.38
15	427	44	9	20.22	75	00	56.46	2.17	241.20	273.06
16	175	44	14	38.04	75	31	42.12	2.54	282.49	274.94
17	94	44	17	49.47	75	55	32.82	2.83	314.48	275.77
18	140	44	18	4.74	76	43	6.35	3.40	377.73	275.39
19	180	44	20	6.63	77	12	16.10	3.75	416.64	275.72
20	600	44	28	37.96	77	39	29.64	4.08	453.55	277.56
21	710	43	3	24.89	72	56	17.23	1.23	136.23	213.88
22	325	43	14	9.91	71	51	32.04	0.85	94.46	172.60
23	79	43	26	56.83	70	40	18.55	1.16	128.45	122.57

The Weston Observatory (WO) NY-NEX array was located in North Haverhill, NH with its center at latitude 44° 04' 45.2" (44.07922°), longitude 72° 00' 30.7" (72.00853°).

2 REGIONAL GEOLOGY

2.0 INTRODUCTION

The WO NY-NEX array was located at the Dean Memorial Airport in North Haverhill, New Hampshire. Since the area is flat, the array analysis can be confined to the x-y coordinates. The earth below the array is made up of a thick overburden of glacial drift and alluvium. Van Diver [3] describes the bedrock geology in the area as characteristic of metamorphosed sedimentary and volcanic rocks resulting from igneous activity. Figures 1A, 1B, and 2 show the large scale folds, faults, and contacts in the region as having a north-northeast trend.

2.1 FORMATIONS

The French Pond granitic (fpgc) intrusion is north of the WO NY-NEX array (see Figure 1A). Several other formations that lie between the NY-NEX shots and the array site are the Albee (Oal), Bethlehem gneiss (bg), Gile Mountain (Og), Meetinghouse Slate (Om), Waits River (Ow), and the Ammonoosuc Volcanics (Oam). Table 2-1 describes the formations and their thicknesses (where known) of rocks between the NY-NEX shots and the WO receivers. The cross-section in Figure 1B also shows these bed thicknesses and relative dips in the region.

<u>Table 2-1</u>		<u>NY-NEX VT - NH ROCK FORMATIONS</u>	
FORM DESCRIPTION		THICK (km)	
bg	Granodiorite or quartz monzonite	--	
fpgc	Porphyritic to coarse grain pink biotite granite	--	
Oal	Feldspathic quartzite in chlorite zone	1.5	
Oam	Soda-rhyolite and chlorite schist	2.5	
Og	Gradational mica schist to quartz-mica schist	2.0	
Om	Thinly bedded mica and quartz-mica slate & schist	0.8	
Ow	Interbedded calcareous and non-calcareous schists	3.0	

2.2 GEOLOGICAL HISTORY

The geologic history of surface rocks in the study area began in the Middle Ordovician with deposition of the Waits River, Gile Mountain, Meetinghouse, and Albee formations [4]. Minor deformation of these rocks resulted from the Taconic orogeny. This deformation is noticeable in areas such as Littleton, NH, where Silurian rocks rest unconformably on top of pre-Silurian rocks. Major tectonic deformation during the Middle Devonian occurred in the Acadian Orogeny, resulting in the folding, faulting, metamorphism, and numerous igneous intrusions such as the French Pond granite (fpgc). The middle Ordovician Meetinghouse slate and Gile Mountain formations of Vermont are separated from the Silurian to middle Devonian Albee formation of New Hampshire by the north-northeast trending Monroe fault [4]. East of the Monroe fault lies the Ammonoosuc thrust fault that dips 36°W. The Ammonoosuc thrust fault establishes the contact between the New Hampshire Albee formation and the Ammonoosuc Volcanics.

Recent geologic changes are attributed to glaciation and stream erosion. Wisconsin glaciation (18,000 to 20,000 years ago) has the only lasting glacial effect on the geomorphology. This glacial erosion is seen in the rounded valleys and carved flanks of the Presidential Range. Stream erosion is mostly attributed to the Connecticut River which winds through the Ordovician Albee formation (Oal).

2.3 GEOPHYSICAL ROCK PROPERTIES

The regional Rayleigh wave velocity estimates (V_r) for rocks in the formations located between NY-NEX shot and WO receiver points are listed in Table 2-2. Rayleigh wave velocities (V_r), listed in Table 2-2, were calculated from the equations

$$V_r = 0.9194 V_s \quad (4)$$

and

$$V_s = V_p/\sqrt{3} \quad (5)$$

where V_p and V_s are the compressional and shear wave velocities. Equations (4) and (5) are based on a Poisson's ratio of 0.25 and are further discussed by Sheriff et al. [5]. These estimates of V_r provide a velocity comparison between rock formations. Their calculations are based a model where the travel path is along the surface (zero depth) of a homogeneous medium (which does not exhibit dispersion [5]). Values for V_p and V_s were found in the Handbook of Physical Constants [6]. The handbook estimates a quality factor (Q) for rocks in the region ranging between 125 and 314, which is characteristic of the higher attenuation levels found in igneous and metamorphic rocks.

To find the relationship between the rock formations and the rock velocities surrounding the WO array, seismic velocities for the bg, fpgc, Oal, Oam and Ow formations were estimated using Tables 2-1 and 2-2. The first significant formation is southeast of the array and is bg; it is composed of granodiorite and is assumed to have a velocity V_r of 2.3 km/sec. The fpgc intrusion to the north of the array mostly consists of granite and therefore is assumed to have a velocity V_r of 2.7 km/sec. The Og formation is dominated by schist and quartz-mica schist and is thought to have a velocity V_r of 3.0 km/sec. Oal is assumed to have a velocity V_r of about 3.0 km/sec since it is composed of the quartzite and chlorite schist rocks listed in Table 2-2. Oam is in the chlorite zone and expected to be a low velocity layer with a V_r of about 2.5 km/sec.

Rg wave group velocities in the NY-NEX study area are therefore expected to be in the range of 2.5 to 3.0 km/sec, characteristic of the high velocity metamorphic and igneous formations in the area. For example, Figure 2 shows the geologic structure between shot 7 (West Groton, Vt) and the WO array consisting of a cross-section of the Ow, Og, Om, and Oal formations. The Rg rock velocities for these formations are

expected to be in the range of 2.5 to 3.0 km/sec.

Table 2-2

ROCK VELOCITIES AT 10 BARS PRESSURE

Rock	Vp (km/sec)	Vs (km/sec)	Vr (km/sec)	Measure Area
Alluvium	0.5-2.0	0.3-1.2	0.3-1.1	-----
Glacial till	0.4-1.0	0.2-0.6	0.1-0.6	-----
Granite	5.1	2.9	2.7	Barre, Vt
Granodiorite, gneiss	4.4	2.5	2.3	Bethlehem, NH
Chlorite Schist	4.8	2.8	2.5	Chester Quarry Vt
Quartzite	---	4.0	3.7	-----
Slate	5.5	3.2	2.9	Medford, Ma

Vr is the Rayleigh wave velocity along the surface
(zero depth) of an isotropic, homogeneous medium.

3 DATA ACQUISITION

3.0 INTRODUCTION

Shot times for the NY-NEX experiment were restricted to the early morning hours to take advantage of the low background seismic noise conditions resulting from lulls in cultural activity and benign weather patterns. The seismic profile encompassed three nights of shot sequences. These shot sequences were separated on each night by a 1.0 to 1.5 hour interval. Each shot sequence consisted of four or five shots at different locations exploded at two or three minute intervals. Each night of shooting was followed by a three to four day rest period. Table 3-1 lists the NY-NEX shot sizes, shot times, and shot locations. A geographic map of the shot locations is shown in Figure 3.

All of the shot sequences were digitally recorded on magnetic tape and transferred to WO where they were divided into two minute windows for data analysis. Each window begins at the shot time. A pre-shot window containing ambient seismic noise was also recorded prior to each shot sequence.

3.1 SITE INFORMATION

The WO NY-NEX array was located approximately 2 km southeast of North Haverhill, New Hampshire at the Dean Memorial Airport (see Figure 4). The geographic coordinates of the center of the array was located at latitude 44.07923° ($44^{\circ} 04' 45.2''\text{N}$) and longitude 72.00852° ($72^{\circ} 00' 30.7''\text{W}$).

The variably spaced NY-NEX array was designed to suppress ambient seismic noise and to capture a wide velocity range of NY-NEX seismic signals. The shape of the array represents a compromise between maintaining linear legs in the array and using available airport grounds for sensor planting. Two array configurations were used to record NY-NEX signals. Sensor coordinates for these configurations are listed in Table 3-2 and

shown in Figures 5A and 5B. The only difference between the two arrays is that in the "short" array (Figure 5B) sensor #1 was moved 106.6 meters (m) closer to sensor #2. This change was made to reduce wind noise generated by the line of trees next to the sensor at the north end of the airfield. Most of the seismic sensors were buried on level ground at 173.7 m above sea level with the exception of channels 14 and 15 which were buried at elevations of 170.7 m and 164.6 m above sea level as listed in Table 3-2 and shown in Figure 4. The center of the array was located at the 3-component station of channels 7, 8 and 9. Channels 1-7 and 10-15 define the two main legs of the array. Channels 1-7 comprised the N 8° 1' W leg of the array. Channels 10-15 comprised the N 69° 26.5' W leg of the array. Channel 16 bisected the angle between the two legs and was 69.5 m from the center of the array (see Figures 5A and 5B). The placement of sensor 16 was based on the analysis of a series of spatial window function models. The spatial window function (see Section 3.2.3) for the final array pattern is shown in Figure 6.

Table 3-1

SHOT INFORMATION

JULIAN DAY	TIME (HHMM)	SHOT	SIZE (lbs)	SHOT LOCATION
261	0400	2	2000	Farmington Falls, ME
261	0402	5	2000	Jefferson Notch, NH
261	0404	7	3000	West Groton, NH
261	0406	22	2000	Warner, NY
261	0408	14	3000	Long Lake, NY
261	0600	6	2000	Littleton, NH
261	0602	4	2000	Gilead, ME
261	0604	1	6000	Waterville, ME
261	0800	3	2000	Mount Zircon, ME
261	0802	23	2000	Sanford, ME
261	0804	10	3000	West Addison, VT
268	0400	8	2000	Barre West, VT
268	0402	9	2000	Lincoln Gap, VT
268	0404	12	2000	Newcomb, NY
268	0406	22	2000	(repeat)
268	0408	20	3000	Marmora, Ontario
268	0600	7	3000	(repeat)
268	0602	17	3000	Alexandria Bay, NY
268	0604	13	2000	Newcomb, NY
268	0606	10	2000	(repeat)
268	0800	14	3000	(repeat)
268	0802	11	2000	North Hudson, NY
268	0804	21	2000	Londonderry, VT
268	0806	4	3000	(repeat)
274	0400	20	2000	(repeat)
274	0402	18	2000	Sharpton, Ontario
274	0404	17	500	(repeat)
274	0406	14	3000	(repeat)
274	0600	19	2000	Lime Lake, Ontario
274	0602	16	2000	Fort Drum, NY
274	0604	15	2000	Star Lake, NY
274	0606	10	3000	(repeat)

All shots occurred within 0.015 seconds of the listed Greenwich Mean Time (GMT).

Table 3-2

SENSOR COORDINATES

<u>CHANNEL</u>	<u>SERIAL</u> <u>NUMBER</u>	<u>X-LOC</u> <u>(m)</u>	<u>Y-LOC</u> <u>(m)</u>	<u>Z-LOC</u> <u>(m)</u>	<u>RANGE</u> <u>(m)</u>
1	363Z	-62.5	443.6	173.7	448.0
2	347Z	-33.7	239.0	173.7	241.4
3	349Z	-18.1	128.2	173.7	129.5
4	366Z	-9.7	68.8	173.7	69.5
5	279Z	-5.2	36.9	173.7	37.3
6	322Z	-2.8	19.8	173.7	20.0
7	348Z	0.0	0.0	173.7	0.0
8	257N	0.0	0.0	173.7	0.0
9	258E	0.0	0.0	173.7	0.0
10	278Z	-18.7	7.0	173.7	20.0
11	367Z	-34.9	13.1	173.7	37.3
12	356Z	-65.1	24.4	173.7	69.5
13	321Z	-121.3	45.5	173.7	129.5
14	319Z	-226.0	84.8	170.7	241.4
15	346Z	-391.7	119.9	164.6	341.4
16	362Z	-43.9	53.8	173.7	69.5

Position change of channel 1 on day 267 at 1900 hours

<u>CHANNEL</u>	<u>SN</u>	<u>X-LOC</u>	<u>Y-LOC</u>	<u>Z-LOC</u>	<u>RANGE</u>
1	363Z	-47.6	338.1	173.7	341.4

The NY-NEX array center (channel 7,8,9) was located at latitude 44° 4' 45.2" (44.07922°) and longitude 72° 00' 30.7" (72.00853°). X-LOC, Y-LOC, and Z-LOC represent the distance north, east, and depth of the sensor positions from the array center.

3.2 RECORDING HARDWARE

3.2.1 Geophysical Data Acquisition System

The Geophysical Data Acquisition System (GDAS) developed at WO provided the hardware [7] and software [8] to record, store, and process 16 channels of data from the NY-NEX experiment. GDAS is a stand-alone system based on Digital Equipment Corporation's Q-bus^T microcomputer. The 18-bit Q-bus supports the LSI-11/23^T microprocessor used for data processing and interrupt-driven data acquisition. Digitized data were stored on floppy disks and 9-track magnetic tapes for further (in-house) data analysis. A 15-bit analog-to-digital converter (A/D) digitizes analog filtered sensor data. A diagram of the GDAS computer is presented in Figure 7. For the NY-NEX experiment, a filter card for each channel consisted of a 6-pole low-pass butterworth filter at 34.3 Hz and a 2-pole low-pass butterworth filter at 100.0 Hz. Filter cards contained a hardware modified gain that was set at a high or low level according to the shot to receiver distance (see Table 3-3). The roll-off of the butterworth filter for the low and high gain filter cards is presented in the system transfer function (channel response) plots shown in Figure 8. The GDAS field unit was hardware switch selected to record data at a 100 Hz sample rate.

The WO NY-NEX array deployed 2 horizontal and 14 vertical Electro-tech EV-17 short-period (1 Hz) seismometers featuring an inclined spring suspension with a moving magnet mass of 2760 g. The seismometers have a nominal sensitivity of 8.8 volts/mm/sec. Ground motions were converted by the seismometers into voltages which were transmitted to the preamplifiers. These preamplifiers conditioned the signals to desired levels and transmitted them to the analog filter cards.

^T Q-bus and LSI-11/23 are trademarks of Digital Equipment Corporation.

Table 3-3SHOT RECORDS

SHOT	SIZE (lb)	TIME (GMT)	FILE NAME	GAIN	ARRAY SIZE	SHOT DATE
3	2000	261 08 00	W3D61B	HIGH	LONG	17-SEP-88
4A	2000	261 06 02	W2D61C	LOW	LONG	17-SEP-88
4B	3000	268 08 06	W3D68E	HIGH	SHORT	24-SEP-88
5	2000	261 04 02	W1D61C	LOW	LONG	17-SEP-88
6	2000	261 06 00	W2D61B	LOW	LONG	17-SEP-88
7A	3000	261 04 04	W1D61D	LOW	LONG	17-SEP-88
7B	3000	268 06 00	W2D68B	LOW	SHORT	24-SEP-88
8	2000	268 04 00	W1D68B	HIGH	SHORT	24-SEP-88
9	2000	268 04 02	W1D68C	HIGH	SHORT	24-SEP-88
10A	3000	261 08 04	W3D61D	HIGH	LONG	17-SEP-88
10B	2000	268 06 06	W2D68E	LOW	SHORT	24-SEP-88
10C	3000	274 06 06	W2D74E	LOW	SHORT	29-SEP-88
11	2000	268 08 02	W3D68C	HIGH	SHORT	24-SEP-88
12	2000	268 04 04	W1D68D	HIGH	SHORT	24-SEP-88
13	2000	268 06 04	W2D68D	LOW	SHORT	24-SEP-88
14A	3000	261 04 08	W1D61F	LOW	LONG	17-SEP-88
14B	3000	268 08 00	W3D68B	HIGH	SHORT	24-SEP-88
14C	3000	274 04 06	W1D74E	HIGH	SHORT	29-SEP-88
21	2000	268 08 04	W3D68D	HIGH	SHORT	24-SEP-88
22A	2000	261 04 06	W1D61E	LOW	LONG	17-SEP-88
22B	2000	268 04 06	W1D68E	HIGH	SHORT	24-SEP-88
23	3000	261 08 02	W3D61C	HIGH	LONG	17-SEP-88

A table of data analyzed within a NY-NEX shot to WO array site range of 200 km.

The filtered outputs were transmitted to the A/D where they were multiplexed, digitized, and stored. This process is illustrated in the following diagram for each of the digitized signals by

$$g(t) + n(t) \rightarrow \text{SENSOR} \rightarrow \text{PREAMPLIFIER} \rightarrow \text{FILTER} \rightarrow \text{A/D} \rightarrow s(nt)$$

where $g(t) + n(t)$ represents the analog recorded signal plus noise at the sensor and $s(nt)$ is the digitized recorded signal at the sampling interval nt . The sampling sequence of the signal is represented mathematically by

$$s(nt) = p(nt) [g(t) * h(t)] \quad (6)$$

where $*$ is the symbol for convolution, $p(nt)$ is defined as the digitizer or the Dirac comb function, and $h(t)$ is the time domain representation of the channel response (further discussed in Section 3.3.2). Typical examples of both raw and filtered ground motions $g(nt) + n(nt)$ recorded by the NY-NEX array are shown in Figure 9.

3.2.2 Channel Calibration

Channel calibration procedures are used to describe the system mathematically in terms of a system transfer function. In this thesis, the system transfer function is identified for each channel as the combined measurement of seismometer, preamplifier, and analog filter card electronics. Since the system transfer function includes the sensor electronics, it is herein referred to as the channel response.

The first step in system calibration is the application of a step in electric current (generated by the digital to analog converter) to the seismometer calibration coil. This causes an equivalent weight lift. The output (calibration) wavelet due to this "weight lift" is recorded by GDAS. This procedure is represented mathematically for the seismometer in terms of equivalent force F by

$$F = Ma = mg = Gi \quad (7)$$

where M is the mass of the seismometer weight, a is the acceleration of the seismometer weight, m is the calibration mass, g is gravity (9.81 m/sec^2), G is the motor constant, and i is the calibration current.

The second step in system calibration is to match the calibration wavelet with a computer generated second order seismometer model (of known electronics) with a gain, phase, and damping coefficient [8]. A match is selected when the sum of squared errors (SSE) between the model wavelet and the calibration wavelet is less than 0.001, or when the ambient noise in the calibration wavelet is less than the residual (SSE between the model and calibration wavelet) value.

Calibration measurements were performed on site during GDAS operation for both the low and high gain filter card electronics. To improve channel calibration wavelet estimates, several calibration tests were recorded and averaged for the low and high gain electronics. The low and high gain channel responses are listed in Table 3-4 and shown in Figure 8 for the NY-NEX site. The amplitude response is constant to ground particle velocity in the 2.0 to 30.0 Hz range. At frequencies greater than 30.0 Hz, there is a sharp fall-off in the channel response due to the analog filter.

Table 3-4

LOW GAIN CHANNEL PARAMETERS

CHANNEL	POLE FREQUENCY (Hz)	DAMPING (%)	MODEL Amplitude Ratio
1	0.932129	0.690000	-68.0309
2	0.969772	0.648438	-68.4867
3	1.010064	0.613281	-57.2372
4	0.937192	0.669531	-66.0749
5	0.956557	0.71875	-76.4375
6	0.947685	0.683594	-71.2204
7	0.943213	0.739844	-78.0973
8	0.996625	0.641406	-67.0136
9	0.977805	0.641406	-66.6782
10	0.97739	0.627344	-65.652
11	0.958049	0.704688	-65.464
12	0.939770	0.725781	-75.6339
13	0.939239	0.71875	-76.5301
14	0.926679	0.746875	-80.7887
15	0.926619	0.697656	-71.6362
16	0.929452	0.6625	-68.1599

HIGH GAIN CHANNEL PARAMETERS

CHANNEL	POLE FREQUENCY (Hz)	DAMPING (%)	MODEL Amplitude Ratio
1	0.937668	0.693262	-141.4317
2	0.969542	0.640527	-140.8091
3	1.009143	0.610000	-119.7630
4	0.934152	0.657227	-136.7298
5	0.956689	0.718750	-159.2683
6	0.940968	0.662500	-146.9642
7	0.935248	0.725000	-162.6823
8	1.008804	0.655469	-141.8040
9	0.985984	0.662500	-141.4921
10	0.974676	0.606250	-134.2870
11	0.953672	0.698535	-135.1754
12	0.938281	0.720000	-156.7691
13	0.936970	0.695000	-156.4051
14	0.931250	0.750000	-168.0947
15	0.927178	0.687500	-148.5644
16	0.924888	0.649316	-140.0599

3.2.3 Array Attributes (Array Calibration)

The spatial window function $|B(K)|^2$, also referred to as the beamforming array response, was calculated as the magnitude of the spatial transform of the array pattern's response to a unit impulse of infinite phase velocity. A continuous array response is calculated by

$$B(K_x, K_y; t) = \int_{-\infty}^{\infty} \int_{-\infty}^{\infty} w(x, y) \exp[-j(K_x x + K_y y)] dx dy \quad (8)$$

Equation (8) for an array of NS sensors with wavenumbers K_x and K_y is digitally represented at sensor locations m and n by

$$B(K_x, K_y; t) = 1/NS^2 \sum_{m,n=1}^{NS} W_{mn} \exp[-j(K_x(x_n - x_m) + K_y(y_n - y_m))] \quad (9)$$

The weight function W_{mn} in Equation (9) allows weighting for array optimization [9,10,11,12]. Weighting is itself a unique venture of finding the correct sensor weighting to optimize azimuth and phase velocity estimation and is not exploited in this thesis. For a uniformly weighted function of $W_{mn}=1$, the spatial window function $|B(K)|^2$ is calculated using

$$B(K_x, K_y; t) = |1/NS \sum_{n=1}^{NS} \exp[-j(K_x x_n + K_y y_n)]|^2 \quad (10)$$

Figures 6A and 6B show the uniformly weighted spatial window functions for the two NY-NEX array patterns. The data are displayed over a wavenumber range of ± 0.1 rad/m with contour steps in decibels (db) calculated by $-10\log[|B(K)|^2]$, where $|B(K)|^2$ has been normalized by its maximum. Table 3-5 provides insight into the relation between db and the percentage of the maximum normalized beamforming array response.

The beams shown in Figures 6A and 6B will optimally detect waves from the NW and SW directions. Rg wave azimuth and phase velocity are shown in Section 5.1.2 to

be calculated from the K_x and K_y values where $P(K_x, K_y, f)$ is a maximum.

<u>Table 3-5</u>		<u>DECIBEL CONTOUR LEVELS</u>	
	<u>Decibels</u>		<u>% of Maximum</u>
	0.00		100.00
	0.25		94.41
	0.50		89.13
	1.00		79.43
	2.00		63.10
	3.00		50.12
	4.00		39.81
	5.00		31.62
	6.00		25.12
	7.00		19.95

4 NOISE

4.0 INTRODUCTION

All unwanted recorded information is defined here as noise. Noise includes digitization error, aliasing, GDAS electronic noise, ambient seismic motion (microseisms), scattered refractions, and in this thesis, all that is not the Rg wave.

Ambient ground motion may be defined as the sum of independent random seismic events. Random events may be described as noise generated by vehicles, animals, and all random electronic noise not described by the channel response. Typical noise levels recorded during pre-shot windows are shown in Figure 10. Noise can be described both at a point (seismometer) and that which is passed by the array. Random noise is classified by its stationarity, normality, and spectra. Microseismic activity is found to exhibit the attributes of a stationary Gaussian random process.

Aki and Richards [1] state that the scatter in phase velocity measurement is due to lateral heterogeneity and ambient seismic noise. Aki and Richards [1] define the root-mean-square (RMS) phase velocity measurement error between two sensors that share the same signal and noise as

$$\Delta c_{rms}/c = 1/(2\pi) |N(f)| / |S(f)| (\lambda/\Delta x) \quad (11)$$

and the corresponding azimuth measurement error as

$$\Delta \Phi_{rms} = 1/\sqrt{2} |N(f)| / |S(f)| \quad (12)$$

where $|N(f)|$ is the amplitude spectra of the noise, $|S(f)|$ is the amplitude spectra of the signal, λ is the wavelength, and Δx is the distance between seismic stations.

4.1 NOISE TEST

The Gaussian probability distribution function was used to test the normality of the data in the NY-NEX pre-shot ambient noise windows. For noise to be classified as

stationary, it must be independent of time. The Sax test [13] for a stationary normal process was used to test the behavior of the ambient noise data.

4.1.1 Test for Normality

The central limit theorem states that the sum of a number of random independent variables has a distribution which approaches a Gaussian function as the number of variables becomes large. Mathematically, a random variable x described as a sum of random independent events r_i

$$x = r_1 + r_2 + r_3 + r_4 + \dots + r_m \quad (13)$$

will approach a Gaussian distribution function as the number of contributions becomes large [14]. Its probability density function $p(x)$ is

$$p(x) = 1/[\sigma\sqrt{2\pi}] \exp[-(x-\mu)^2/(2\sigma^2)] \quad (14)$$

where μ is the mean of x and σ is the standard deviation. Distributions of pre-shot ambient seismic motion were plotted on probability paper (as shown in Figure 12) to determine if the noise was distributed as a normal Gaussian process. The advantage of the probability paper is that it transforms the distribution of the Gaussian variate x' into a straight line [15], and the test becomes one of accepting a linear fit. The test data are based on calculating the variate x' by inversely solving Equation (15)

$$y = P(x') = \text{Prob}(x \leq x') = \int_{-\infty}^{x'} p(x) dx \quad (15)$$

for x' ,

$$x' = P^{-1}(y) \quad (16)$$

$P(x')$ is the probability that the random variable x is less than or equal to the variate x' . The distributions were computed by dividing observations in the ambient noise window into 128 equal histogram bins (class intervals).

4.1.2 Test for Stationarity

For stationary Gaussian noise, spectral coefficients in a narrow band are distributed as a Rayleigh density function (exponential probability function)

$$p(x) = x/(c^2) \exp[-x^2/(2c^2)] \quad \text{for } x \geq 0 \quad (17)$$

where c is a constant such as the standard deviation σ . Sax [13] showed that the probability of a Power Spectral Density (PSD) measurement in a band E of Gaussian noise between E and $E+dE$ is described by the exponential

$$P(E)dE = \exp(-\bar{E}/E) dE \quad (18)$$

which follows the Rayleigh distribution function

$$\int_{-\infty}^E P(E)dE = \int_{-\infty}^E \exp[-x^2/(2c^2)] \quad (19)$$

A linear trend in the graph identifies the noise as stationary and Gaussian. For the test, spectral coefficients were generated at frequencies in the 0.6 to 3.3 Hz band (the band where the Rg wave is known to occur). These coefficients, or observations, were plotted as linear energy (volts²/Hz) versus logarithmic frequency of occurrence (transformed scores) as shown in Figure 11. The spectral coefficients were generated by calculating 34 fast Fourier transforms (FFT's) of 128 individual samples (plus 128 zero pads - see Appendix A) in the same ambient seismic noise window used in Table 4-1. Spectral coefficients were gathered at frequencies in the 0.6 to 3.3 Hz band and distributed as a cumulative process.

4.1.3 Summary of the Test Results

Table 4-1 summarizes the Gaussian distribution test calculated for four individual pre-shot ambient noise windows. Table 4-1 identifies some sensors within the array as non-Gaussian. The non-Gaussian distributions of channels 14 and 15 are probably the result of these channels being close to the trees. The non-Gaussian distributions are probably due to an increase in the wind level, as seen when comparing the amplitude levels of channels 3 and 14 in Figure 12.

<u>Table 4-1</u>		<u>GAUSSIAN DISTRIBUTION TEST</u>													
		<u>CHANNELS</u>													
<u>FILE</u>		<u>1</u>	<u>2</u>	<u>3</u>	<u>4</u>	<u>5</u>	<u>6</u>	<u>7</u>	<u>10</u>	<u>11</u>	<u>12</u>	<u>13</u>	<u>14</u>	<u>15</u>	<u>16</u>
W1D61A		x	x	x	x	x	x	x	x	x	x	x		x	x
W2D61A		x	x	x	x		x	o	x		x	x		o	
W2D68A		x	x	x	x	x	x	x	x	x		x	x	x	o
W2D74A		x	x	x	x	x	x	x	o	x	x	x	x	x	x

An "x" marks the channels that fit a Gaussian distribution. An "o" marks the channels that are very close to a Gaussian distribution. A " " (blank) marks the channels as non-Gaussian. File W1D61A was based on a time window from 35.84 to 122.87 sec. Files W2D61A, W2D68A, and W2D74A were based on time windows from 0.01 to 62.00 sec.

Examples of the stationarity test for channel 3 are shown in Figure 11. The plots show that the channel tests as non-stationary at 1.76 and 2.15 Hz. Note that these frequencies also exhibit higher amplitude levels, indicating that the non-linearity in the plot is probably due to wind noise.

4.2 CHANNEL NOISE

4.2.1 Hardware Noise

Channel hardware noise provides a lower bound estimate of the overall system noise. Channel hardware noise consists of the combined measurement of electronic, seismometer, and digital noise. Hardware noise is isolated by calculating the temporal incoherence between collocated sensors. The noise $G_{nn}(f)$ is calculated in terms of the incoherent spectrum referenced to the input. The noise at sensor n is defined by

$$G_{nn}(f) = [1 - V_{mn}(f)] G_{mm}(f) / |H_m(f)|^2 \quad (20)$$

where $H_m(f)$ is the channel response for sensor m . $V_{mn}(f)$ is the complex temporal coherence between sensors m and n

$$V_{mn}(f) = [G_{mn}(f) G_{nm}(f)] / [G_{mm}(f) G_{nn}(f)] \quad (21)$$

$G_{mn}(f)$ is the 1-sided ensemble average of (cross-) PSD's calculated from a window of period T by

$$G_{mn}(f) = (2/T) \langle X_m(f,T) X_n^*(f,T) \rangle \quad (22)$$

NY-NEX channel hardware noise was measured between vertical sensors 6 and 7 reinstalled with a 0.3 m separation at WO. The experiment recorded 5.12 sec samples every hour for 64 hours. These samples were used to construct the ensemble average of periodograms $G_{mn}(f)$ (128 degrees of freedom) graphed as the lower curves shown in the plots of Figure 13.

4.2.2 Ambient Noise

Ambient ground motion may be defined as the sum of independent random seismic events. Random events may be described as noise generated by vehicles, animals, and all random electronic noise not described by the channel response. Typical noise levels recorded during pre-shot windows are shown in Figure 10. Noise is described both at a

point (seismometer) or by that which is passed by the array. Random noise is classified by its stationarity, normality, and spectra. Microseismic activity is found to exhibit the attributes of a stationary Gaussian random process.

Ambient seismic noise has been analyzed for pre-shot windows. In cases where the seismic noise at a point was determined to be both stationary and Gaussian, it was classified in terms of its PSD [16]. Ensemble averages of periodograms were calculated by taking the sum of FFT's in non-overlapping segments in pre-shot ambient noise windows. The data were padded with zeros (interval doubling) to reduce leakage and variance [17] generated by the FFT transformation (Appendix A). The periodograms quantify the noise at various frequencies in the 0.0 to 50.0 Hz band that may interfere with the signal.

4.2.3 Digital Noise

One important component of digital noise which must be avoided is aliasing. Aliasing results from the digital sampling of data below the Nyquist frequency (twice the highest frequency) in the analog waveform. Sample rates below twice the Nyquist frequency will cause distortion in the recorded signal. The Protection Ratio [18] identifies the effects of the first-fold alias of the data within the Nyquist interval. It is calculated by the ratio of the amplitudes of the in-band frequencies (0.0 to 50.0 Hz) to those of the out-of-band frequencies (50.0 to 100.0 Hz) by

$$H_m(f) = H_m(f) / H_m(2f_n - f) \quad (23)$$

where $H_m(f)$ is the channel response for channel m and f_n is the Nyquist frequency. The high and low gain Protection Ratios of Figure 14 indicate that the data recorded above 30.0 Hz is affected by aliasing. The Rg waves analyzed in this study are in the 1.0 to 5.0 Hz band and are minimally effected by aliasing.

Another component of digital noise results from the digitization of analog signals by the analog-to-digital converter (A/D) and is measured in terms of quantization [19]. Quantization noise has been calculated for GDAS and referenced to the input by

$$G_{mm}(f) = G_{NN}/|H_m(f)|^2 \quad (24)$$

where $G_{mm}(f)$ is the quantization noise for channel m . G_{NN} is the quantization level Q produced by the GDAS 15-bit A/D converter distributed as white noise over the GDAS 50.0 Hz Nyquist interval. G_{NN} , shown in Equation (25), is measured in units of volts^2/Hz .

$$G_{NN} = (Q^2/12)/50.0 \quad (25)$$

4.2.4 Summary

The plots of Figure 13 show the channel hardware noise (lower curve) compared with the ambient seismic noise (upper curve) for channels 1, 3, 7, and 14. The spectra are characteristic of the noise field present throughout the NY-NEX experiment. Analysis of the plots in the 0.0 to 1.0 Hz band indicates a sharp increase in the ambient noise from $1.0 \text{ E-}10$ to $1.0 \text{ E-}6 \text{ (mm/sec)}^2/\text{Hz}$. This increase correlates with the increase in hardware noise and may affect the azimuth and phase velocity estimates. Figure 13 shows that at frequencies greater than 1.0 Hz, the ambient noise tends to level off at about $1.0 \text{ E-}11 \text{ (mm/sec)}^2/\text{Hz}$ with the exception of a few noise peaks within the 10-13, 13-16, 18-19, 22-26 and 29-30 Hz bands. These noise peaks are of unknown origin and are, fortunately, outside of the 0.6 to 3.3 Hz Rg wave band of interest in this study area. The consistency of these spectra with those taken at different ambient seismic noise windows identifies the noise as an ergodic random process. Overall, the spectra show that the signals can be detected accurately in the 1.0 to 10.0 Hz band.

The Protection Ratio plots of Figure 14 indicate, for example, that samples recorded at 40.0 Hz will appear 20 times greater than their aliased 60.0 Hz values. The Protection

Ratio at 1.0 Hz is approximately 1.5×10^{-4} . Overall, the Protection Ratio favors signal detection in the 0.0 to 40.0 Hz band.

A comparison of the quantization noise (Figure 15) to the channel hardware noise (Figure 13) indicates that the effect of digitization noise on seismic recordings is negligible since it is approximately three orders of magnitude less than the hardware noise.

4.3 ARRAY NOISE

Array noise is described as noise passed by the array. Sections 4.3.1 and 4.3.2 describe this additive noise in terms of spatial aliasing and ambient noise.

4.3.1 Spatial Noise of the Array

Spatial aliasing is one component of hardware noise and is controlled by sensor spacing. Spatial aliasing is defined in terms of wavenumber just as sample aliasing is defined in terms of frequency. A Nyquist wavenumber K_n was calculated for a sensor spacing D from the following equations:

$$K = 2\pi/\lambda$$

$$K_n = 2\pi/(D/2)$$

$$K > K_n = \pi/D \quad (26)$$

where λ is wavelength. According to Table 3-2 and Equation (26), aliasing for the WO NY-NEX array would occur at wavenumbers above 0.1571 rad/m for the minimum 20.0 m sensor spacing between channels 7 and 6, and above 0.0070 rad/m for the maximum 448.0 m sensor spacing between channels 7 and 1. Spatial aliasing was not a noise problem in this thesis since the Rg waves studied were within a group velocity range of 1.9 to 3.4 km/sec, producing wavenumbers within a range of 0.0017 to 0.0009 rad/m.

4.3.2 Ambient Noise of the Array

Ambient seismic noise attributes are given in terms of frequency and wavenumber and are essential to the optimum array processing of weak signals. Figure 16 shows the ambient seismic noise passed through the array. The conventional frequency-wavenumber (F-K) algorithm used to produce these results is discussed in Section 5.1.1. The noise for this plot is block averaged over 25 non-overlapping 2.56 sec segments (50 degrees of freedom) in the pre-shot ambient seismic noise window. Peak power (maximum $P(K_x, K_y, f)$) results for the ambient array noise are listed in Table 4-2.

In Figure 16, the plot of $P(K_x, K_y, 1.76)$ for some ambient seismic noise indicates maximum power came from a beam steered towards signals arriving from a 135.0° azimuth with a phase velocity of 4.69 km/sec (as shown by the velocity circle on the plot). As stated in Section 3.3.3, contour levels are measured in db down from the maximum computed level. The plot of $P(K_x, K_y, 1.95)$ indicates a maximum power for a beam steered to signals arriving from a 153.4° azimuth with a velocity of 6.58 km/sec. $P(K_x, K_y, 2.15)$, and $P(K_x, K_y, 2.25)$ indicate a maximum power from beams steered to receive signals from the southeast and northeast at velocities around 7.0 km/sec. Overall, the central main lobes (areas of contour levels less than 3 db) in Figure 16 indicate that coherent noise passed by the array had a variety of azimuths and high phase velocities. These velocity estimates are outside of that expected for the 1.9 to 3.4 km/sec Rg wave arrivals. The additive effects of this ambient noise with the recorded signal will tend to show up as high phase velocity noise with scattered azimuths.

Table 4-2

AMBIENT NOISE ARRAY RESULTS

<u>FREQUENCY</u> <u>(Hz)</u>	<u>PEAK POWER</u> <u>(mm/sec)²/Hz</u>	<u>PHASE VELOCITY</u> <u>(km/sec)</u>	<u>AZIMUTH</u> <u>(deg)</u>
1.76	0.26	4.69	135.00
1.95	0.62	6.58	153.44
2.15	0.15	7.25	206.57
2.25	0.36	7.59	333.43

5 RG WAVE AZIMUTH AND PHASE VELOCITY ESTIMATIONS USING AN ARRAY

5.0 INTRODUCTION

The problem being studied here is that of estimating Rg wave azimuth and phase velocity as a function of frequency for the NY-NEX shots. As mentioned in Chapter 1, the Rg wave bandwidth is limited to 0.6 to 3.3 Hz. In a simply layered half-space, azimuth estimates should show a minimal deviation in azimuth from the great-circle azimuth for frequencies in the 0.6-3.3 Hz range. However, it has been found that azimuth estimates for the NY-NEX study were widely distributed about the great-circle azimuth within this frequency band. This scatter is analyzed to determine if it is caused by lateral heterogeneity in the shallow crustal structure and/or ambient noise.

Classically, propagating plane waves have been characterized in terms of their azimuth and phase velocity by a F-K power spectral density function $P(K_x, K_y, f)$ (see Lacoss [9] and Capon [10]). This frequency-domain synthesis technique has advantages over the corresponding time domain method primarily because of considerable reductions in beam forming computation time [20], and secondarily the time domain assumption that the signal is identical across the array [21] is not necessarily true for dispersive surface waves.

The azimuth and phase velocity for NY-NEX Rg waves were estimated using the conventional F-K algorithm discussed in Section 5.1.1. Several other conventional and high-resolution frequency-domain techniques were initially applied to the Rg waves recorded by the WO NY-NEX array in an effort to improve upon the azimuth and phase velocity estimations. The criterion for deciding which technique to implement was based on finding the method which minimized the amount of scatter in azimuth and phase velocity estimates within the frequency band where the Rg wave is present. The results of the conventional

and high-resolution algorithm applications developed by Capon et al. [10,20,21] and Lacoss et al. [9,22] are summarized in the following sections.

I. Conventional Methods

1. F-K Analysis on Raw Data

Out of the several algorithms tested, F-K analysis provided the smallest deviation in azimuth and phase velocity estimates from the expected values in the 0.6-3.3 Hz Rg wave band.

2. F-K Analysis on Filtered Raw Data

A 0.6-3.3 Hz third order butterworth filter applied to the raw time-domain data before F-K analysis to reduce the deviation in azimuth and phase velocity estimates resulted in no improvements over the results obtained from F-K analysis on raw data. Therefore, the additional amount of computation required was not justified.

3. F-K Analysis on Stacked Data

Stacking multiple shots occurring at the same location (shots 7A, 7B and shots 10B, 10C for example) did not reduce the deviation of azimuth and phase velocity estimates over those from the single shot F-K analysis on the raw data.

4. Wideband Detection on Filtered Data

Wideband detection is a covariance based method that provides azimuth and phase velocity estimates for seismic signals. On raw data, this method provided an average azimuth and phase velocity estimate for the entire seismic band, resulting in deviated estimates biased by noise and other reflected and refracted signals. A filter (see Lacoss et al. [22]) of 0.6-3.3 Hz applied the raw time-domain data reduced the deviation in the Rg wave azimuth and phase velocity estimates from

the expected values. These estimates were used as a comparison to the conventional F-K calculated results.

II. High-resolution Methods

1. High-Resolution (Maximum-Likelihood) F-K Analysis [10]

For data in the 0.6-3.3 Hz Rg wave band, high-resolution F-K techniques resulted in a greater deviation in azimuth and phase velocity estimates compared to the conventional F-K algorithm. This scatter is probably caused by unstable PSD estimates $\hat{P}_{mn}(f)$ [$\hat{P}_{mn}(f)$ is discussed in Section 5.1.1]. This instability results from $\hat{P}_{mn}(f)$ being calculated from only one ensemble over the data window. Capon [10] discusses the importance of the block averaging for calculating a stable, inverse matrix $\hat{P}_{mn}(f)$ for the high-resolution method. He states, in fact, that there should be a number of ensemble averages at least equal to the number of sensors. In analysis of the Rg wave, estimates of $\hat{P}_{mn}(f)$ averaged over L-blocks were found to accumulate noise due to the existence of other unwanted signals in the window, producing false power maxima in the band.

2. High-Resolution Wideband Detection [22]

High-resolution wideband analysis resulted in an increase of azimuth and phase velocity estimate deviations from the values expected as compared to the conventional wideband detection method. The poor results of this high-resolution technique were also attributed to the instability of the inverse operator discussed in Section 5.1.1.

III. Comparisons of Methods

Figure 17 shows four typical examples of the contoured $P(K_x, K_y, f)$ values for the data processed from NY-NEX shot 5. Phase velocity $c(f)$ and azimuth estimates are listed at the top of each plot. These plots show the variations of azimuth and phase velocity estimates found throughout the data processing for different frequencies in the 0.6 to 3.3 Hz Rg wave band. In each plot, azimuth and phase velocity estimates were determined from the K_x and K_y grid locations where the power spectra $P(K_x, K_y, f)$ is at a maximum. A dashed circle centered at the origin and intersecting this maximum indicates the phase velocity. Contour levels are shown in levels of db down from the normalized maximum (see Table 3-5 for description of db levels). The azimuth was determined as the angle between the positive vertical axis (north) and where the phase velocity circle intersects the maximum.

Figures 18A, 18B, and 18C show results for the wideband analysis methods for shot 7A. Figure 18B indicates a heightening of contours due to the application of a 0.6 to 3.3 Hz filter. The high-resolution wideband results shown in Figure 18C produced an unacceptable azimuth of around 250° compared to the expected 301° great-circle azimuth.

Figures 18D, 18E, and 18F demonstrate how stacking the data effects F-K analysis. If noise was a dominant factor, azimuth and phase velocity estimates would be inconsistent between different recordings of data from the same shot. Only minor differences are found between Figures 18D and 18E (shown by the arrows on the graphs), indicating the consistency in azimuth and phase velocity estimates using the F-K algorithm. Furthermore, Figure 18F does not show any improvement over Figures 18D and 18E from a stacking of the data from shots 7A and 7B indicating noise is not a dominant factor.

5.1 DATA PROCESSING

5.1.1 Frequency-Wavenumber Spectra

The conventional F-K algorithm is used in this thesis to estimate power as a function of frequency and wavenumber $P(K_x, K_y, f)$. $P(K_x, K_y, f)$ is used to calculate the azimuth and phase velocity of Rg waves. It is estimated for an NS sensor array by

$$P(K_x, K_y, f) = (1/NS^2) \sum_{m,n=1}^{NS} P_{mn}(\hat{u}) \exp[jK_x(x_m - x_n) + jK_y(y_m - y_n)] \quad (27)$$

where \hat{u} is the normalized frequency $\hat{u} = 2\pi k/N$, and $P_{mn}(\hat{u})$ is a matrix-based estimate of the two-dimensional cross-power spectral density function between sensors m and n . $\hat{P}_{mn}(\hat{u})$ is calculated for L ensemble (L -block) averages by

$$\hat{P}_{mn}(\hat{u}) = 1/L \sum_{l=1}^L S_{ml}(\hat{u}) \bar{S}_{nl}(\hat{u}) \quad (28)$$

where $S_{ml}(\hat{u})$ and $\bar{S}_{nl}(\hat{u})$ are the Fourier transforms of a N -point time series X in the l 'th block. For sensor m , the discrete Fourier transform [19] of $S_{ml}(\hat{u})$ in the l 'th block is calculated by

$$S_{ml}(\hat{u}) = 1/N \sum_{i=0}^{N-1} X_{m,i+(l-1)} \exp(ji\hat{u}) \quad (29)$$

$\hat{P}_{mn}(\hat{u})$ is assumed to be normalized to remove the effects of improper sensor equalization by

$$\hat{P}_{mn}(\hat{u}) = \hat{P}_{mn}(\hat{u}) / [\hat{P}_{mm}(\hat{u}) \hat{P}_{nn}(\hat{u})]^{1/2} \quad (30)$$

Capon [10] defines the high-resolution method for estimating the F-K spectrum as

$$P'(K_x, K_y, f_k) = \left\{ \sum_{m,n=1}^{NS} Q_{mn}(\hat{u}) \exp[jK_x(x_m - x_n) + jK_y(y_m - y_n)] \right\}^{1/2} \quad (31)$$

where $\hat{Q}_{inn}(f)$ is the matrix inverse of the complex spectral matrix $\hat{P}_{mn}(f)$. The step by step procedure used in this thesis to calculate the conventional F-K spectra for the WO NY-NEX seismic data is summarized as follows:

1. Determine the Group-Velocity Window for Analysis

The shot to site distance R divided by the maximum U_{max} (3.4 km/sec) and minimum U_{min} (1.9 km/sec) Rg wave group velocities determined the start time ($t_0 = R/U_{max}$) and stop time ($t_1 = R/U_{min}$) of the group-velocity window.

2. Fourier Transform the Time Window

The FFT of each sensor was calculated for the group-velocity window. Each time series was padded with zeroes (see Appendix A) to improve upon the estimation of $\hat{P}_{mn}(u)$.

3. Calculate the Cross-Power Matrix $P_{mn}(u)$

A NS by NS (14 by 14) normalized cross-power matrix of $\hat{P}_{mn}(u)$ was generated at frequencies f within the Rg wave band for the calculation of $P(K_x, K_y, f)$.

4. Calculate the F-K Spectra $P(K_x, K_y, f)$

$P(K_x, K_y, f)$ was calculated over a 61 by 61 wavenumber grid having a range of ± 0.025 rad/m. The wavenumber range of ± 0.025 rad/m was determined in order to maintain accurate contouring between wavenumber elements as shown in Figure 17. A 61 by 61 grid pattern for this range results in a phase velocity resolution of ± 0.4 m/sec.

5.1.2 Azimuth and Phase Velocity

The conventional F-K algorithm estimates power $P(K_x, K_y, f)$ as a function of frequency and wavenumber, the quantities used to calculate azimuth and phase velocity. $P(K_x, K_y, f)$ was computed for a K_x and K_y grid of wavenumbers between ± 0.025 rad/m

in the 0.6 to 3.3 Hz Rg wave band. The frequency resolution within the band is determined by the number of points N in the group-velocity window (see step 1 in Section 5.1.1) and the sample spacing dt by

$$f = K/(Ndt) \quad (32)$$

At each frequency f within the Rg wave band, the maximum value of P(Kx,Ky,f) was picked from the wavenumber grid. The Kx and Ky location of this maximum was used to calculate the azimuth $\Phi(f)$

$$\Phi(f) = \arctan(Kx/Ky) \quad (33)$$

and phase velocity c(f)

$$c(f) = 2\pi f/|K| \quad (34)$$

where the wavenumber vector K was calculated from its Kx and Ky components by

$$|K| = (Kx^2 + Ky^2)^{1/2} \quad (35)$$

5.1.3 Spatial Coherence

The spatial coherence provides an analysis of coherency of the signals between the sensors of the WO NY-NEX array. The spatial coherence was calculated for frequencies within the Rg wave band by

$$V(Kx,Ky,f) = |P(Kx,Ky,f)| / \sum_{m,n=1}^{NS} |\hat{P}_{mn}(f)| \quad (36)$$

5.1.4 Power Spectral Density Sum

The power spectral density (PSD) sum provides an estimate of the average power at a frequency f for the Rg wave. The PSD sum, PSD(f), was calculated by adding the individual PSD's for each of the NS sensors in the group-velocity window by

$$\text{PSD}(f) = 1/NS \sum_{m=1}^{NS} |\hat{P}_m(f)| \quad (37)$$

PSD(f) represents the ideal F-K power spectral density function. This is shown in Equation (27) when the exponent is zero (where $\hat{P}_{mn}(f)$ is maximum). Thus, this estimate provides information about the amount of power expected at a frequency f for the Rg wave recorded by the WO array.

6 AZIMUTH AND PHASE VELOCITY RESULTS

6.0 INTRODUCTION

The NY-NEX data interpretation described in this chapter was based on the combined analysis of (a) raw data records, (b) raw data records with a 0.6-3.3 Hz 3rd order butterworth filter applied, (c) ambient and hardware noise spectra, (d) the PSD sum curve, and (e) plots of azimuth and phase velocity estimates versus frequency.

The data were compared with their average estimates and standard deviations calculated at 0.5 Hz intervals over a 1.0 to 3.0 Hz band. This procedure made it possible to quantify the amount of scatter in the azimuth and phase velocity estimates at different frequencies in the Rg wave band as measured by the WO array. Theoretically, the phase velocity is not expected to be less than the group velocity at a given period, and therefore, values of phase velocity (and their associated azimuths) are rejected if they are less than the group velocity. Spectral analysis of the NY-NEX shots was limited to a 1.0 to 3.0 Hz band. It was found that for frequencies less than 1.0 Hz the data was dominated by additive noise (see Section 4.2.4) and for frequencies greater than 3.0 Hz coherent Rg waves were not present in the spectra.

NY-NEX shots 5, 6, 7, and 8 were the only shots in the study that produced coherent Rg wave azimuth and phase velocity estimates from the conventional F-K analysis. Shot 10 was processed to determine the effects of stacking noisy records for improved signal-to-noise ratios (SNR). SNR is defined in this thesis as the ratio of the signal amplitude spectra $|S(f)|$ (measured from the spectra of the group-velocity window) to the noise amplitude spectra $|N(f)|$ (measured from the spectra of an ambient noise window immediately preceding the shot) as discussed in Section 4.0.

6.1 SHOT ANALYSIS

6.1.1 Shot 6

Shot 6, 2000 lbs in size, was located at a range of 26.40 km and an azimuth of 32.43° from the center of the WO array. The Rg wave generated by this shot appears approximately 10.8 sec after shot time and can be seen in both the raw and filtered field seismograms (Figures 19A and 19B). The filtered records in Figure 19B clearly show the dispersion of the Rg wave between 9.8 and 11.8 sec after shot time. Figure 19C shows a spectral comparison between the signal and ambient noise ground motions, and the hardware noise. These spectra clearly indicate a Rg wave in the 1.0-3.0 Hz band with amplitudes ranging from 0.9 E-7 to $4.0 \text{ E-7 (mm/sec)}^2/\text{Hz}$ and a high SNR of 100 to 1. The spectra have a high spatial coherence (0.98 to 1.00) in the 1.0-2.2 Hz band as shown in Figure 19D.

The azimuth and phase velocity estimates plotted in Figure 19D are compared to the azimuth and phase velocity averages calculated at 0.5 Hz intervals as listed in Table 6-1. Deviation of the azimuth estimate was minimal (4.01°) in the 1.5-2.0 Hz band. The high deviation (11.34°) in the 1.0-1.5 Hz band is attributed to the high 56.31° azimuth estimate at 1.17 Hz. This scattered azimuth corresponds to a decrease in $\text{PSD}(f)$ from 2.0 E-8 to $1.0 \text{ E-8 (mm/sec)}^2/\text{Hz}$ as shown in Figure 19D. There is an increase in azimuth scatter in the 2.2-2.5 Hz band, indicated by deviations of 17.09° . This scatter may be explained by a weak signal which is shown as the decrease in average power in the $\text{PSD}(f)$ at 2.5 Hz. The phase velocity estimates deviated from their 0.5 Hz averages in the 1.0-2.5 Hz band by 0.45, 0.30, and 0.36 km/sec. These deviations are independent of the scatter in azimuth estimates, spatial coherency, and $\text{PSD}(f)$ levels. Most of the phase velocity estimates in the 2.5-3.0 Hz band were rejected because they were below the 1.9-3.4 km/sec group-velocity window. The consistently low phase velocities in this band are

associated with an increase in signal amplitude (indicated by PSD(f) increasing from 1.0 E-8 to 6.0 E-8 (km/sec)²/Hz) and may be explained by the presence of other coherent waves in the group-velocity analysis window.

An average of the azimuth and phase velocity estimates in the 1.0-3.0 Hz band indicates that a beam was steered to receive Rg waves from a 49.28° azimuth with a 2.47 km/sec phase velocity. This azimuth is 16.85° greater than the expected 32.43° great-circle azimuth. Figure 1A indicates most of the raypath from the shot point to the array as being isolated in the 2.5 km/sec Ammonoosuc Volcanics. The French Pond granite intrusion is also located between shot 6 and the WO array site and it is thought to have a higher velocity of 2.7 km/sec compared to the surrounding formation. This intrusion may have caused some deviation of the Rg wave azimuth from the great-circle path.

Table 6-1

Shot 6 - LINEAR COMPARISONS

f (Hz)	$\Phi(f)$ (deg)	$\overline{\Phi(f)}$ (deg)	σ (deg)	$c(f)$ (km/sec)	$\overline{c(f)}$ (km/sec)	σ (km/sec)
1.07	26.57			3.62		
1.17	56.31			2.45		
1.27	33.69	36.79	11.34	2.65	2.93	0.45
1.37	33.69			2.86		
1.46	33.69			3.06		
1.56	36.87			2.36		
1.66	45.00			2.95		
1.76	45.00	42.11	4.01	2.34	2.49	0.30
1.86	38.66			2.18		
1.95	45.00			2.60		
2.05	45.00			2.73		
2.14	38.66			2.53		
2.25	50.19	52.83	17.09	2.17	2.34	0.36
2.34	77.47			1.92		
2.44	94.76			1.53		
2.54	90.00			1.60		
2.64	68.20			1.85		
2.73	48.81	44.05	3.65	1.94	2.01	0.06
2.83	41.19			2.01		
2.93	41.19			2.08		
3.03	45.00			2.02		

Average azimuth $\overline{\Phi(f)}$ and phase velocity $\overline{c(f)}$ estimates are listed at 0.5 Hz increments between 1.07 and 3.03 Hz. Anomalous values at 2.44-2.64 Hz were omitted in the calculations of the averages due to their low phase velocity. σ is the standard deviation.

6.1.2 Shot 7

Shots 7A and 7B were located 21.33 km from the center of the WO array at an azimuth of 301.20°. The results of the data analysis for shots 7A and 7B were nearly identical and therefore are discussed together. The Rg wave is visible in the raw and filtered time series shown in Figure 20A and 20B at 9.20 sec after shot time, resulting in a group velocity of 2.32 km/sec. Examples of the power spectra (referenced to the input) for channels 1, 3, 7, and 14 are shown in the upper graphs of Figure 20C. The Rg wave spectra appear in these figures in the 1.0-6.5 Hz band with amplitudes ranging from 4.0 E-8 to $3.0 \text{ E-5 (mm/sec)}^2/\text{Hz}$, much higher than that of shot 6. The high SNR in Figure 20C (ratio of the upper curve to middle curve) is approximately 100 to 1. The noise in the plots of Figure 20C appears to be uncorrelated with the signal. Figure 20D compares the array analysis plots. The spatial coherency is high (between 0.97 and 1.00) in the 1.1-2.2 Hz band.

The azimuth plot of Figure 20D is particularly interesting because of the changes in azimuth and phase velocity estimates with frequency in the 2.0-2.5 Hz band. The relatively good azimuth and phase velocity estimate deviations from the average of 5.84° and 0.47 km/sec in this band correspond to a spatial coherency of 0.75 to 0.95. Shots 7A and 7B contain similar power spectra characterized by erratic coherence (8.6 to 9.7) in the 2.25-3.00 Hz band. Estimates in this band were rejected on the basis that their phase velocity is below the 1.9-3.4 km/sec group-velocity window. The stack of shots 7A and 7B demonstrated a slight improvement in azimuth calculations, while the phase velocity estimates resulted in the same amount of scatter (see Figure 18D, 18E, and 18F). This comparison indicates the consistency of the F-K analysis methods and the minimal effects that ambient noise has on these estimates.

An average of the azimuth and phase velocity estimates in the 1.0-2.5 Hz band indicates that a beam was steered to receive the Rg waves from a 276.74° azimuth for a 2.62 km/sec phase velocity. This azimuth is 24.46° less than the expected great-circle azimuth. This change in azimuth could have been caused by a rock velocity gradient decreasing at an angle to the direction of propagation of the Rg wavefront. A simple model to demonstrate this effect is to consider the propagation of Rg waves across a boundary between two different seismic velocities. For a high velocity (V1) to low velocity (V2) boundary, the angle of incidence i_1 is greater than the angle of refraction i_2 (see Figure 21). The 24.46° raypath deflection is consistent with Snell's law in Equation (38) for a high-to-low velocity boundary somewhere along the raypath

$$V_1/V_2 = \sin(i_1)/\sin(i_2) \quad (38)$$

The geologic structure between shot 7 (West Groton,Vt) and the array is best shown by the cross-section in Figure 1B. This cross-sections shows several Ordovician sequences (with velocities ranging from 2.5 to 3.0 km/sec) contacting with the lower velocity (2.5 km/sec) Ammonoosuc Volcanics to the southeast. This contrasting geology could explain the deviation from the great-circle raypath seen in the observed data.

Table 6-2

Shot 7 - LINEAR COMPARISONS

f (Hz)	$\Phi(f)$ (deg)	$\overline{\Phi(f)}$ (deg)	σ (deg)	$c(f)$ (km/sec)	$\overline{c(f)}$ (km/sec)	σ (km/sec)
1.07	90.00			4.05		
1.17	270.00			1.77		
1.27	303.69	292.50	15.83	2.65	2.41	0.34
1.37	296.56			4.61		
1.46	281.31			2.17		
1.56	291.80			2.19		
1.66	284.04			3.04		
1.76	281.31	283.82	5.84	2.60	2.45	0.47
1.86	278.13			1.98		
1.95	270.00			1.84		
2.05	251.56			2.44		
2.14	248.20			3.01		
2.25	258.69	264.77	16.96	3.32	2.84	0.36
2.34	279.46			2.91		
2.44	285.95			2.53		
2.54	270.00			1.60		
2.64	255.96			1.61		
2.73	251.57	rejected		1.63	rejected	
2.83	262.41			1.41		
2.93	265.91			1.57		
3.03	266.42			1.42		

Azimuth $\Phi(f)$ and phase velocity $c(f)$ estimates are listed at increments between 1.07 and 3.03 Hz. Anomalous values at 1.07, 1.17, 1.37, 1.95, and 2.54-3.03 Hz were rejected due to their phase velocities being outside of the group velocity window.

6.1.3 Shot 5

Shot 5, 2000 lbs in size, was located 57.45 km from the center of the WO array at an azimuth of 60.01° . Recognition of a coherent Rg wave is limited to channels 5, 6, 7, and 10 in the raw and filtered time series shown in Figures 22A and 22B, indicating spatial coherency for channels within a 20 m separation. Comparisons of the spectra for channels 1, 2, 4, and 5 in Figure 22C indicate a SNR [ratio of the upper (signal) curve to the middle (ambient noise) curve] of 20 to 1. In the PSD sum curve of Figure 22D, the Rg wave spectra is apparent in the 1.0-2.3 Hz band. The spectra are characterized by a high spatial coherence in the range of 0.92 to 1.00 in the 1.0-2.0 Hz band and a rapid loss of spatial coherence from 0.90 to 0.55 in the 2.0-3.0 Hz band.

The azimuth and phase velocity estimates in the 1.0-3.0 Hz band plotted in Figure 22D have been compared with their average estimates and standard deviations at 0.5 Hz intervals (see Table 6-3) to describe the amount of scatter. The azimuth plot of Figure 22D and the azimuth standard deviations of 28.55° indicate that the scatter is high in the 2.0-2.5 Hz band. Azimuth estimates show a minimal deviation in the 1.0-1.5 Hz band with a deviation of 2.76° . The scatter in phase velocity for the 1.0-3.0 Hz band is below 0.38 km/sec. However, numerous phase velocities were rejected because they were below 1.9 km/sec in the 2.0-3.0 Hz band. The phase velocity plot of Figure 22D and the average estimates at 0.5 Hz in Table 6-3 resemble a dispersive phase velocity curve.

An overall average of the azimuth and phase velocity estimates in the 1.0-3.0 Hz band (avoiding the anomalous values) indicates that a beam was steered to receive Rg waves from an azimuth of 64.63° with a phase velocity of 2.60 km/sec. This azimuth deviation of 4.62° indicates essentially no changes in the lateral variations in the rock velocities along the great-circle azimuth. Geologically, shot 5 parallels the north-northeast trending structure in the region (see Figure 1A).

Table 6-3

Shot 5 - LINEAR COMPARISONS

f (Hz)	$\Phi(f)$ (deg)	$\overline{\Phi(f)}$ (deg)	σ (deg)	$c(f)$ (km/sec)	$\overline{c(f)}$ (km/sec)	σ (km/sec)
1.07	71.57			2.56		
1.17	71.57			2.79		
1.27	71.57	71.77	2.76	3.03	2.59	0.42
1.36	68.20			1.91		
1.46	75.96			2.68		
1.56	90.00			1.47		
1.66	56.31			3.47		
1.76	63.44	62.65	5.98	2.96	3.05	0.38
1.86	108.44			2.21		
1.95	68.20			2.73		
2.05	78.69			1.52		
2.15	33.69			2.25		
2.25	74.06	53.88	28.55	2.33	2.29	0.06
2.34	235.30			1.12		
2.44	143.13			1.84		
2.54	250.91			0.70		
2.64	209.05			1.93		
2.73	56.31	56.31	0.00	1.91	1.91	0.00
2.83	81.25			1.62		
2.93	45.00			1.30		
3.03	225.00			0.54		

Average azimuth $\overline{\Phi(f)}$ and phase velocity $\overline{c(f)}$ estimates are listed at 0.5 Hz increments between 1.07 and 3.03 Hz. Anomalous values at 1.56, 2.05, 2.34-2.54 and 2.83-3.03 Hz were omitted in the calculations of the averages because of their low phase velocity. Anomalous values at 1.86 and 2.64 Hz were omitted in the calculations of the averages because of their low azimuth.

6.1.4 Shot 8

Shot 8 was 2000 lbs in size with an azimuth of 280.15° from the WO array center. Shot 8 had nearly the same azimuth as shot 7 (301.20°) but had a range of 46.19 km instead of 21.33 km. Shot 8 shows evidence of the Rg wave in the filtered time plot of Figure 23B. The Rg wave appears at 18.6 sec from shot time indicating a group velocity of 2.6 km/sec. The PSD plots in Figure 23C (upper curve) show an appearance of the Rg wave in the 1.0-3.0 Hz band with a SNR of 32 to 1. The spatial coherency of these shots is high (0.98 to 1.00) in the 1.0-2.0 Hz band, decreasing to around 0.80 in the 2.0-3.0 Hz band. The average power in Figure 23D in the 1.0-2.0 Hz band is between 0.8 E-8 and $1.0 \text{ E-8 (mm/sec)}^2/\text{Hz}$.

Azimuth estimates in the 1.0-2.0 Hz band show a deviation of 2.71° to 9.20° from the average. The phase velocity estimates in the 1.0-2.0 Hz band deviate from their averages by 0.53 to 0.47 km/sec. This large scatter in phase velocity estimates is clear in the phase velocity plot of Figure 23D. Most of the estimates in the 2.0-3.0 Hz band were unacceptable because of their low phase velocities.

The average azimuth and phase velocity estimates for the 1.0-3.0 Hz band indicate that a beam was steered at an azimuth of 266.62° to receive Rg waves having a phase velocity of 2.60 km/sec. This azimuth is 34.58° less than the expected 280.15° great-circle azimuth. Such a variation in the observed azimuth from the expected great-circle azimuth could have been caused by lateral changes in rock velocities along the raypath similar to that suggested to explain the observations from shot point 7.

Table 6-4

Shot 8 - LINEAR COMPARISONS

<u>f</u> (Hz)	<u>$\Phi(f)$</u> (deg)	<u>$\Phi(f)$</u> (deg)	<u>σ</u> (deg)	<u>c(f)</u> (km/sec)	<u>c(f)</u> (km/sec)	<u>σ</u> (km/sec)
1.07	270.00			2.70		
1.17	270.00			2.95		
1.27	243.43	270.70	2.71	4.28	2.82	0.53
1.37	270.00			3.44		
1.46	281.31			2.17		
1.56	270.00			2.95		
1.66	258.69			2.45		
1.76	255.96	264.66	9.20	3.21	2.60	0.47
1.86	260.54			2.30		
1.95	278.13			2.08		
2.05	270.00			2.21		
2.14	47.29			0.92		
2.25	180.00	270.00	0.00	1.69	2.21	0.00
2.34	235.49			0.91		
2.44	227.29			1.04		
2.54	-----			----		
2.64	236.31			1.38		
2.73	-----	248.20	0.00	----	2.12	0.00
2.83	274.40			1.64		
2.93	350.54			1.21		
3.03	248.20			2.12		

Average azimuth $\overline{\Phi(f)}$ and phase velocity $\overline{c(f)}$ estimates are listed at 0.5 Hz increments between 1.07 and 3.03 Hz. Anomalous values at 2.14-2.64, 2.83, and 2.93 Hz were omitted in the calculations of the averages because of their low phase velocity. The anomalous value at 1.27 Hz was omitted in the calculation of the 1.0-1.5 Hz average because of its low azimuth.

6.1.5 Shot 10

Shot 10 was located at an azimuth of 269.84° and a range of 110.47 km from the WO array site. This shot was near the farthest limit from which Rg waves with acceptable amplitudes for analysis were detected by the array during the NY-NEX experiment. The processing of this shot was to determine if the stacking of two noisy data records from two common shots (10B and 10C) would increase the SNR, causing a decrease in the scatter of azimuth and phase velocity estimates in the 1.0-3.0 Hz band. The Rg wave is not visually present in the raw and filtered field data records shown in the group-velocity windows of Figures 24A and 24B. The plots in Figure 24C also appear to show no presence of the Rg wave in the 1.0-3.0 Hz band. The low SNR in this band is estimated at 2 to 1. Figure 24D shows the F-K results due to the time series stacking. Azimuth estimates in Figure 24D have little indication of a trend.

An average of the azimuth and phase velocity estimates over the 1.0-3.0 Hz band indicates that a beam was steered to receive Rg waves from an azimuth of 239.81° with a phase velocity of 2.88 km/sec. This azimuth is at a decrease of 30.03° from the expected azimuth, indicating a shot-to-site lateral decrease in rock velocity along the great-circle azimuth. The consistency in F-K estimates between the individual shots and their stack indicates that ambient noise did not significantly effect the estimates of azimuth or phase velocity.

6.1.6 Summary

Figures 19 thru 24 represent the time and spatial processing results for the NY-NEX shot data recorded at the WO array. It was found that the stacking of two shots from common shot points did not improve the F-K azimuth and phase velocity estimates, suggesting that the scatter in these estimates was not due to additive noise. Table 6-5 indicates the effect that azimuth measurement error $\Delta\phi_{rms}$ and phase velocity measurement error $\Delta c_{rms}/c$ has on scatter (as discussed in Section 4.0). The high RMS levels in phase velocity measurement error listed for shot 10 may explain the large amount of scatter in the conventional F-K estimates in the 1.0 to 3.0 Hz band. Table 6-5 indicates a minimal deviation in azimuth measurement error for all the shots processed.

Table 6-5		ESTIMATION ERROR			
SHOT	SNR	$\Delta\phi_{rms}$	RANGE OF $\xi/\Delta x$	$\Delta c_{rms}/c$	
5	20	0.04	4.2 - 170.0	0.03	- 1.35
6	100	0.01	4.2 - 170.0	0.01	- 0.27
7	100	0.01	4.2 - 170.0	0.01	- 0.27
8	32	0.02	4.2 - 170.0	0.02	- 0.85
10	2	0.35	4.2 - 170.0	0.33	- 13.53

Rg wavelengths + sensor spacings (3400 m/sec + 20 m)
and 1900 m/sec + 448 m) provides the maximum and
minimum ranges of $\xi/\Delta x$.

For the NY-NEX shot data analyzed, the 1.0 to 2.0 Hz band consistently presented a high spatial coherence (ranging between 0.95 and 1.00). The spatial coherence in the 2.0 to 3.0 Hz band was found to be below 0.90. Dispersive phase velocity trends were noticed in the 0.5 Hz incremental averages for shots 5, 6, 7, and 8 in Tables 6-1 to 6-4.

As a comparison to the average F-K estimates, the conventional algorithm for wideband analysis (see Section 5.0, I-4) with a 0.6 to 3.3 Hz filter was applied in the group-velocity window over the 0.6 to 3.3 Hz frequency band. Azimuth and phase velocity

estimates from the F-K analysis and the wideband analysis techniques are compared in Table 6-6, and the wideband F-K estimates are shown in Figure 25. Wideband azimuth estimates in Table 6-6 are within 10° of the F-K azimuth estimates. The wideband phase velocity estimates in Table 6-6 are unacceptable for shots 5 and 7B because of their low phase velocity. The wideband phase velocity estimates for shots 6 and 7A are lower than the 2.5 to 3.0 km/sec Rg wave velocities expected in the region. Overall the wideband estimates indicate that the phase velocity estimates are poorly determined in the Rg wave analysis.

Table 6-6		AZIMUTHS AND PHASE VELOCITIES				
SHOT	RANGE (km)	TRUE AZ (deg)	F-K AZ (deg)	F-K c(f) (km/sec)	WIDE AZ (deg)	WIDE c(f) (km/sec)
5	57.45	60.01	64.63	2.60	75.96	1.74
6	26.40	32.43	49.28	2.47	51.34	2.15
7A	21.33	301.20	----	----	266.00	2.00
7B	21.33	301.20	----	----	264.29	1.53
7+	21.33	301.20	276.74	2.62	-----	----
8	46.19	280.15	266.62	2.60	260.54	2.60
10	110.47	269.84	239.81	2.88	-----	----

The RANGE and TRUE AZ columns are from Table 1-1. F-K AZ and F-K c(f) are calculated from the overall average of the values (ignoring anomalies) listed in Tables 6-1 to 6-4. WIDE AZ and WIDE c(f) were calculated from wideband analysis. 7+ indicates a stack of shots 7A and 7B.

A map showing true azimuths and F-K azimuths for NY-NEX shots 5, 6, 7, 8, and 10 is shown in Figure 25. The deflection of the Rg raypaths shows a consistent pattern which may reflect velocity variations in the local geology. A model to explain the raypath deviations is one with a gradient in the rock velocity, with the velocity decreasing to the southeast. The Rg wave recorded from shot 5 was less likely to be scattered by geologic features such as faults since its raypath is parallel to the north-northeast trending thrust faults and parallel to the strike of the lateral velocity change. Those raypaths at greater angles

to this northeast direction of shot 5 show increasing raypath deviations from the great-circle path.

A decrease in rock velocity to the southeast between the sites of those NY-NEX shots processed in this thesis and the WO array site can be attributed to a transition from the higher velocity metamorphic formations of Ow, Og, and Oal to the lower velocity Oam formation from northwest to southeast. F-K analysis results for shot 6 found an increase in the Rg raypath azimuth of 16.85° . F-K analysis for shot 5 found a small increase in azimuth of 4.62° . From the northwest, shot 7 was found through F-K analysis to have decreased by 24.46° in azimuth from the true azimuth. The average F-K azimuth estimate for shot 8 was 266.62° , 34.58° less than the great-circle azimuth. An average of the azimuth and phase velocity estimates for shot 10 indicated a decrease in azimuth of 30.03° from the great-circle azimuth. These raypath deflections support a model where shots 5 and 6 are not deflected much by lateral rock velocity variations since their raypaths were parallel to the grain of the structure. Rg waves from shots 7, 8, and 10 had raypaths at different angles to the geologic structure, and in all cases slower velocities towards the southeast would have deflected the raypaths in a counterclockwise direction. This model is illustrated in Figure 25.

6.2 COMPARISON OF GROUP AND PHASE VELOCITY

Kafka (personal communication, 1989) provided several group velocity dispersion curves calculated from the data recorded at sensors 1-7 for shot 22. These calculations were based on an algorithm developed by Dziewonski et al. [23] for the analysis of transient seismic signals. The data were processed at WO using a narrow-band pass filter over a group-velocity window of 2.2 to 3.2 km/sec. The results for each sensor are shown as the lower curves in Figure 27. Figure 27 is a typical example of a Rg wave group

velocity dispersion produced by quarry blasts in the New England region [2]. The difference between group velocity measurements for each sensor is within 0.11 km/sec, indicating the reliability of the estimates. Acceptable phase velocity estimates in Tables 6-1 to 6-4 were averaged at 0.5 Hz increments to provide one general phase velocity dispersion curve $c(av)$ for the Rg waves recorded by the NY-NEX shots. This phase velocity dispersion curve is shown in Figure 26. From $c(av)$, the group velocities listed in Table 6-7 were calculated using Equation (2), Equation (3) and the derivatives of $K=w/c$, resulting in the equation

$$dK/dw = 1/c - w/c^2 dc/dw = 1/U \quad (39)$$

Rewriting Equation (39) as a function of frequency f results in

$$dK/dw = 1/c(f) - f/c(f)^2 [c(f)-c(f-df)]/df = 1/U(f) \quad (40)$$

The group velocity calculations $U'(f)$ agree within 0.3 km/sec of the group velocity dispersion curve in the 1.00 to 2.25 Hz frequency band. $U'(2.75)$ is lower than the expected $U(2.75)$ as listed in Table 6-7 and shown in Figure 27. This low value may be caused by the poor Rg signal generally found for frequencies above 2.00 Hz. The results verify that Rg wave phase velocity dispersion is present and that the expected results agree with other New England Rg wave dispersive group velocity models produced by Kafka [2].

Table 6-7 GROUP VELOCITY MEASUREMENTS

f (Hz)	$c(f)$ (km/sec)	df (Hz)	$c(f-df)$ (km/sec)	$U'(f)$ (km/sec)	$U(f)$ (km/sec)
1.25	2.74	0.25	2.80	2.47	2.59
1.75	2.57	0.50	2.74	2.09	2.41
2.25	2.56	0.50	2.57	2.52	2.36
2.75	2.01	0.50	2.56	0.82	2.30

df is the frequency step between $c(f)$ and $c(f-df)$, $U'(f)$ is the group velocity calculated from values in this table and Equation (40), and $U(f)$ is the group velocity shown in Figure 27.

7 CONCLUSION

A conventional F-K algorithm has been used to estimate azimuths and phase velocities for Rg waves produced from the NY-NEX experiment. Data analysis was based on producing estimates of $P(K_x, K_y, f)$ over a 1.0 to 3.0 Hz band, which was shown by Kafka [2] to contain Rg waves in New England. The noise at the WO NY-NEX array was identified in an effort to determine if the scattered azimuth and phase velocity estimates were the result of (a) scattering due to lateral heterogeneity in geology or (b) measurement error due to the ambient seismic noise.

The scatter in azimuth and phase velocity estimates appears to be primarily due to a lateral variation in the shallow crust and not noise. This lateral variation appears to be related to variations in the seismic velocity structure of the rocks underlying the various geologic formations outcropping in the study area. These conclusions are based on (a) the RMS error in phase velocity measurements between two sensors was found to be negligible for the near shots (5, 6, 7, and 8), but significant for the far shot (10), (b) SNR improvements resulting from the stacking of common data from two shots at the same shot point was shown to not reduce the scatter in the azimuth and phase velocity estimates at different frequencies, (c) ambient noise was identified through conventional F-K analysis to be multidirectional with phase velocities in the 4.7 to 7.6 km/sec range, having no additive effects on the Rg wave, and (d) Rg raypath azimuth estimates agree with a model having a laterally decreasing rock velocities to the southeast.

Azimuth and phase velocity estimates in the Rg wave 1.0 to 3.0 Hz band were found to be affected by the regional geology. Shot 5, with a raypath parallel to the north-northeast trending structure, was found to be deflected by only 5° over the great-circle azimuth. The deflections found in shots 6, 7, and 8 are characteristic of lateral velocity variations along the great-circle azimuths. F-K analysis resulted in average phase velocity

estimates around 2.6 km/sec, within the 2.5 to 3.0 km/sec group velocity range expected for the metamorphic to igneous rocks of the region.

ACKNOWLEDGEMENTS

Some of the research presented in this paper was supported under Air Force Geophysics Laboratory contract F19628-86-C-0055. Other research was completed under the M.S. Thesis requirement in Geophysics at Boston College with the advisory committee of Dr. John E. Ebel, Francis A. Crowley, and Dr. James W. Shehan, S.J. Special attention was directed from Dr. Alan L. Kafka with his Rg wave expertise and the provision of Figures 26 and 27.

APPENDIX A: THE POWER SPECTRAL DENSITY FUNCTION

The Power Spectral Density ($G(f)$ or PSD) is a 2-sided even function with one half the total power (variance per cycle per second) in the positive frequency range. In this paper, the PSD considered over positive frequency is the one-sided PSD function $2S(f)$. Thus, the PSD is expressed in terms of a density $2S(f)$ for positive frequencies.

To expand on this matter theoretically, $S(f)$ is defined in terms of the autocorrelation function $R(\tau)$

$$S(f) = \int_{-\infty}^{\infty} R(\tau) \exp(-j\omega\tau) d\tau \quad (A-1)$$

and relating to the time series $x(t)$

$$S(f) = \lim_{T \rightarrow \infty} 1/(2T) \left| \int_{-T}^T x(t) \exp(-j\omega t) dt \right|^2 \quad (A-2)$$

$S(f)df$ describes the contribution to the variance (amount of power) within the band f and $f+df$. If $x(t)$ is real, as in the case of the time history records, $S(f)$ may be represented by a 2-sided even function

$$S(f) = \lim_{T \rightarrow \infty} (1/2T) \left| \int_{-T}^T x(t) \cos(\omega t) dt \right|^2 \quad (A-3)$$

The one-sided PSD is shown as

$$G(f) = \lim_{T \rightarrow \infty} (1/T) \left| \int_0^T x(t) \cos(\omega t) dt \right|^2 \quad (A-4)$$

or

$$G(f) = \begin{cases} 2 S(f) & f \geq 0 \\ 0 & f < 0 \end{cases} \quad (A-5)$$

The PSD is defined over the interval $[-T, +T]$, and the Fourier transform of $x(t)$ is defined over the interval $[0, +T]$. To obtain the true PSD representation of the autocorrelation, the interval of $x(t)$ is doubled. To accomplish this task, $x(t)$ is increased

APPENDIX A: THE POWER SPECTRAL DENSITY FUNCTION

from $[0, +T]$ to $[0, 2T]$ with the installation of T zero pads. Finally, Equation (A-4) is written in terms of the autocorrelation

$$G(f) = 2 \int_0^{\infty} R(\tau) \cos(w\tau) d\tau \quad (A-6)$$

Relating the above one-sided power spectra to the two-sided power spectra, the total power in the positive frequency range contains the power in the negative frequency range plus the power in the positive frequency range.

APPENDIX B: SYMBOLS

<u>Variable</u>	<u>Description</u>
μ	Mean (Estimated Mean of the Sample)
\hat{u}	Normalized Frequency $\hat{u} = 2n\pi/(N-1)$
σ	Standard Deviation
σ^2	Variance
$\Phi(f)$	Azimuth as a Function of Frequency
π	Pi ($\pi = 3.14159\ 26536$)
$\langle \rangle$	Expected
$1/(Ndt)$	Fundamental Frequency
a	Acceleration
$A(z)$	Amplitude as a Function of Depth
$B(K_x, K_y, t)$	Spatial Window Function or Beamforming Array Response
$c(f)$	Phase Velocity
D	Sensor Spacing
df	Frequency Spacing between Samples
dt	Time Spacing between Samples
$d\tau$	Variable Spacing
dw	Wavenumber Spacing between Samples
E	Base 10 Exponent ($E-2$ is equivalent to 10^2)
E	Frequency Band
\exp	Exponential Function ($\exp = 2.71828\ 18285$)
f	Frequency, Discrete $f = K/(Ndt)$
f_n	Nyquist Frequency
F	Force

APPENDIX B: SYMBOLS

g	Gravity
$G_{mn}(f)$	1-Sided (Cross-) Power Spectral Density
$G_{nn}(f)$	Incoherent Noise
$G_{NN}(f)$	Hardware Noise
$H(f)$	Channel Response [(OUTPUT)/(INPUT) = (volts)/(mm/sec)]
i	Current
j	$\sqrt{-1}$
K	Wavenumber (rad/m)
km	Kilometers
K_n	Nyquist Wavenumber (π/D)
L	Number of Time Segment Blocks (Windows)
m	Meters, or Sensor Channel Number
M	Mass
n	Sensor Channel Number
N	Number of Samples in Time Window
$N(f)$	Noise Spectra
NS	Number of Sensors
$P(f)$	1-Sided Power Spectral Density (PSD), $G(f)$
$P(K_x, K_y, f)$	Frequency-wavenumber Power Spectral Density
$p(x)$	Probability Density Function
$P(x)$	Probability Distribution Function, $\text{Prob}(x \leq x')$
$\hat{P}_{mn}(u)$	Spectral Matrix Calculated from the Discrete Fourier Transform of the Cross-correlation Function
PSD	Power Spectral Density, $P(f)$

APPENDIX B: SYMBOLS

Q	Quality Factor
$\hat{Q}_{mn}(\dot{u})$	Inverse of the Spectral Matrix $\hat{P}_{mn}(\dot{u})$
$R(\tau)$	Autocorrelation Function
$S(f)$	2-Sided Power Spectral Density
T	Period ($T = 1/f$)
U	Group Velocity
$u(x,h,z,t)$	Particle Displacement in Cartesian Coordinates
$V(K_x,K_y,f)$	Spatial Coherence Function
$V_{mn}(f)$	Temporal Coherence Function
V_p	P-Wave Velocity
V_r	Rayleigh Wave Velocity
V_s	S-Wave Velocity
ω	Angular Frequency (rad/sec)
$w(x,y), W_{mn}$	Array Weighting Function
x	Random Variable or Cartesian Coordinate
x_m	x-coordinate Position of Sensor m
x_n	x-coordinate Position of Sensor n
x'	Random Variate
$x(t)$	Time Series
y	Cartesian Coordinate
y_m	y-coordinate Position of Sensor m
y_n	y-coordinate Position of Sensor n
z	Cartesian Coordinate

APPENDIX C. REFERENCES

- [1] Aki, K., Richards, P.G., 1980, Quantitative Seismology, Theory and Methods Volume 2, W.H. Freeman and Co., p.260, 580-633.
- [2] Kafka, A.L., 1990, Rg as a Depth Discriminant for Earthquakes and Explosions: A Case Study in New England, Bull. Seis. Soc. Am., in press.
- [3] Van Diver, B.B., 1987, Roadside Geology of Vermont and New Hampshire, Mountain Press Publishing Co., Missoula, p.18.
- [4] White, W.S., Billings, M.P., 1951, Geology of the Woodsville Quadrangle, Vermont-New Hampshire, Bull. GSA, 647-696.
- [5] Sheriff, R.E., Geldart, L.P., 1986, Exploration Seismology Volume 1, Cambridge Univ. Press, p.48, 49.
- [6] Clark, S.P., 1966, Handbook of Physical Constants, Geol. Soc. of Am., Mem. 97, p.180, 199-204.
- [7] Von Glahn, P.G., 1980, The Air Force Geophysics Standalone Data Acquisition System: "A Functional Description," AFGL-TR-80-0317, ADA100253.
- [8] Lacoss, R.T., Kelly, E.T., Toksoz, M.N., Estimation of Seismic Noise Structure using Arrays, Geophysics, v.34, n.1, 21-38.
- [9] Capon, J., 1969, High-Resolution Frequency-Wavenumber Spectrum Analysis, Inst. Electr. Electron. Eng., v.57, n.8, 1408-1419.
- [10] Mykkeltveit, S., Astebol, K., Doornbos, D.J., Husebye, E.S., 1983, Seismic Array Configuration Optimization, Bull. Seis. Soc. Am., v.73, n.1, 173-186.

APPENDIX C: REFERENCES

- [11] Ingate,S.F., Husebye,E.S., Christoffersson,A., 1985, Regional Arrays and Optimum Data Processing Schemes, Bull. Seis. Soc. Am., v.75, n.4, p.1155-1177.
- [12] Sax,R.L., 1968, Stationarity of Seismic Noise, Geophysics, v.33, p.668-674.
- [13] Bendat,J.S., Piersol,A.G., 1986, Random Data, John Wiley & Sons, Inc., p.74-94.
- [14] Gumbel,E.J., 1958, Statistics of Extremes, Columbia Univ. Press.
- [15] Strotovitch,R.L., 1963, Topics in the Theory of Random Noise Volume 1, Gordon & Breach Science Publishers, Inc.
- [16] Yen,C.K., 1979, On the Smoothed Periodogram Method for Spectrum Estimation, North Holland Publ. Co., p.83-86.
- [17] Blackman,R.B., Tukey,J.W., 1958, The Measurement of Power Spectra from the Point of View of Communications Engineering, Dover Publ. Inc., p.132-135.
- [18] Oppenheim,A.V., 1975, Digital Signal Processing, Prentice-Hall, Inc., p.88,413-417.
- [19] Capon,J., Greenfield,R.J., Kolker,R.J., 1967, Multidimensional Maximum-Likelihood Processing of a Large Aperture Seismic Array, Inst. Electr. Electron. Eng., v.55, n.2, p.192-211.
- [20] Capon,J., Greenfield,R.J., Kolker,R.J., Lacoss,R.T., 1968, Short-Period Signal Processing Results for the Large Aperture Seismic Array, Geophysics, v.33, n.3, p.452-472
- [21] Nawab,S.H., Dowla,F.U., Lacoss,R.T., 1985, Direction Determination of Wideband Signals, Inst. Electr. Electron. Eng., v.33, n.4, p.1114-1122.
- [22] Dziewonski,A., Bloch,S., Landisman,M., 1969, A Technique for the Analysis of Transient Seismic Signals, Bull. Seis. Soc. Am., v.59, n.1, p.427-444.

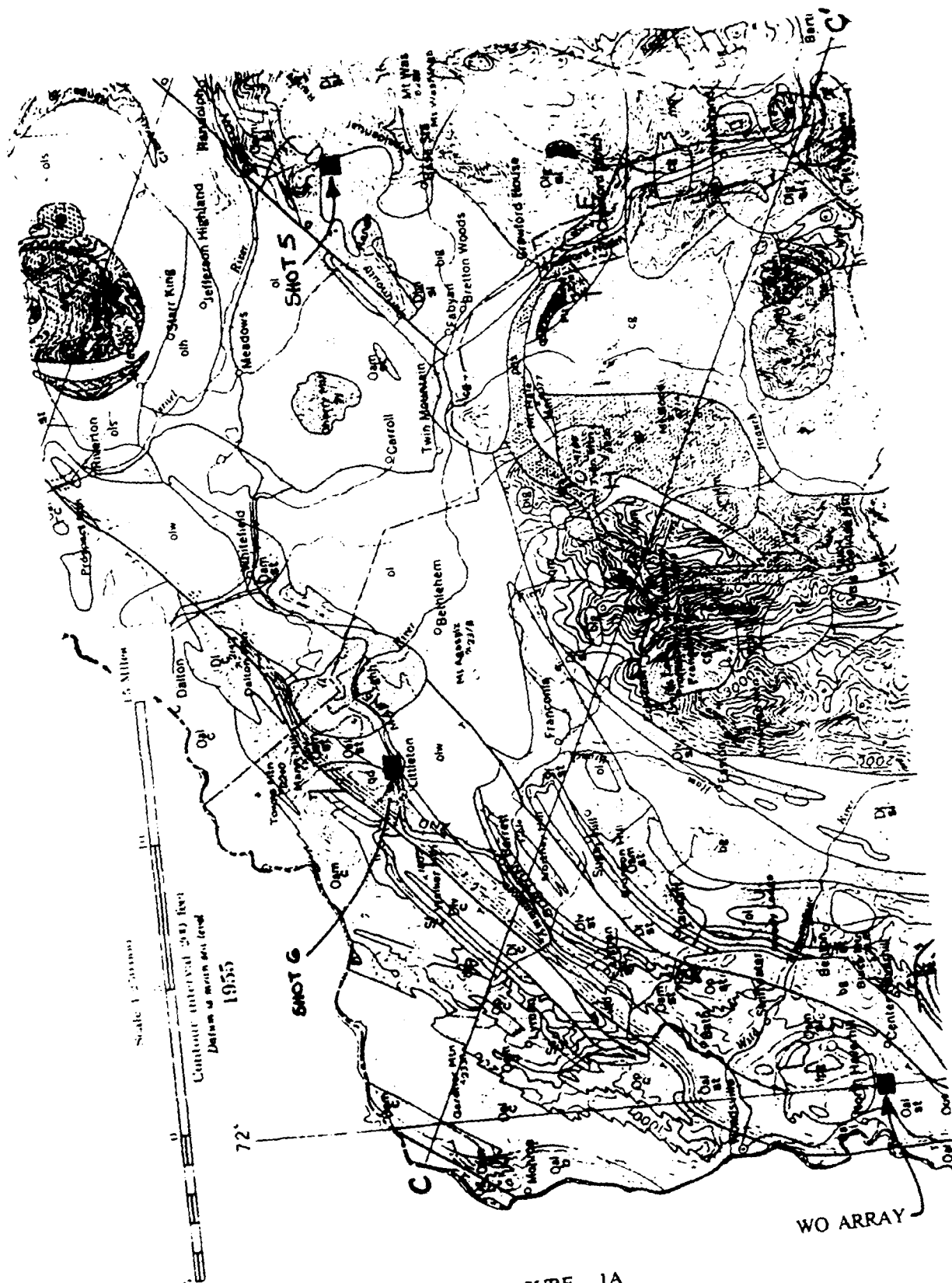


FIGURE 1A

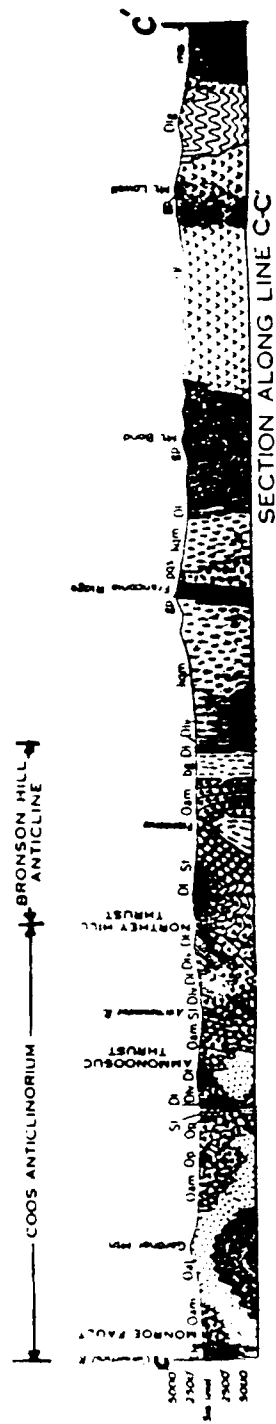


FIGURE 1B



FIGURE 2

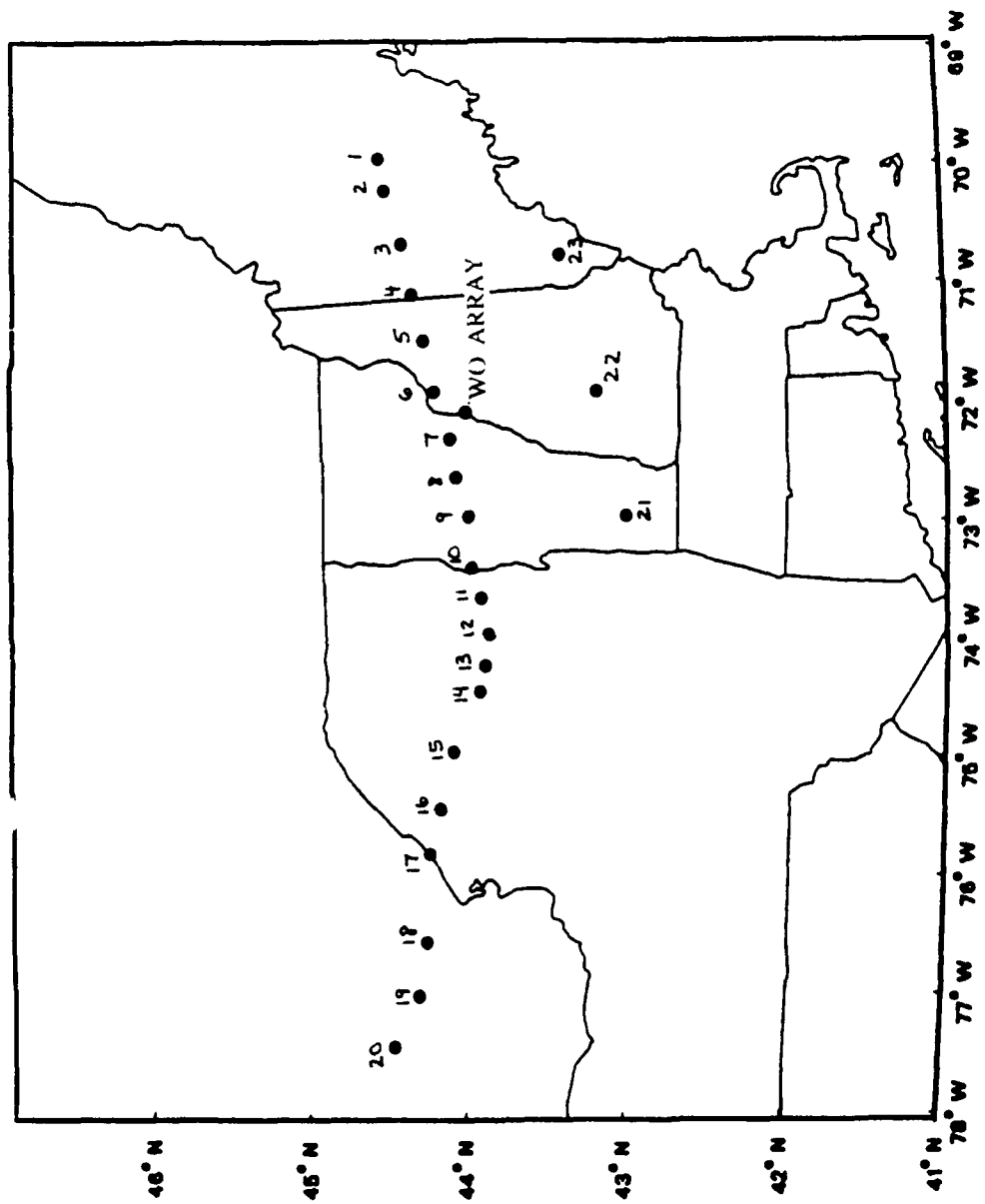


FIGURE 3

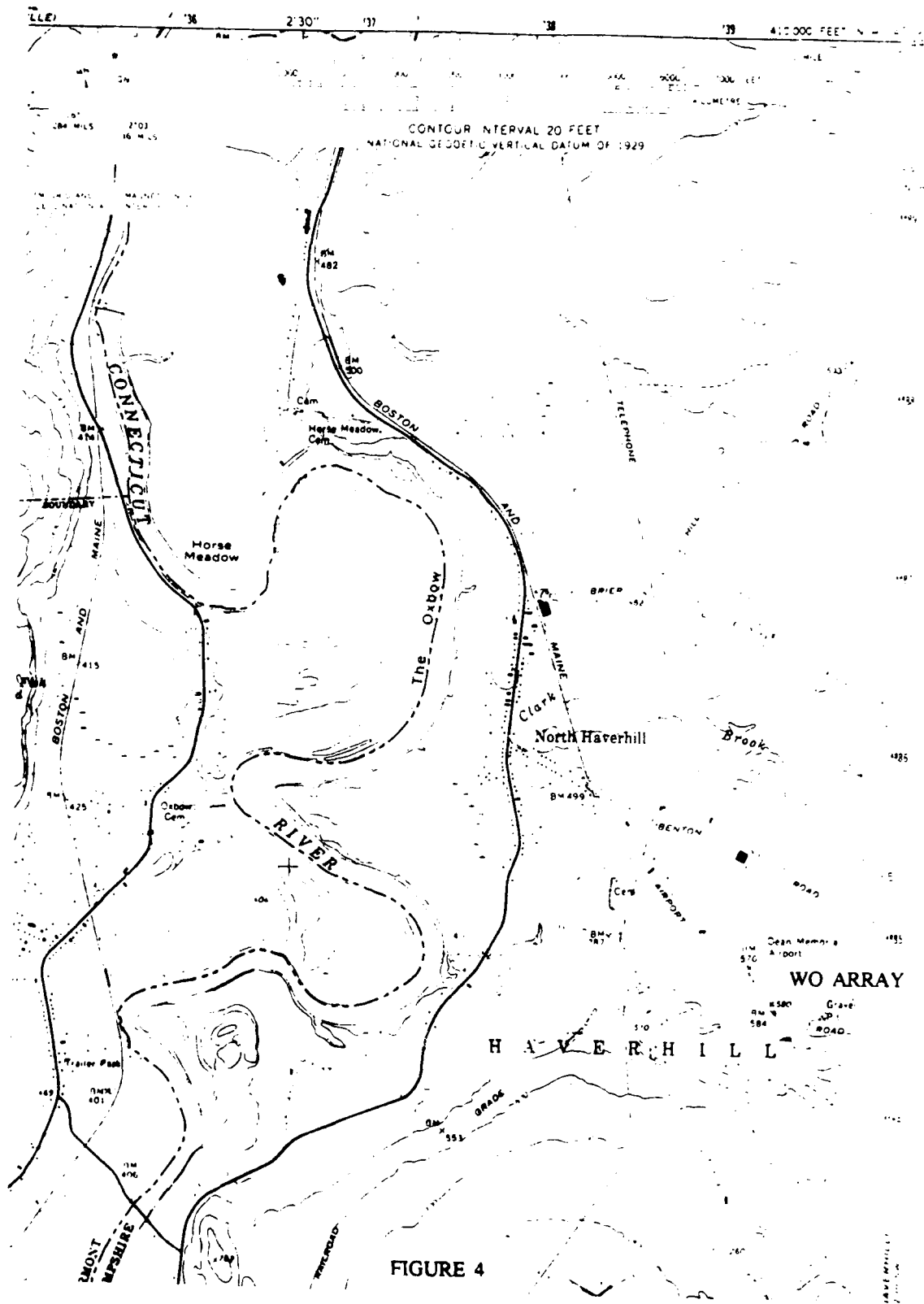


FIGURE 4

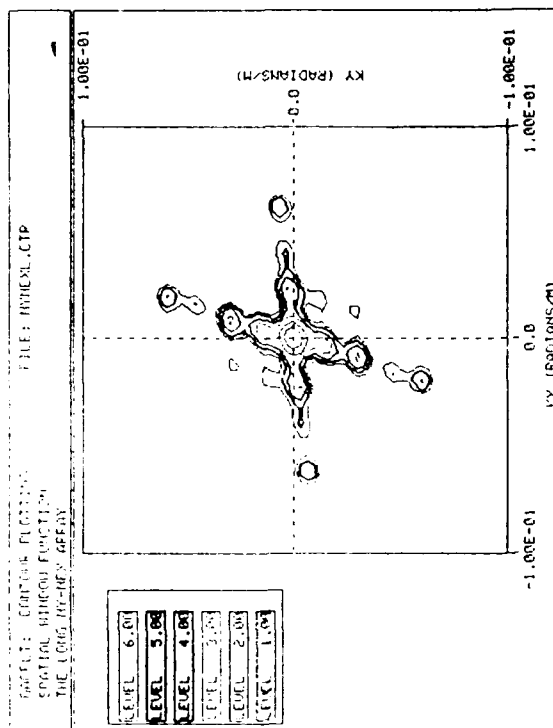


FIGURE 6A

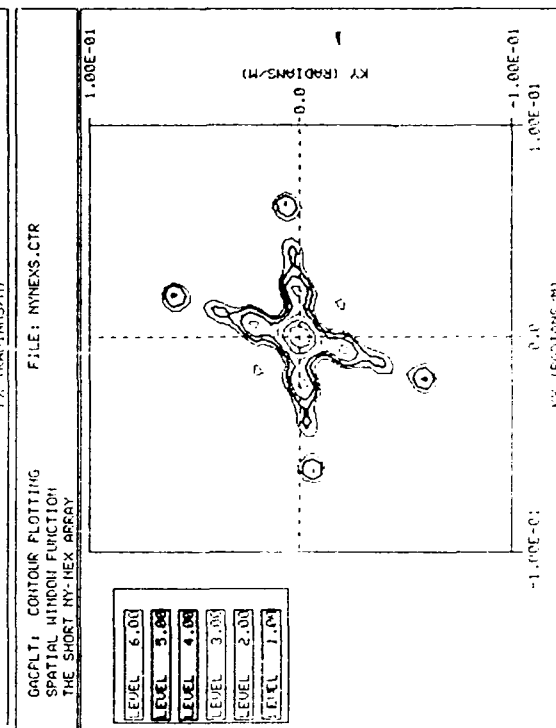


FIGURE 6B

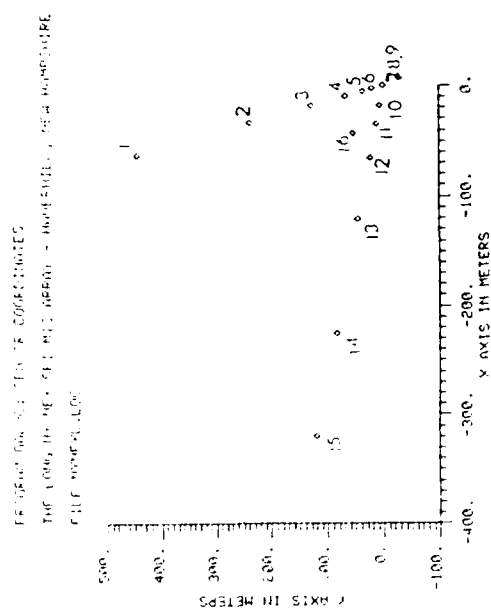


FIGURE 5A

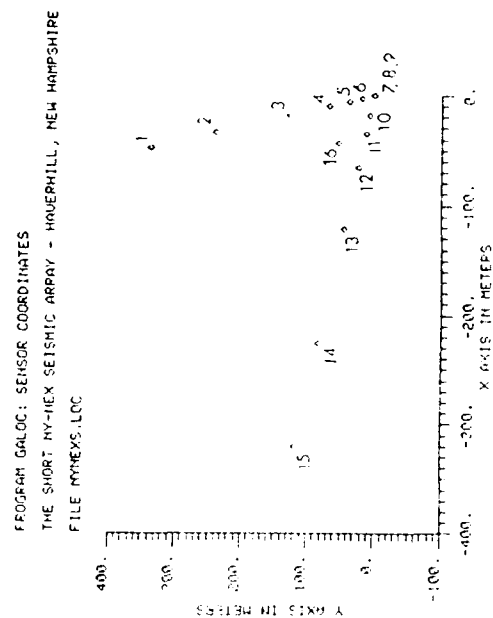
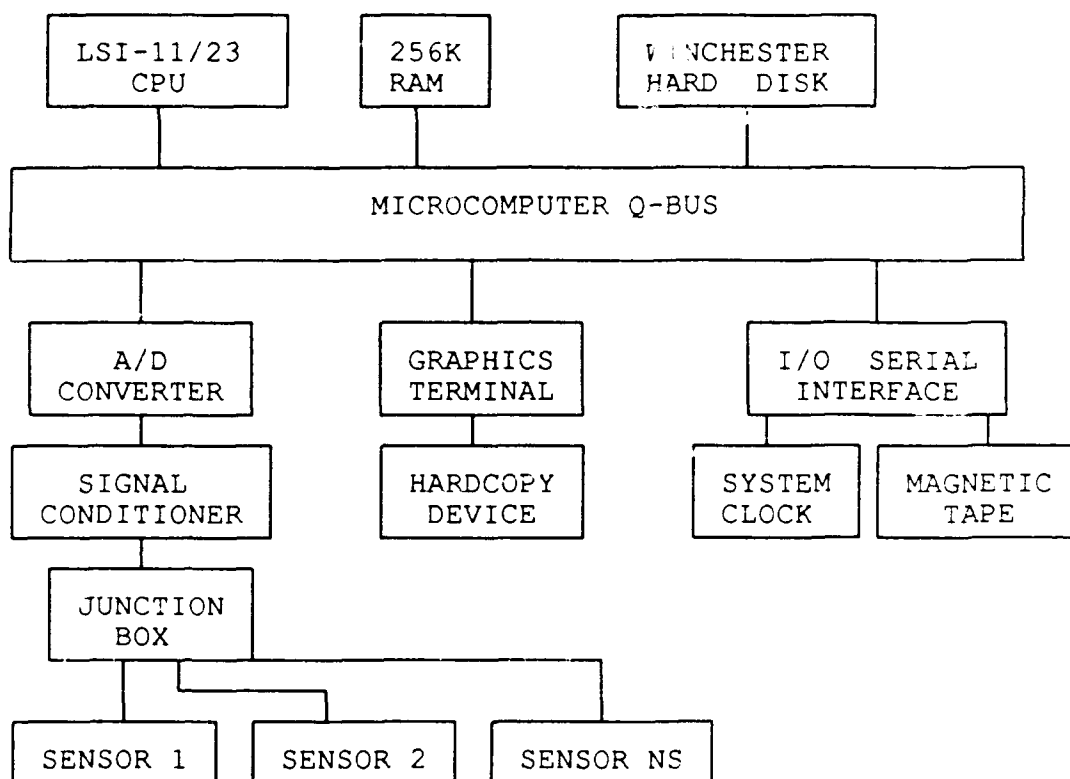


FIGURE 5B



The diagram shows the Geophysical Data Acquisition System (GDAS) hardware flow chart. The "signal conditioner" module contains the preamplifier and filter electronics.

Figure 7

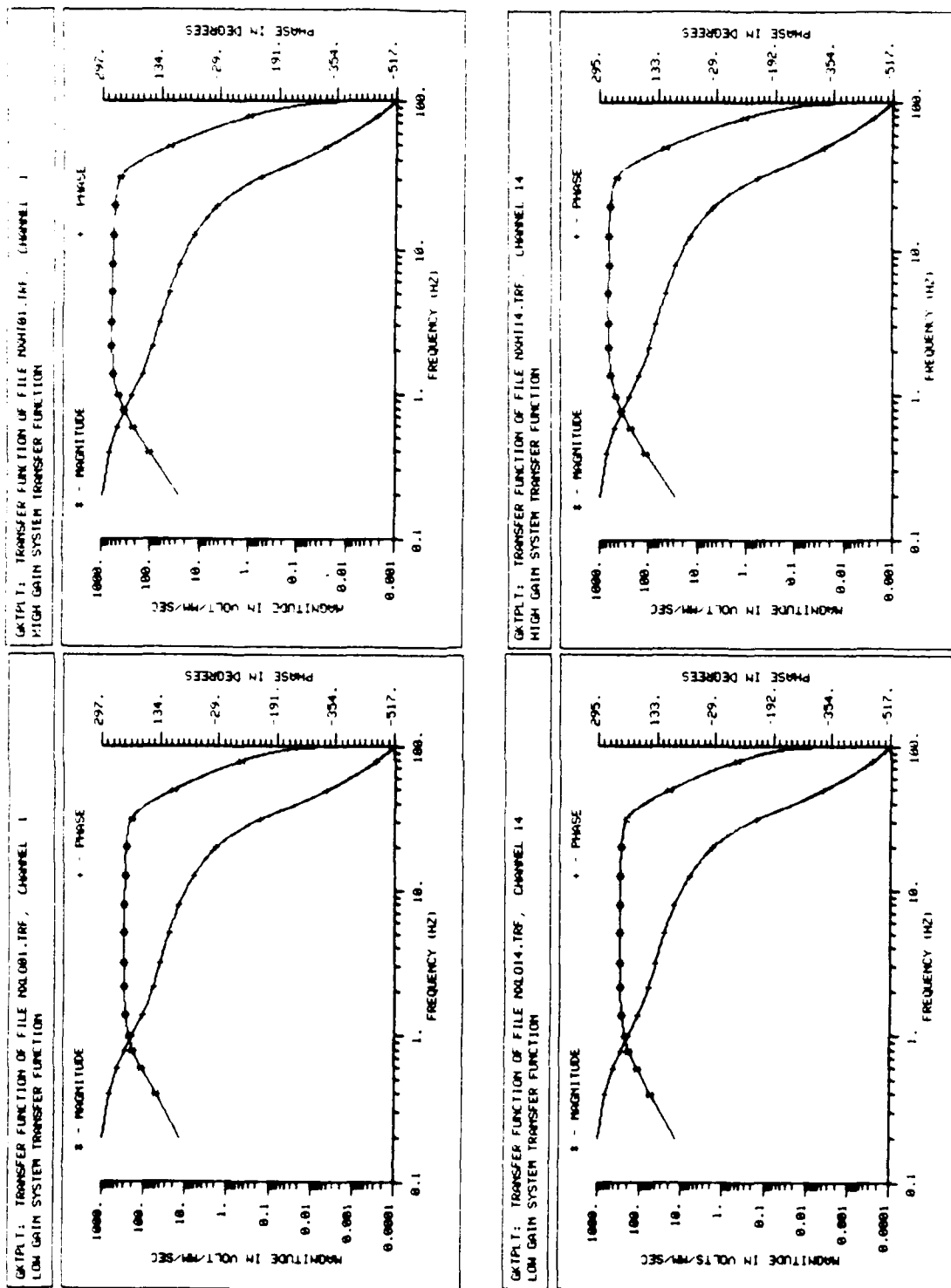


FIGURE 8

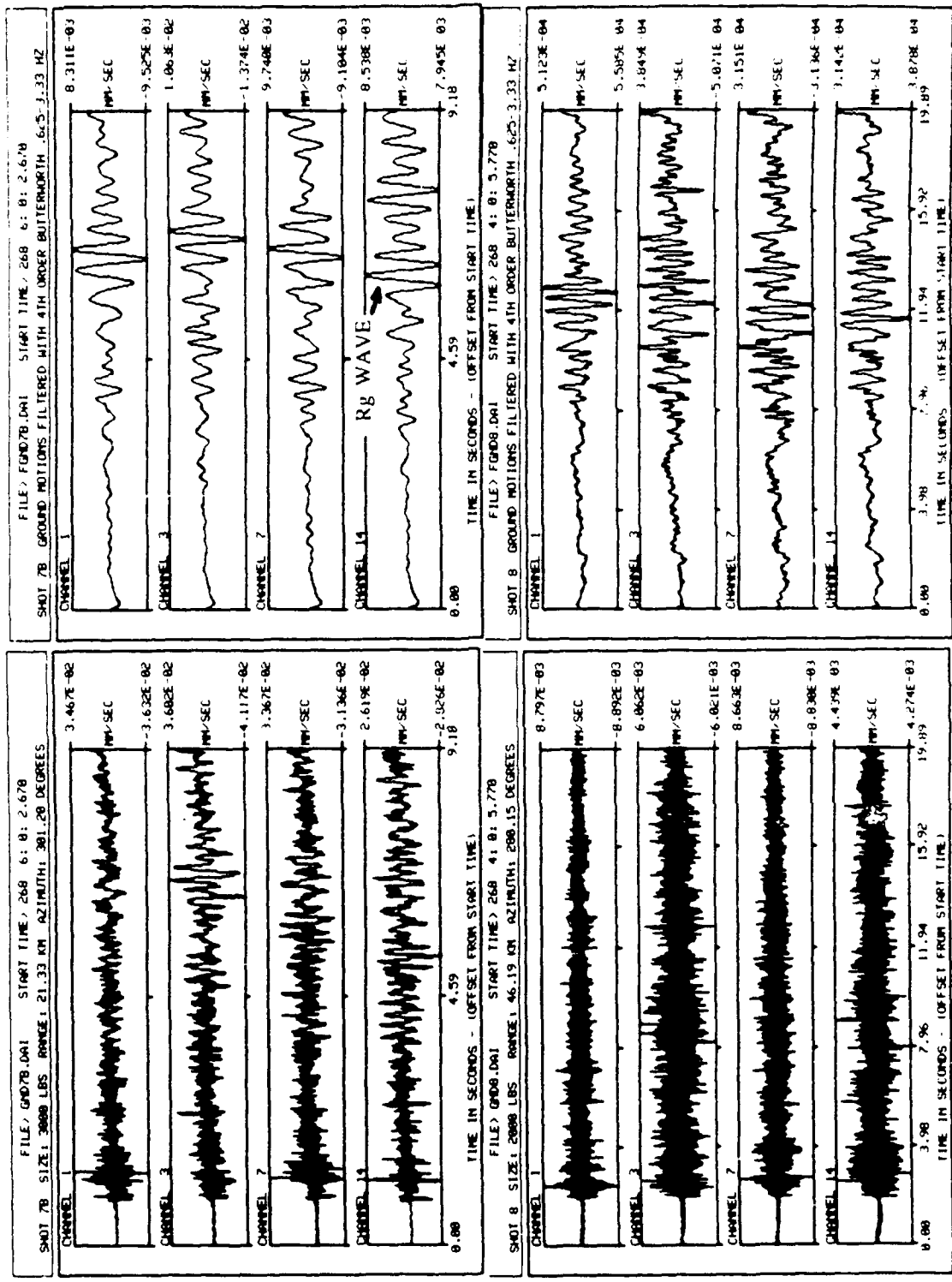


FIGURE 9

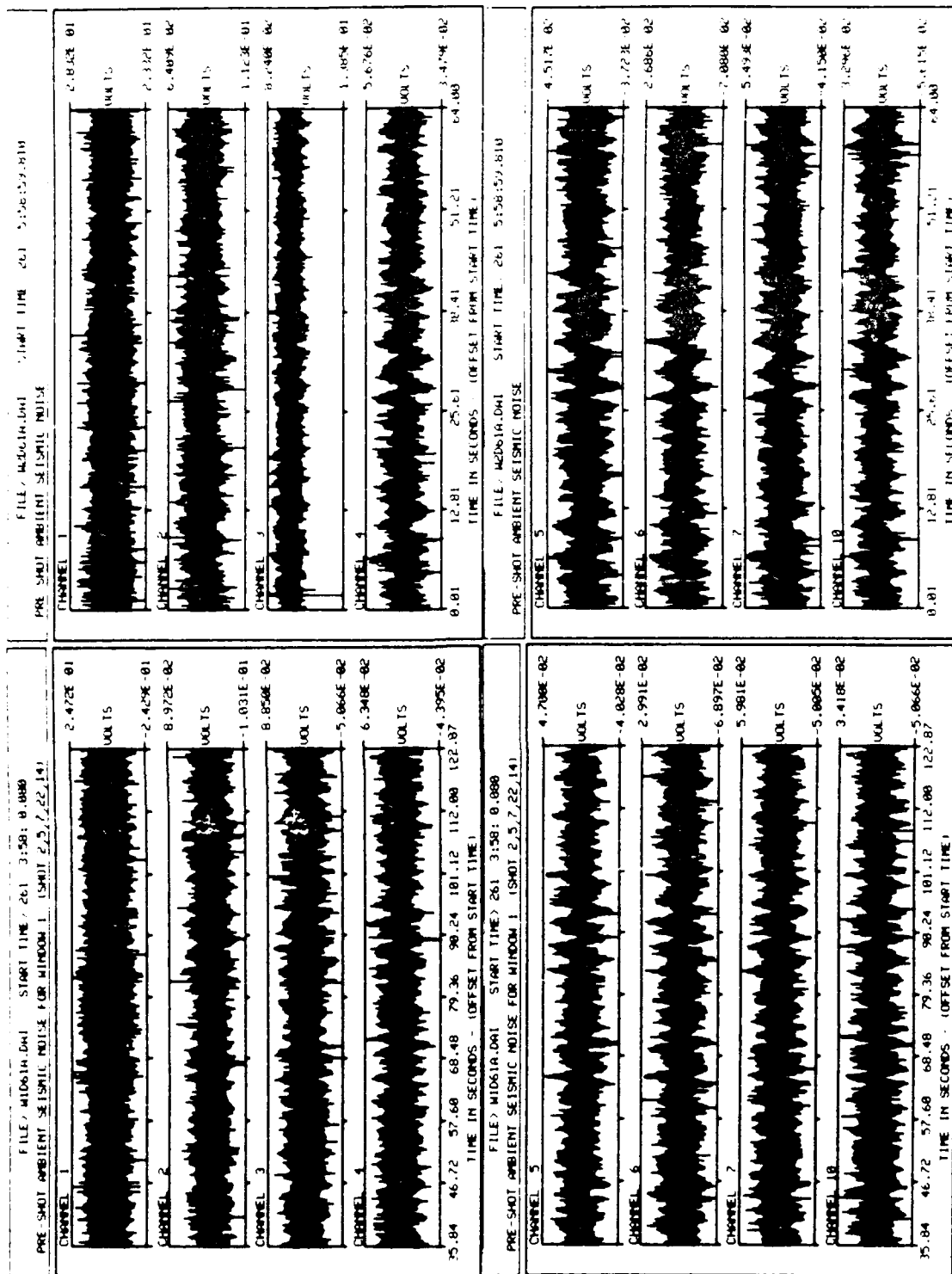


FIGURE 10

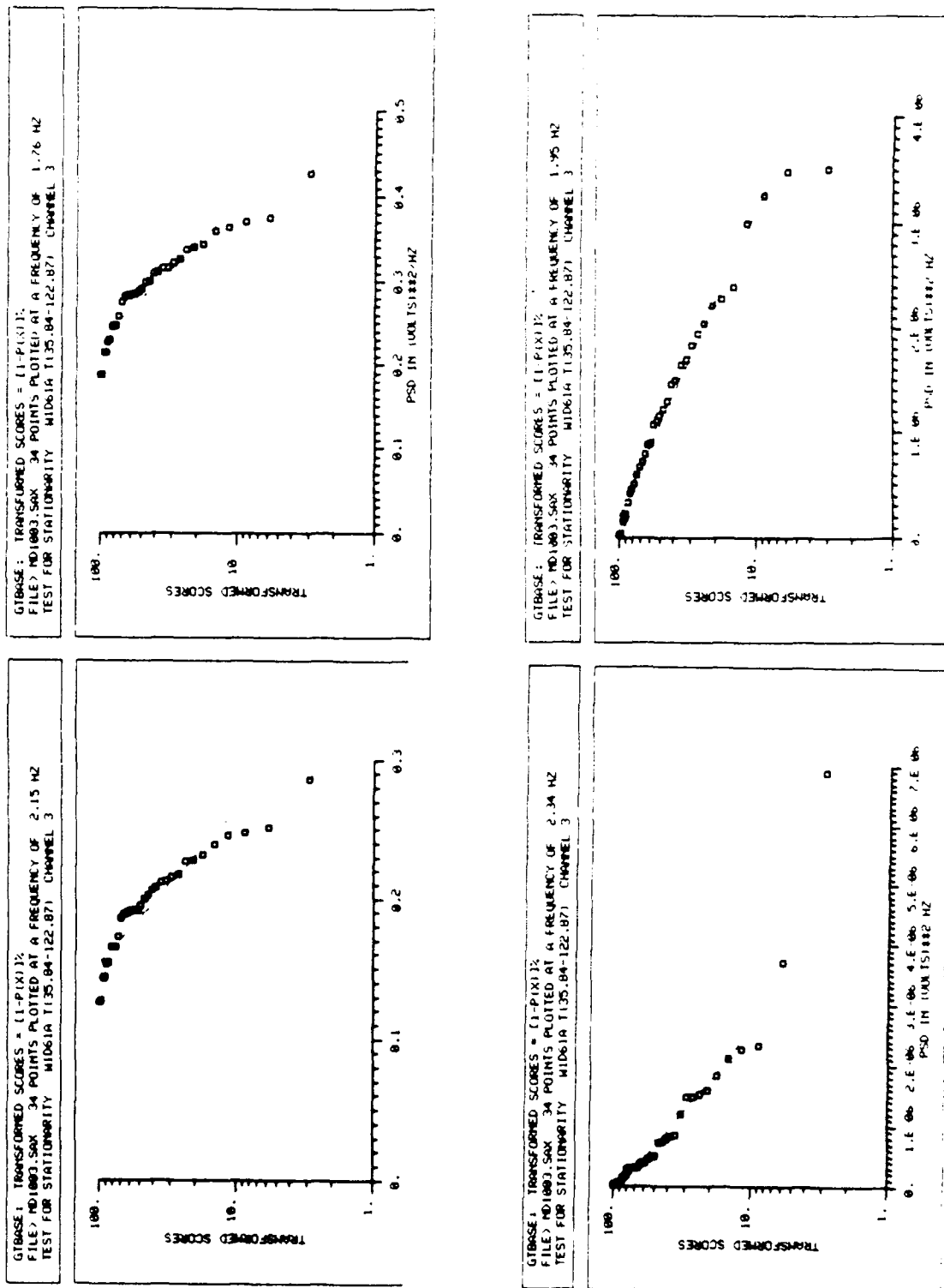


FIGURE 11

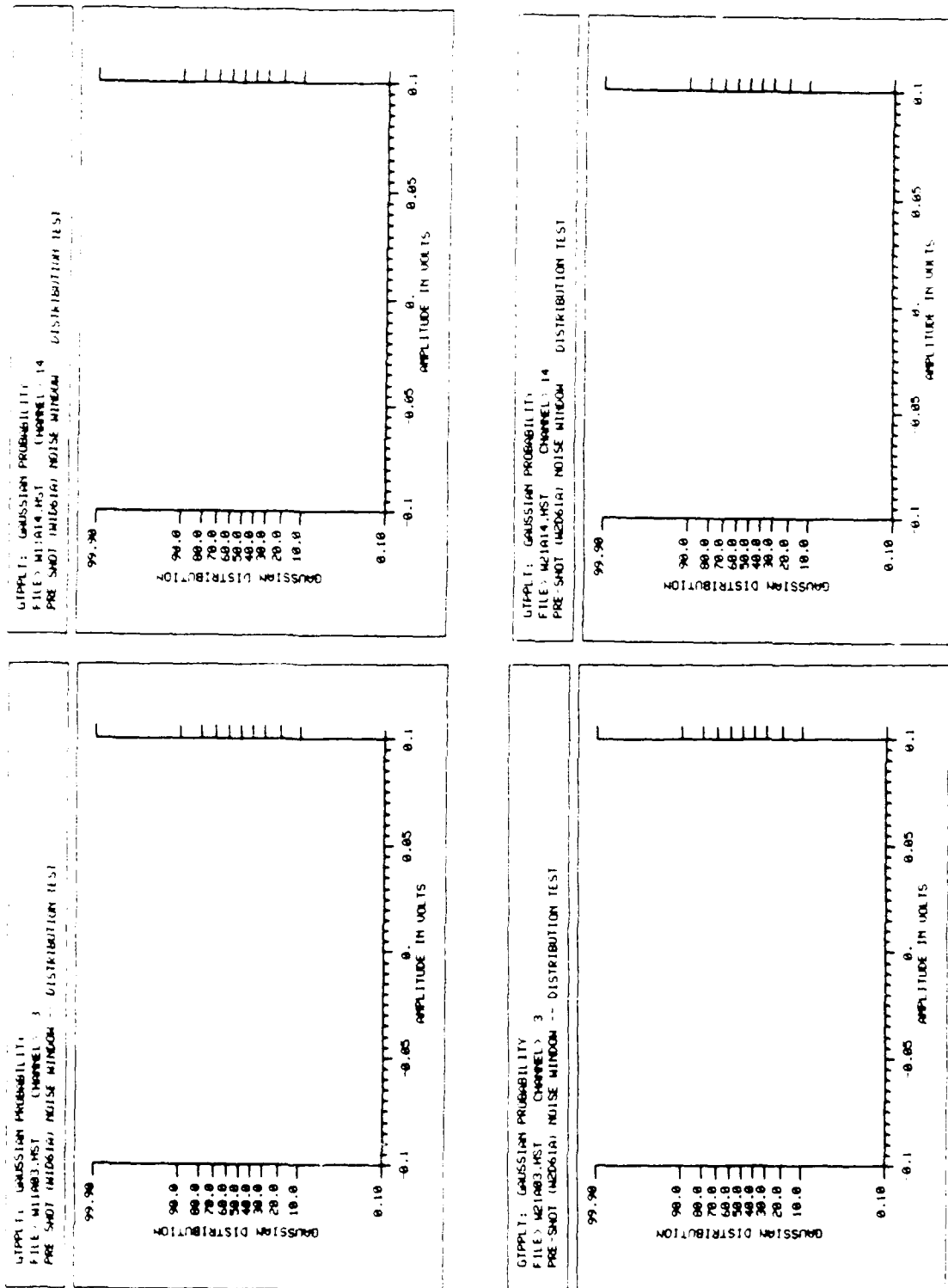


FIGURE 12

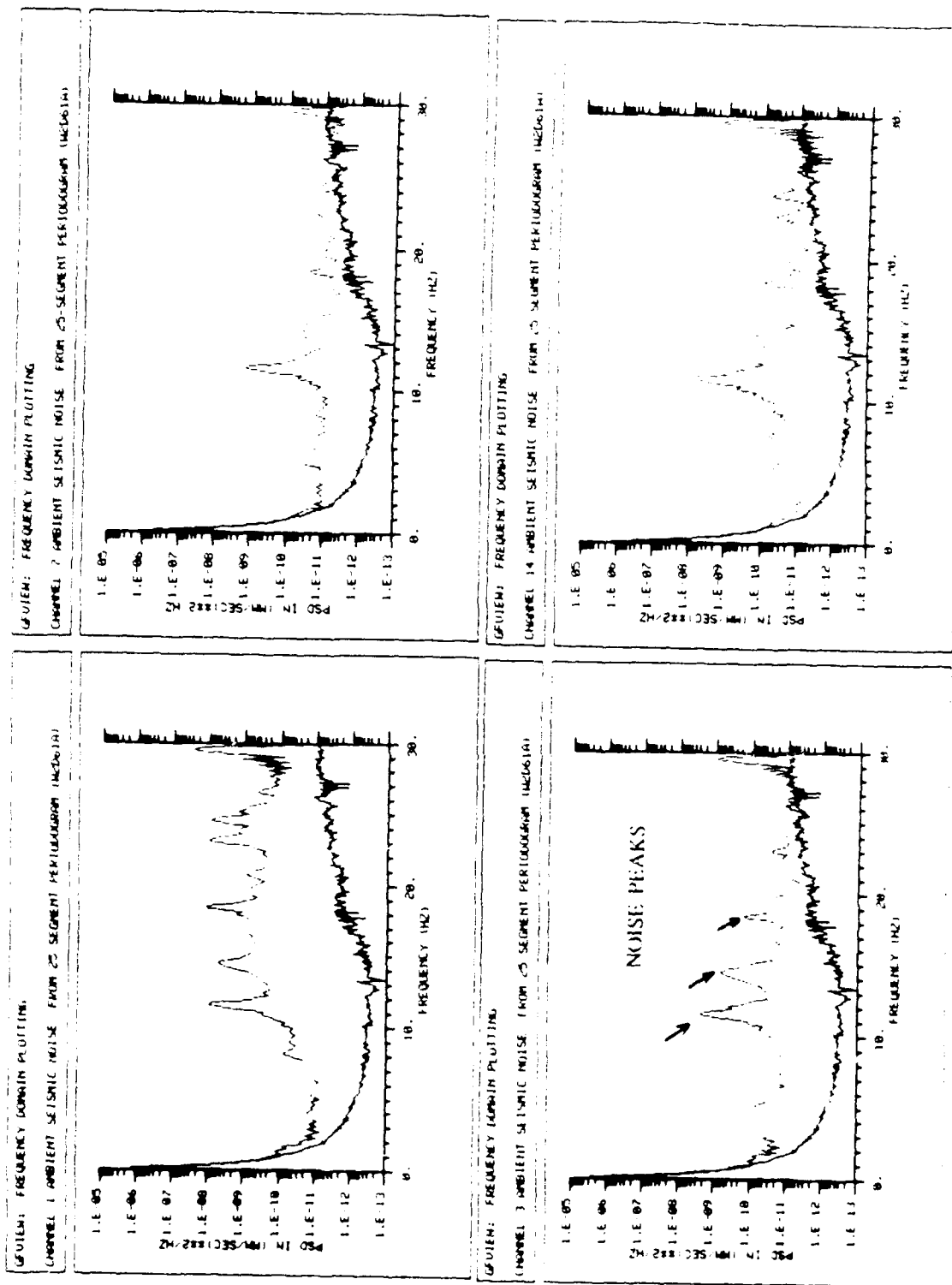


FIGURE 13

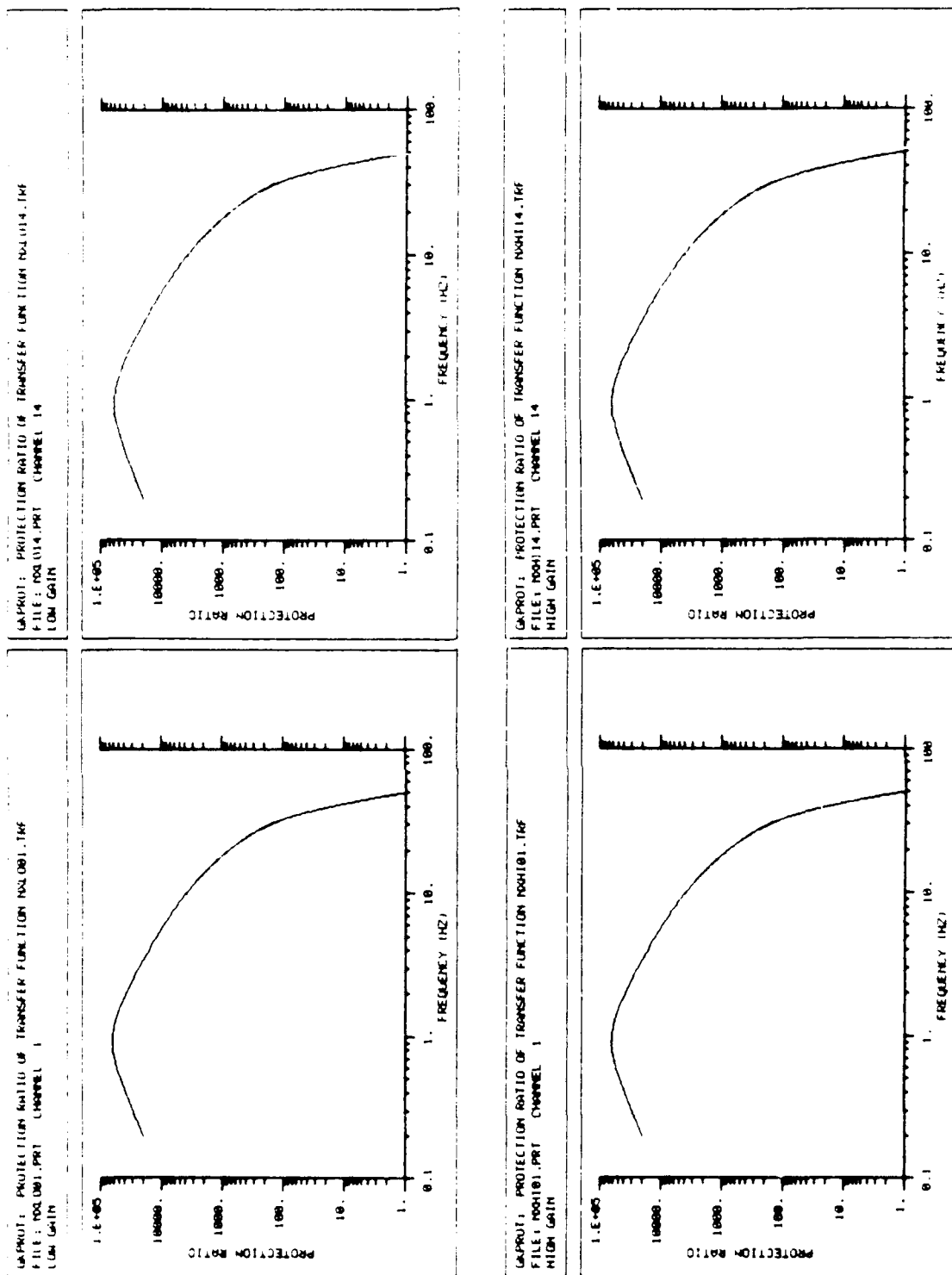


FIGURE 14

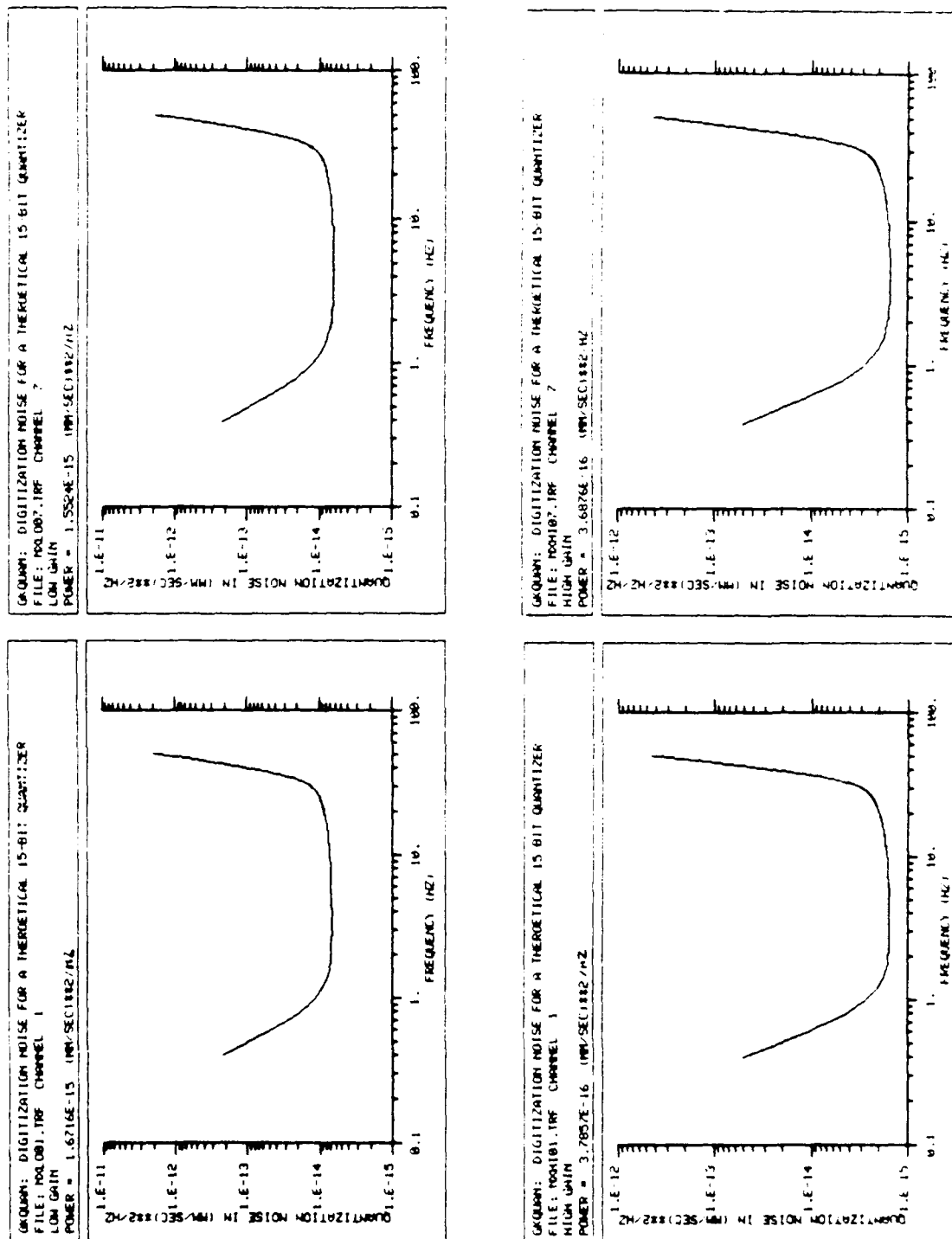


FIGURE 15

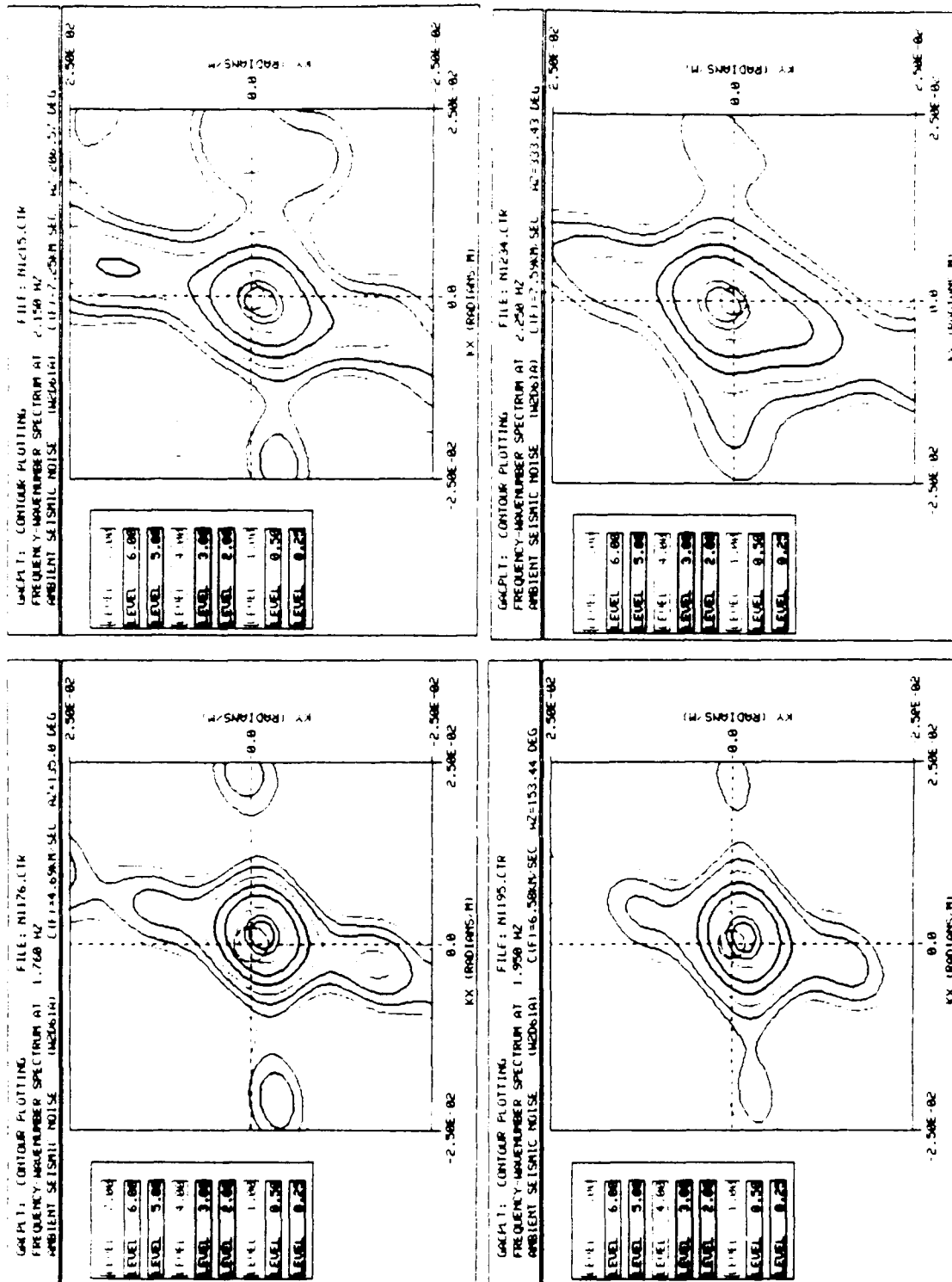


FIGURE 16

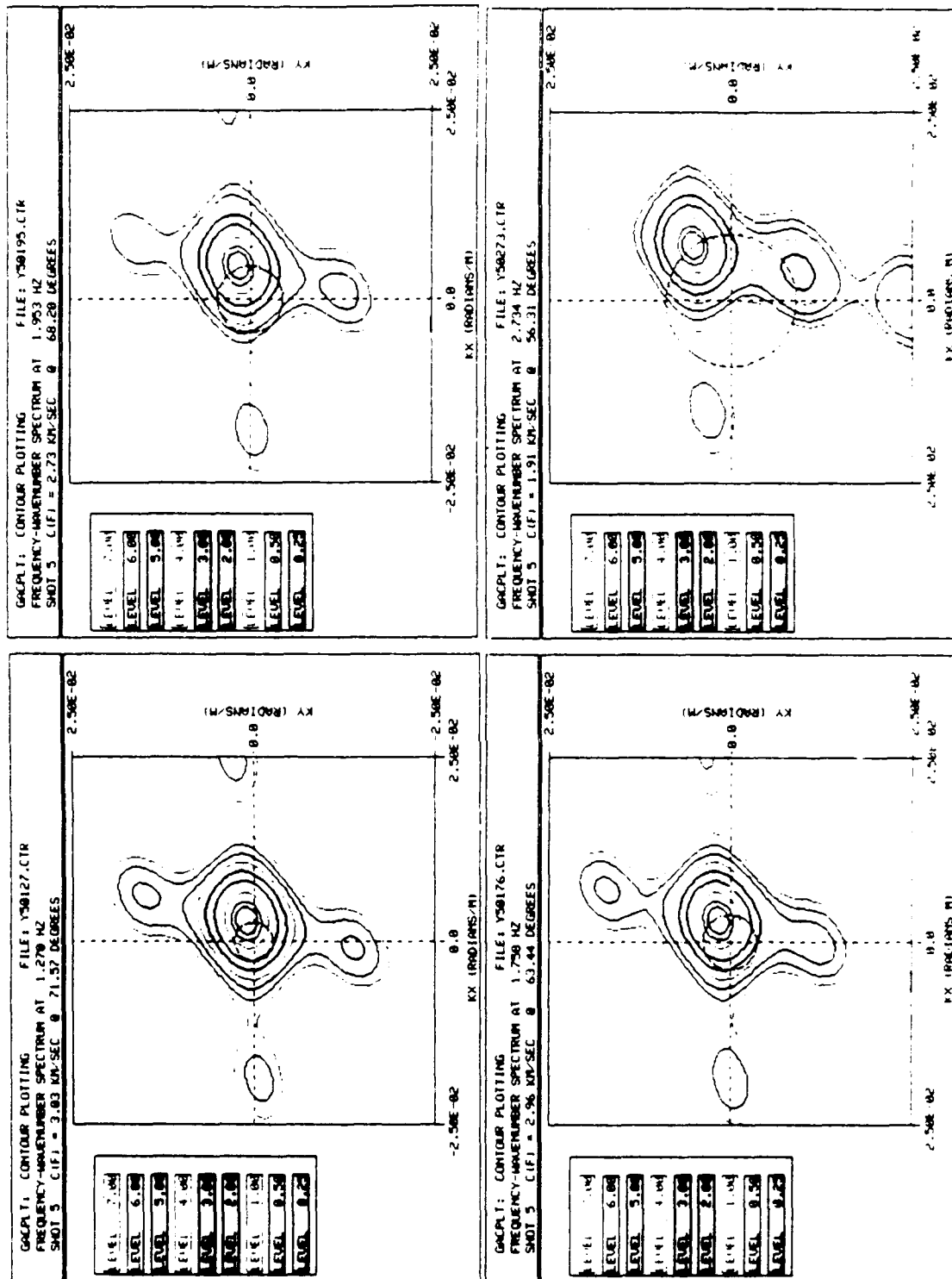


FIGURE 17

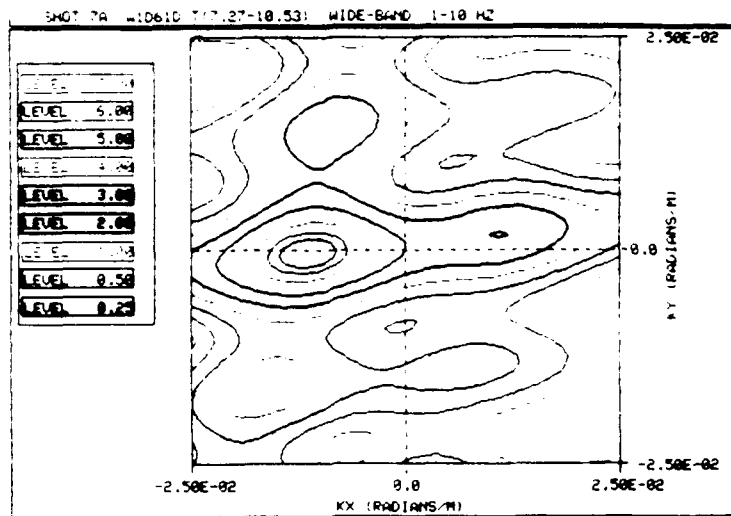


FIGURE 18A

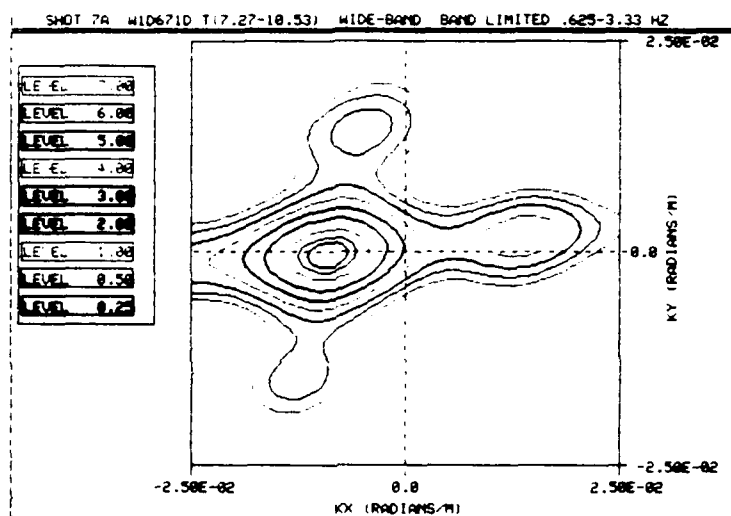


FIGURE 18B

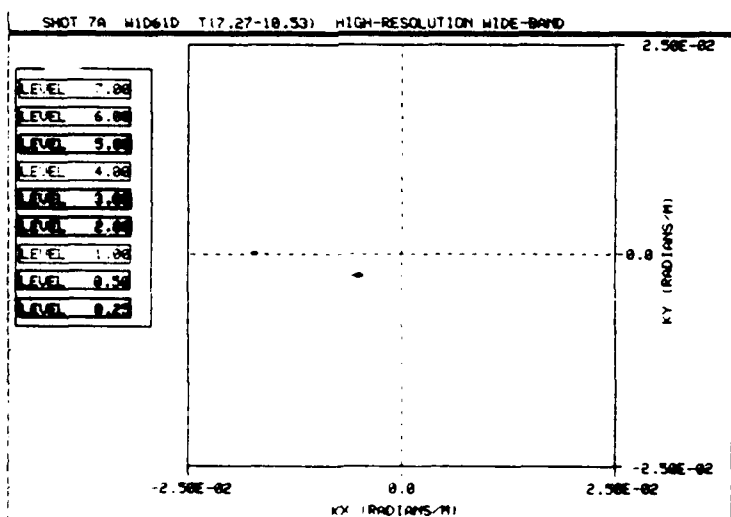


FIGURE 18C

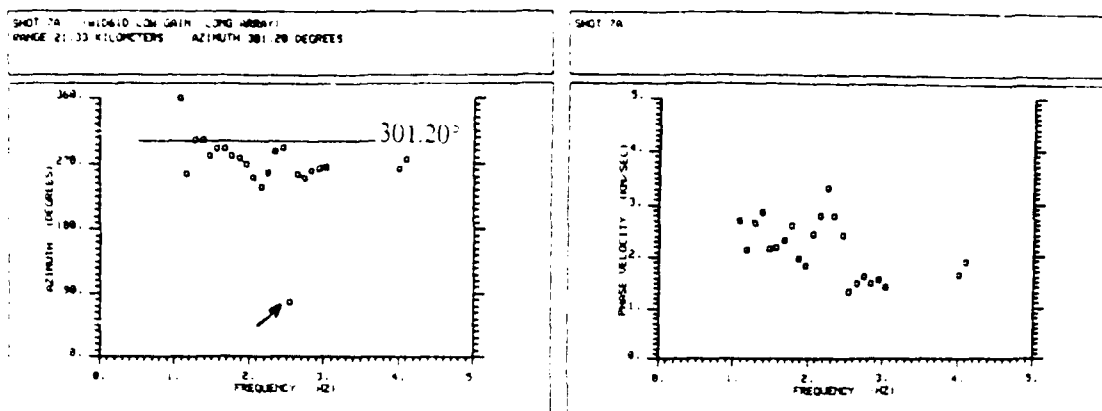


FIGURE 18D

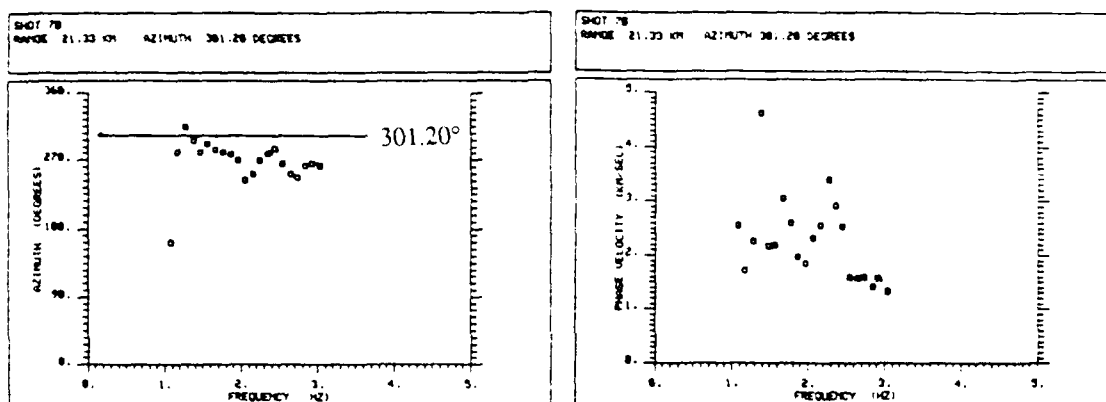


FIGURE 18E

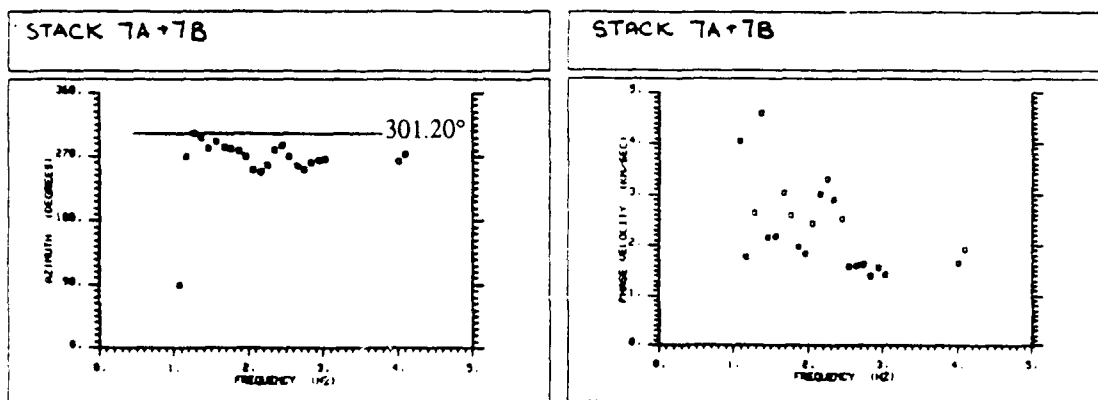


FIGURE 18F

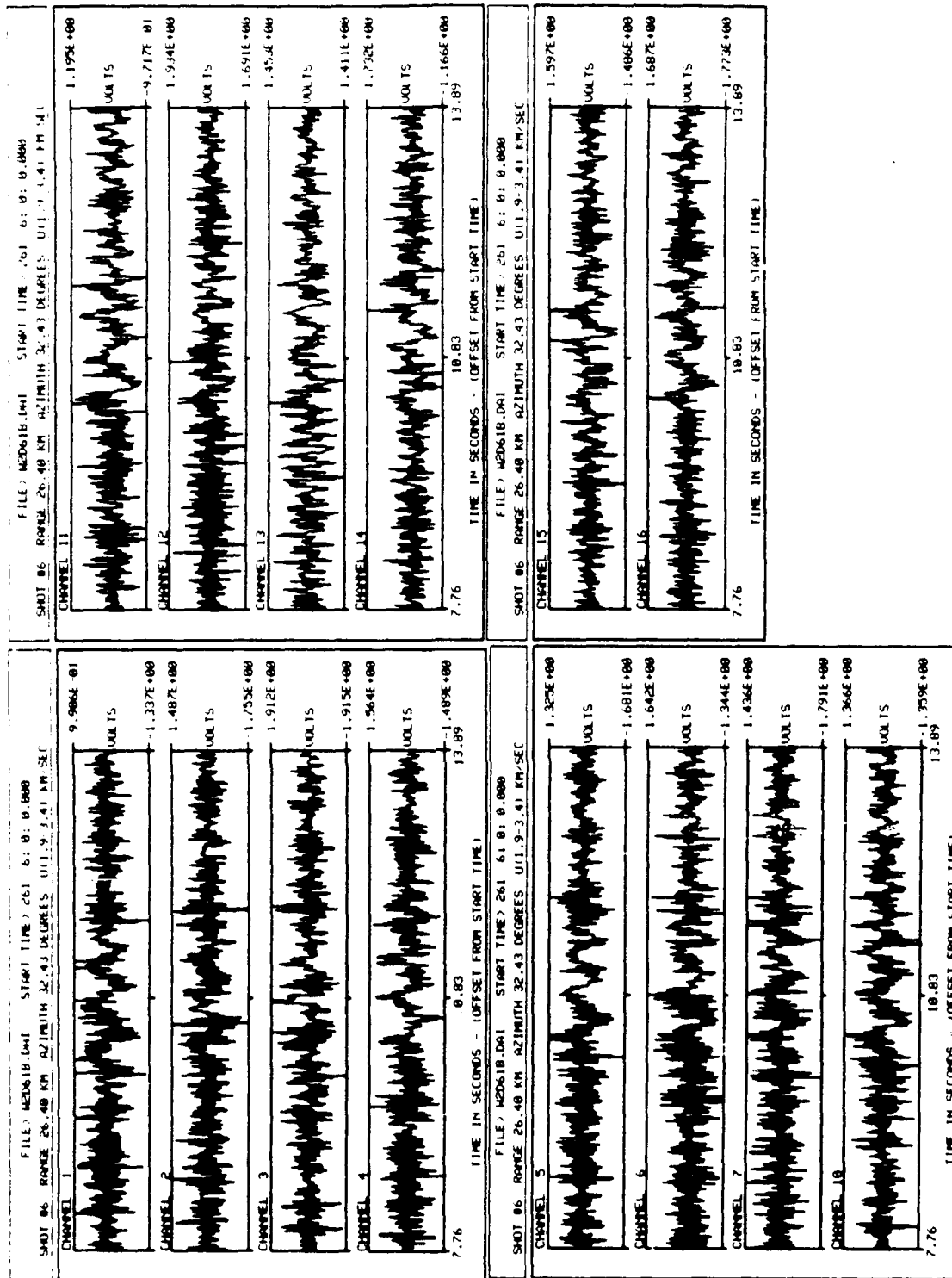


FIGURE 19A

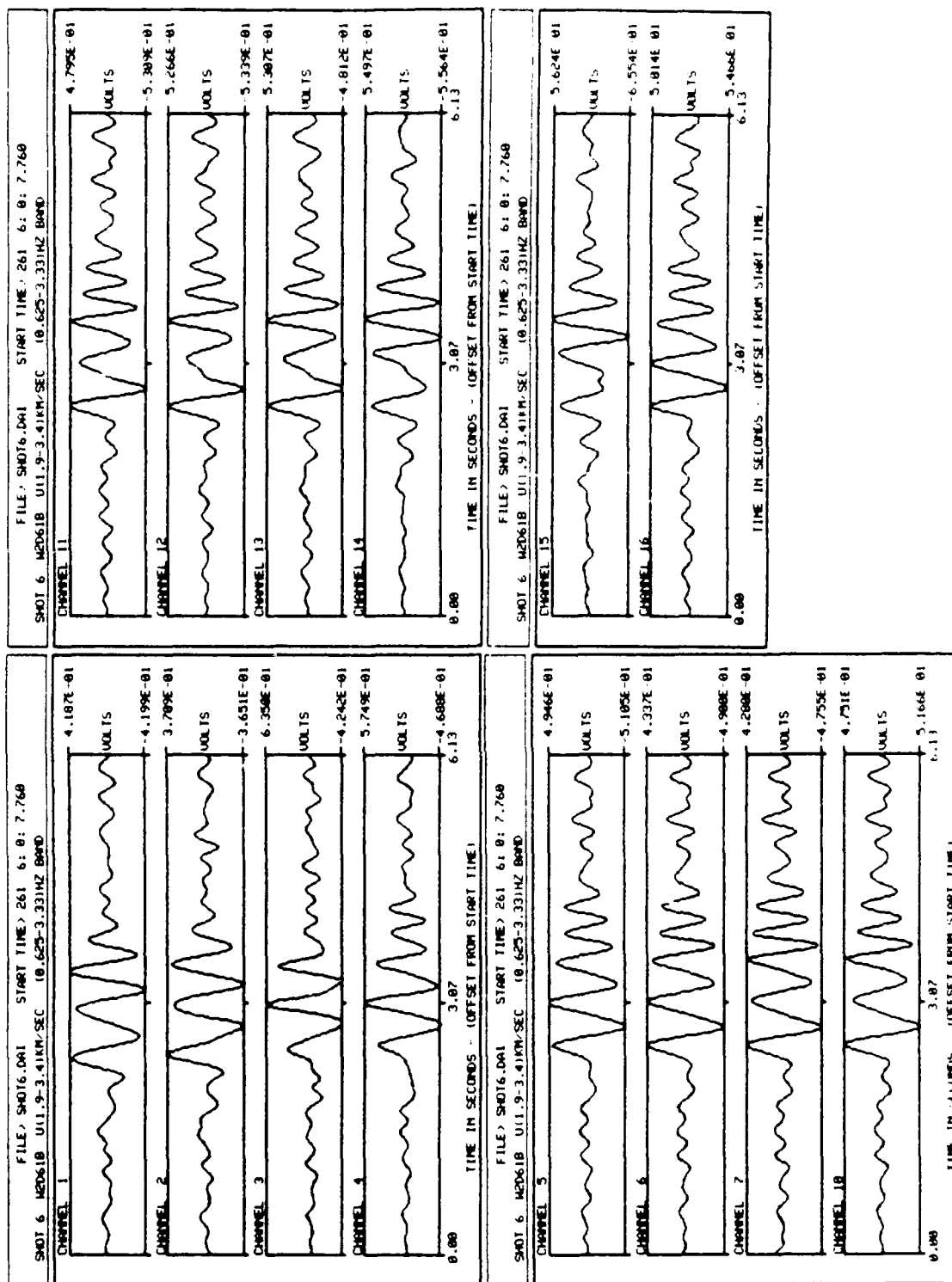


FIGURE 19B

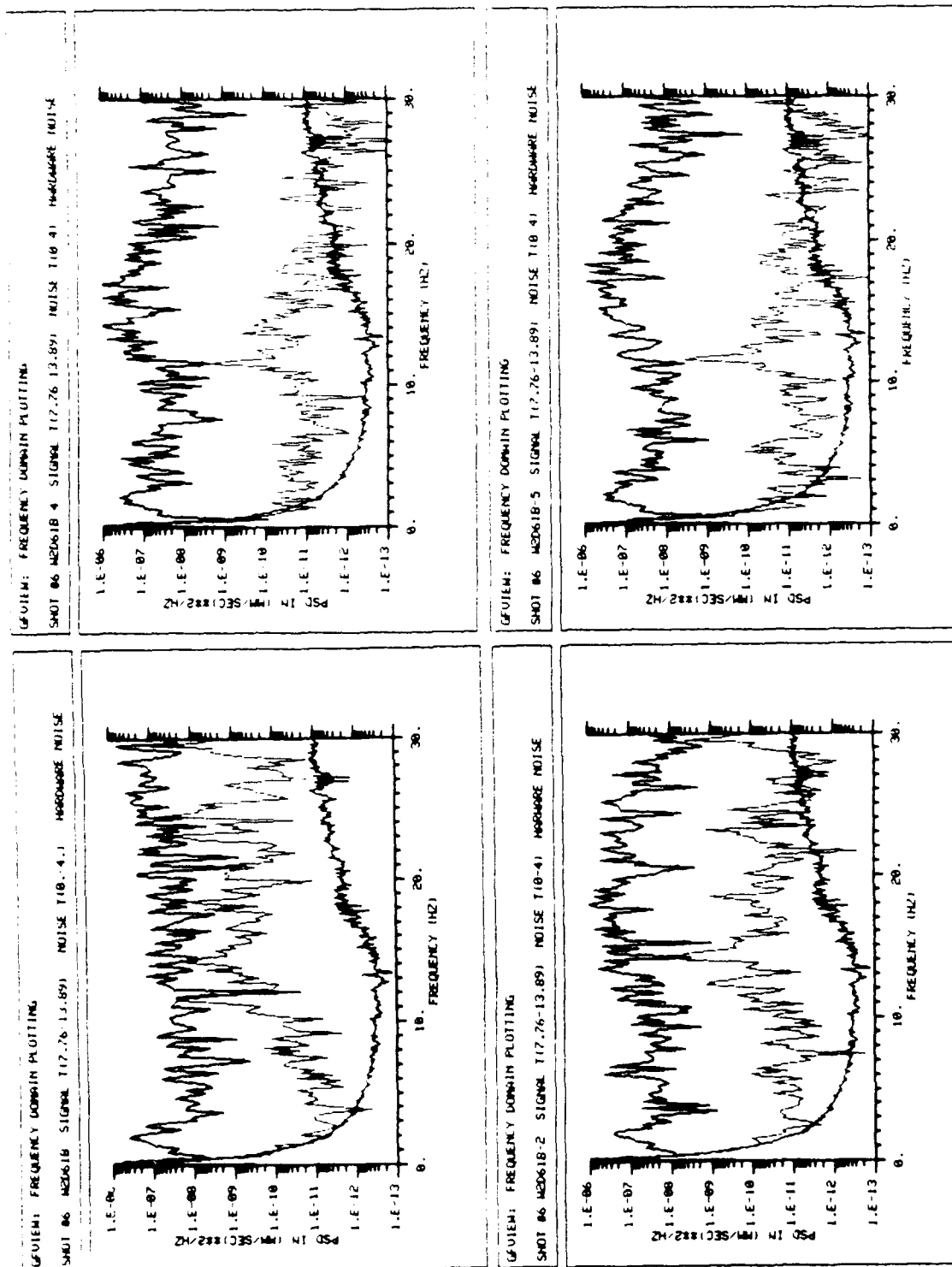


FIGURE 19C

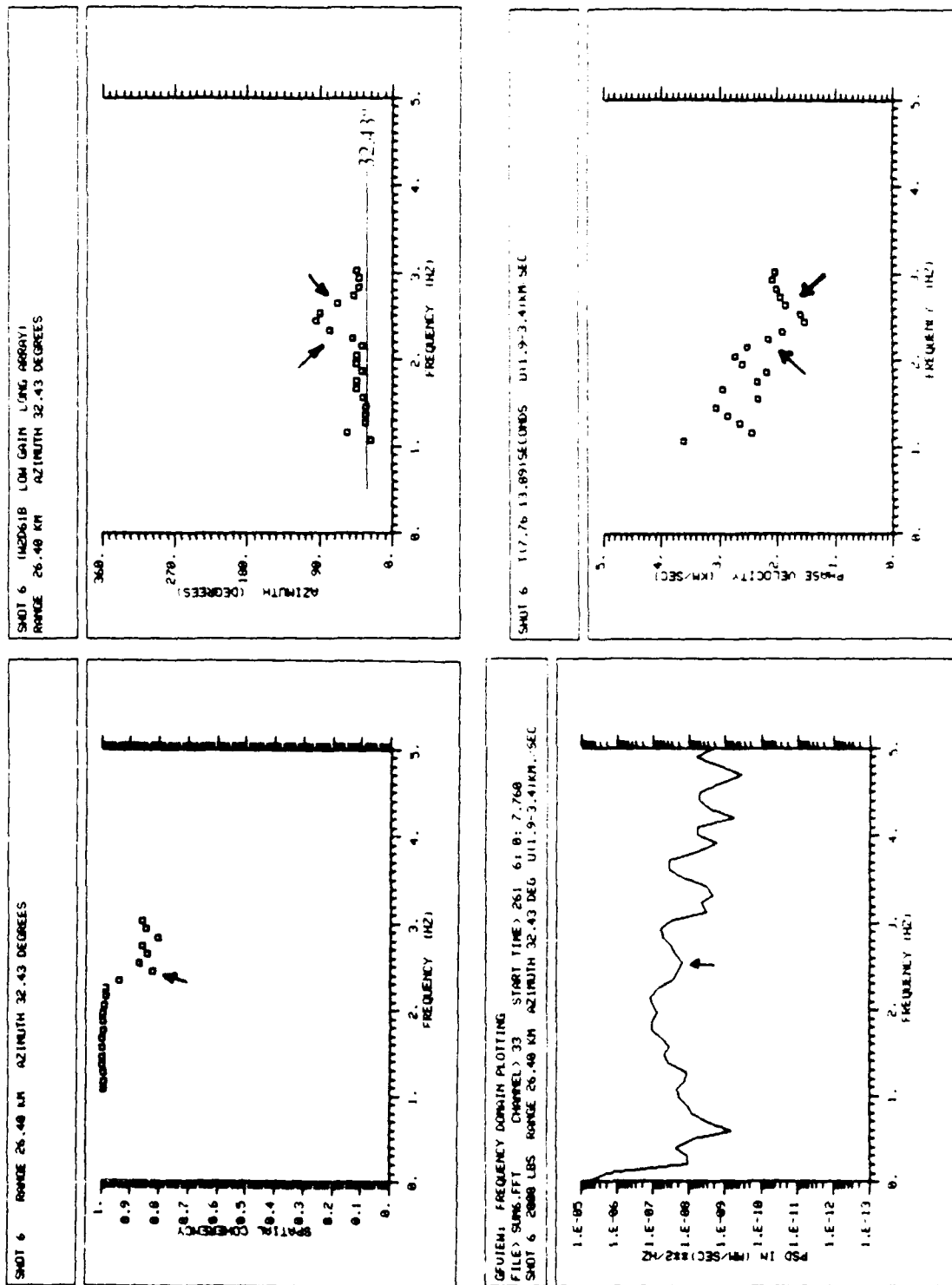


FIGURE 19D

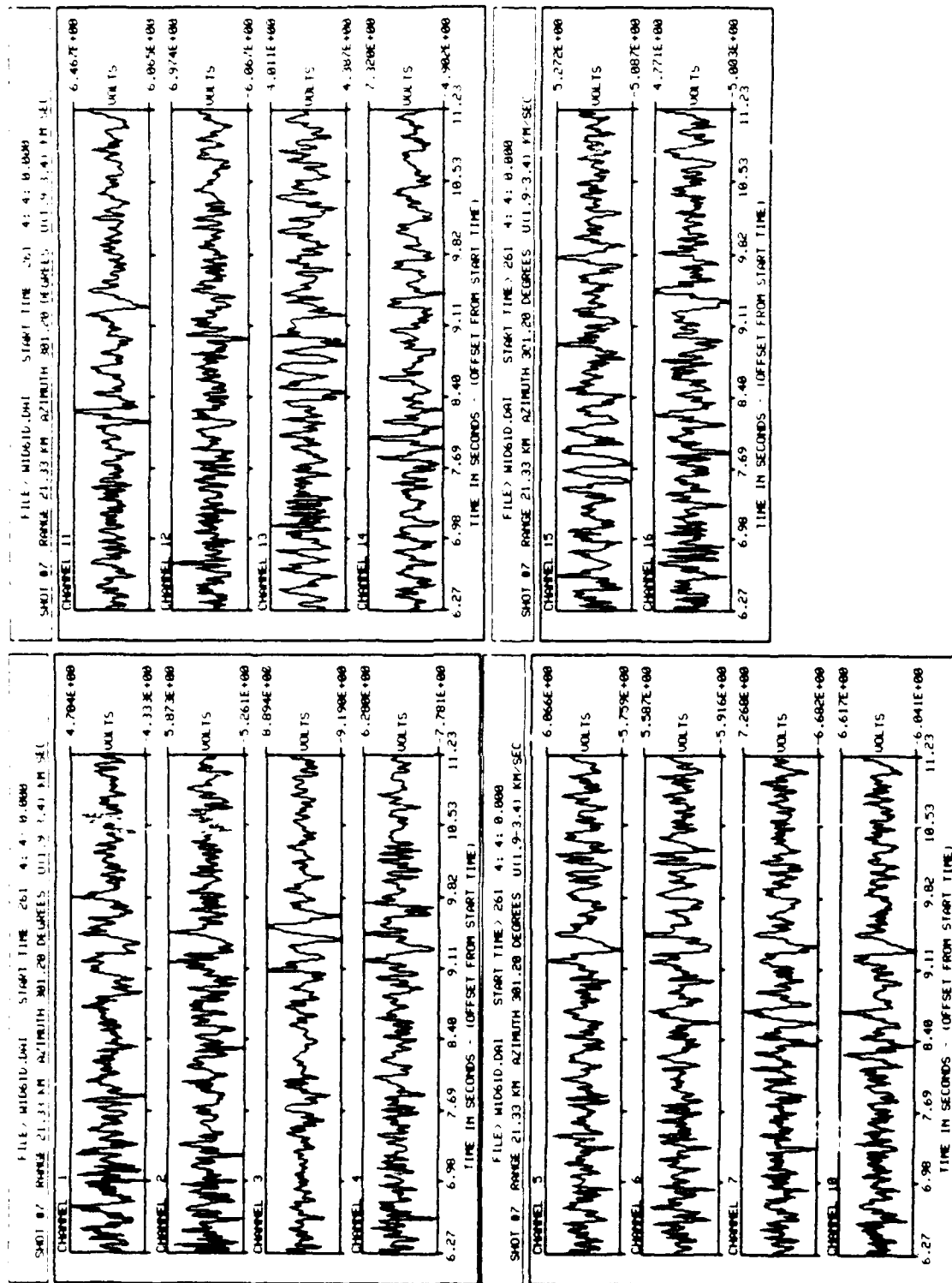


FIGURE 20A

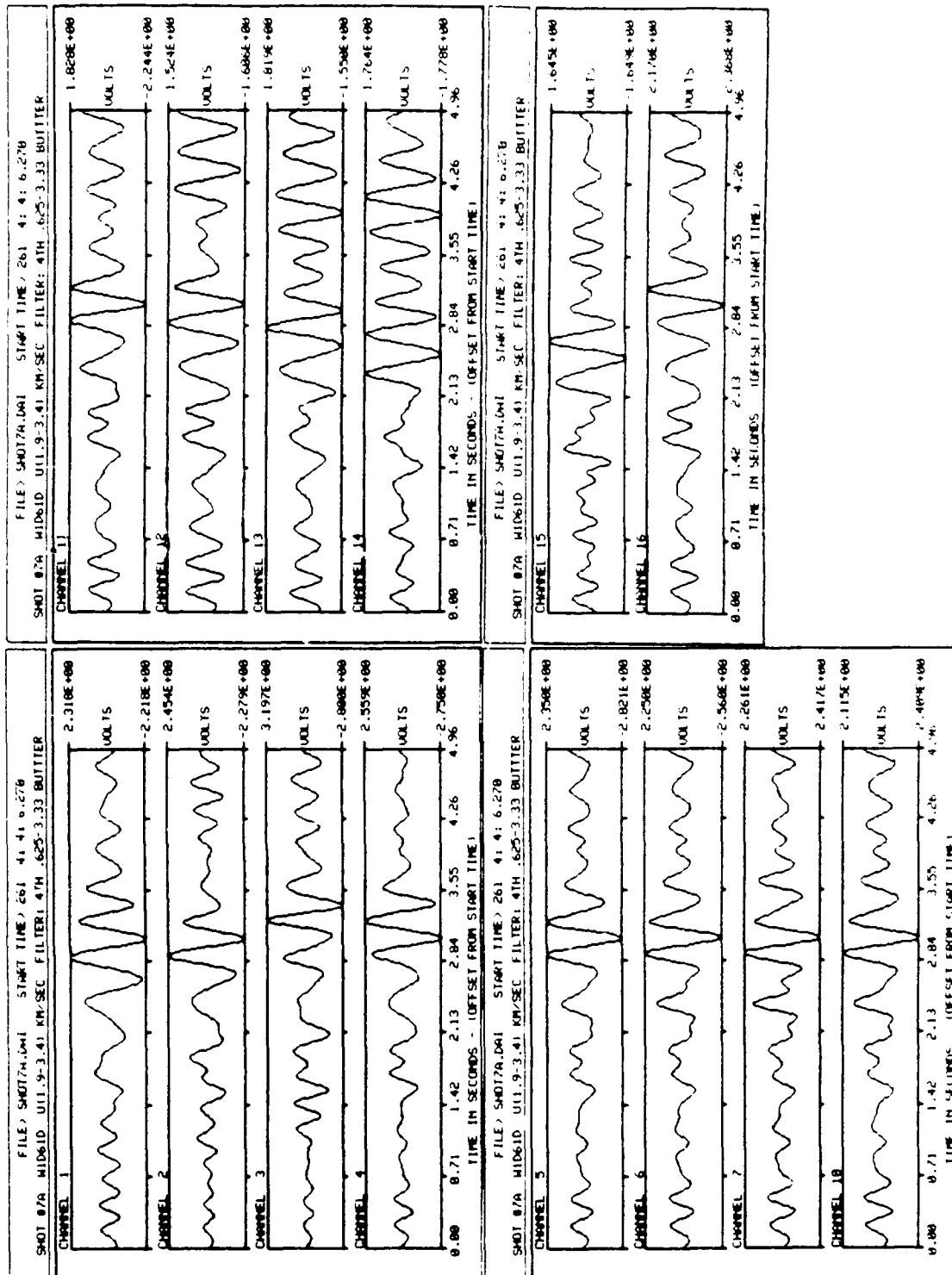


FIGURE 20B

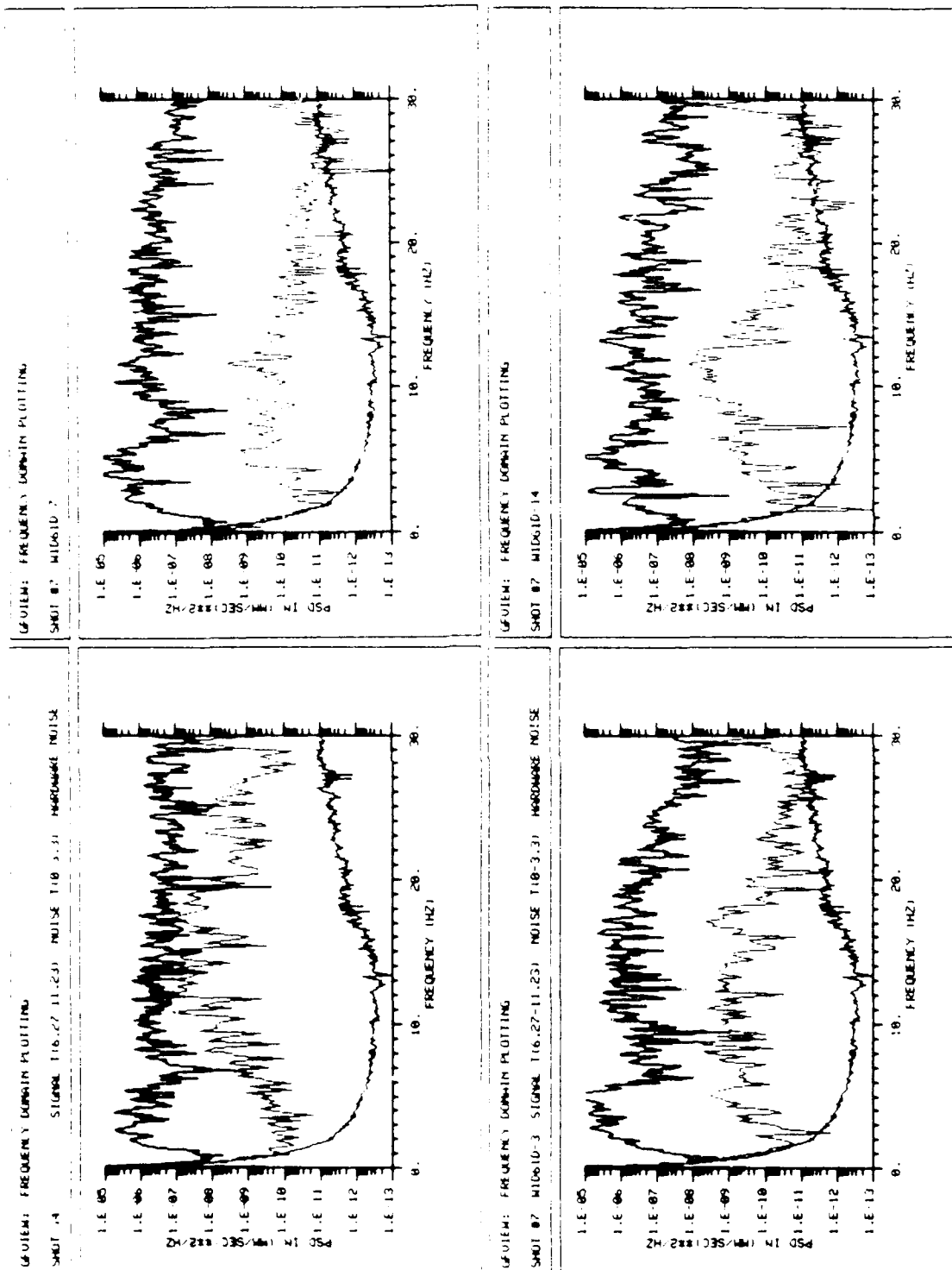
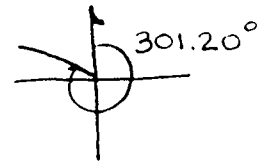
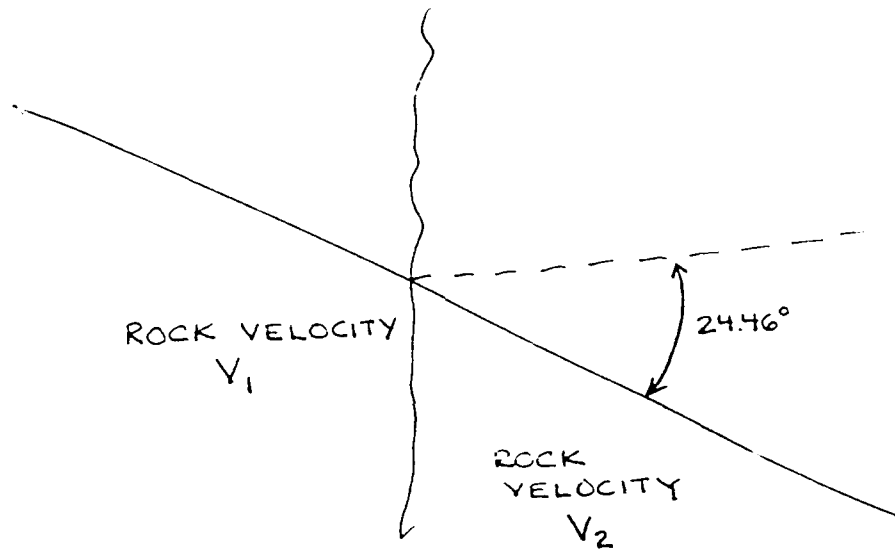
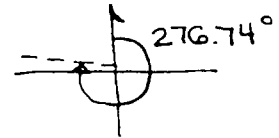


FIGURE 20C

TRUE AZIMUTH



F-K AZIMUTH



FOR A 25° ANGLE DEFLECTION, CONSIDER A 75° ANGLE OF INCIDENCE AND A 50° ANGLE OF REFRACTION.

$$\frac{\sin 75^\circ}{\sin 50^\circ} = 1.26 = \frac{V_1}{V_2} = \frac{3.0 \text{ km/sec}}{2.4 \text{ km/sec}}$$

FIGURE 21

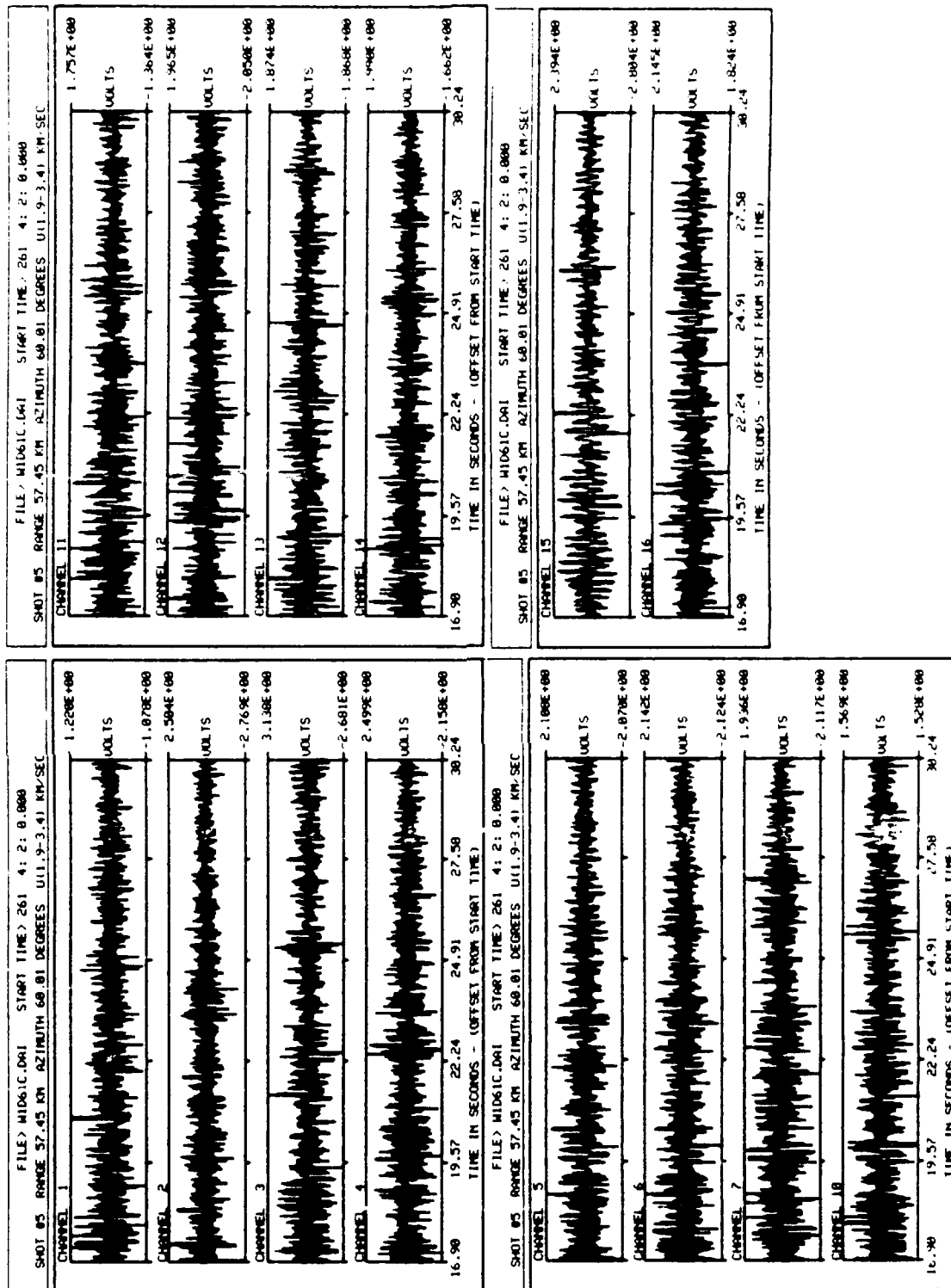


FIGURE 22A

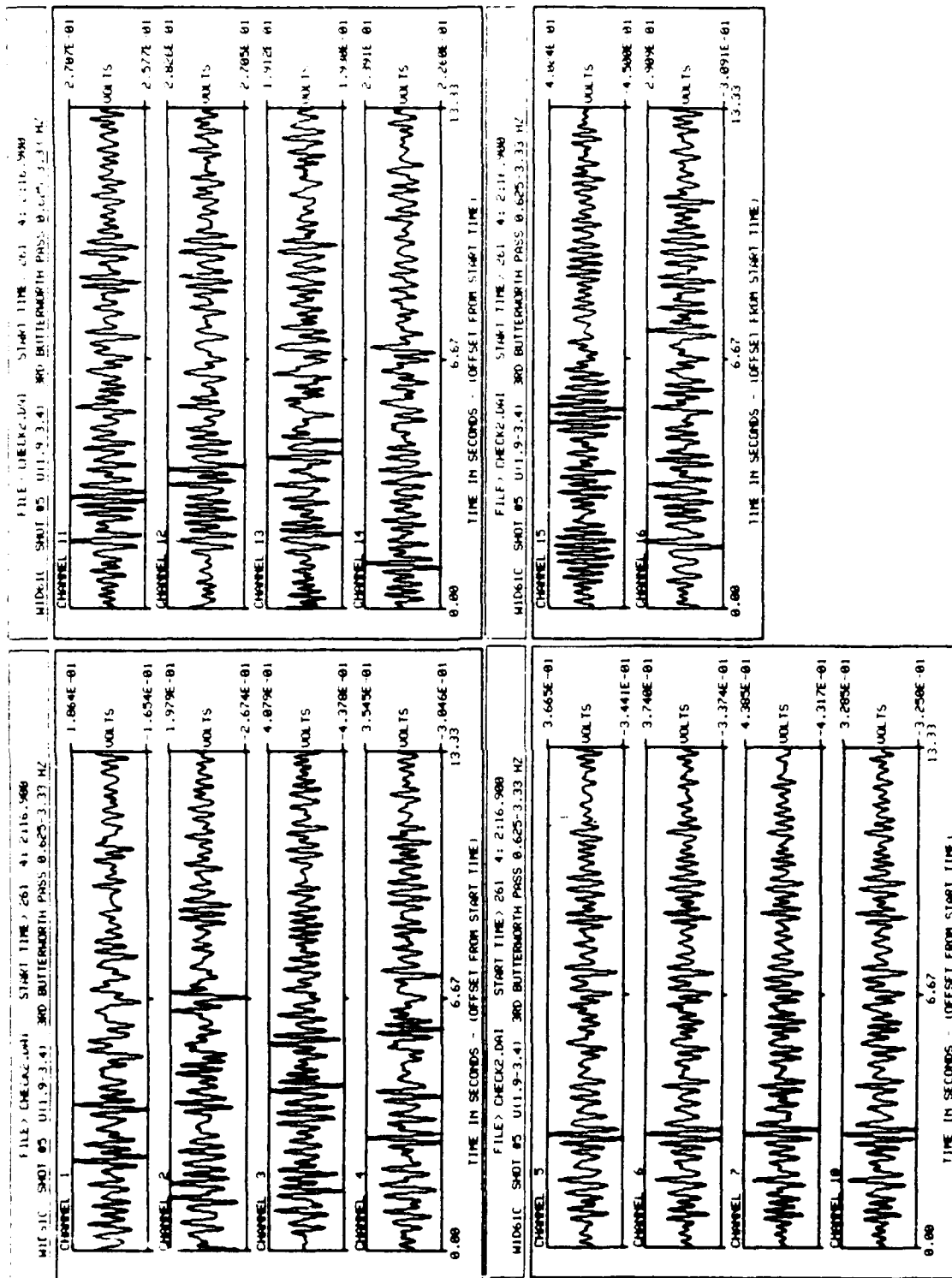


FIGURE 22B

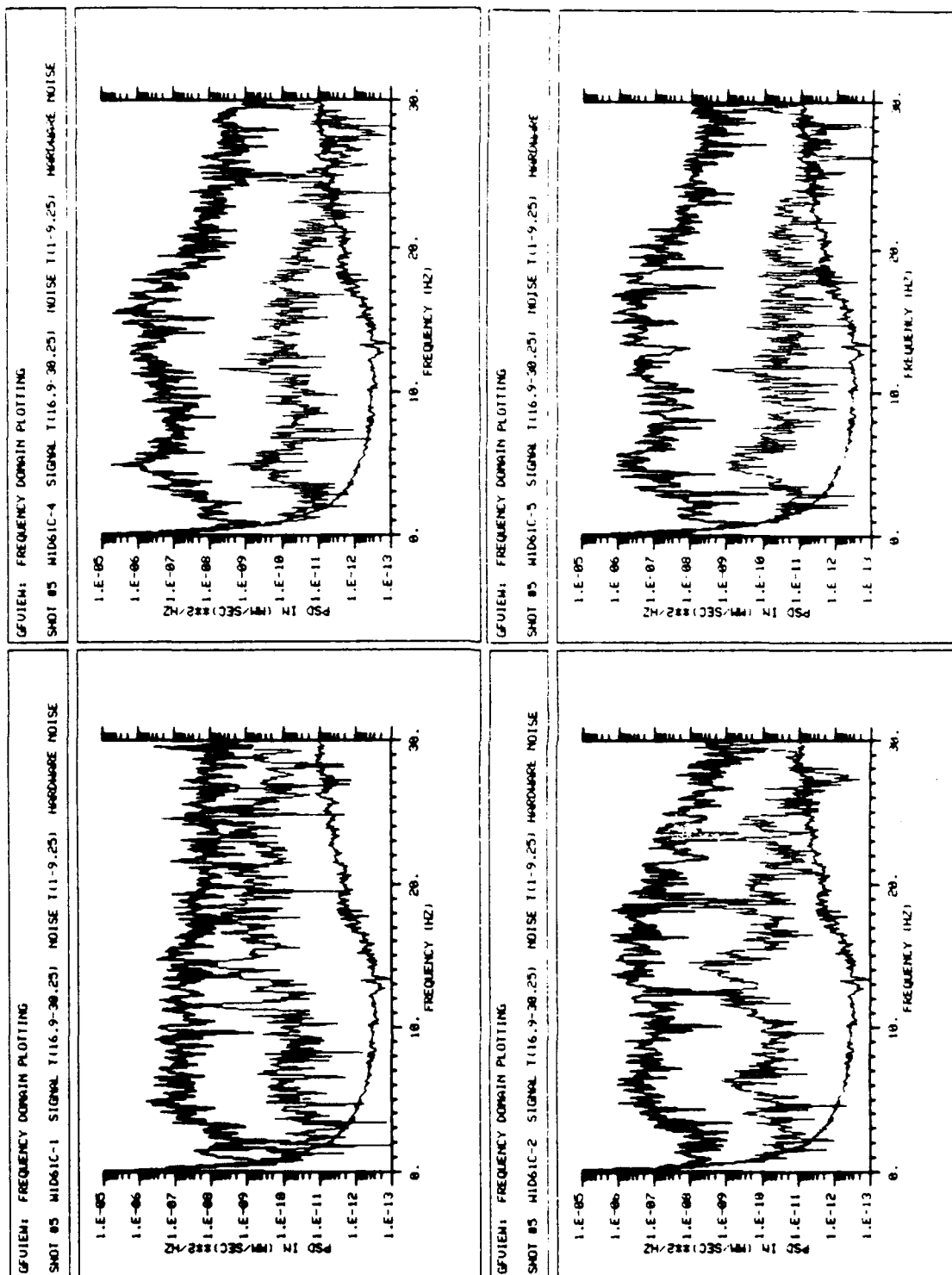


FIGURE 22C

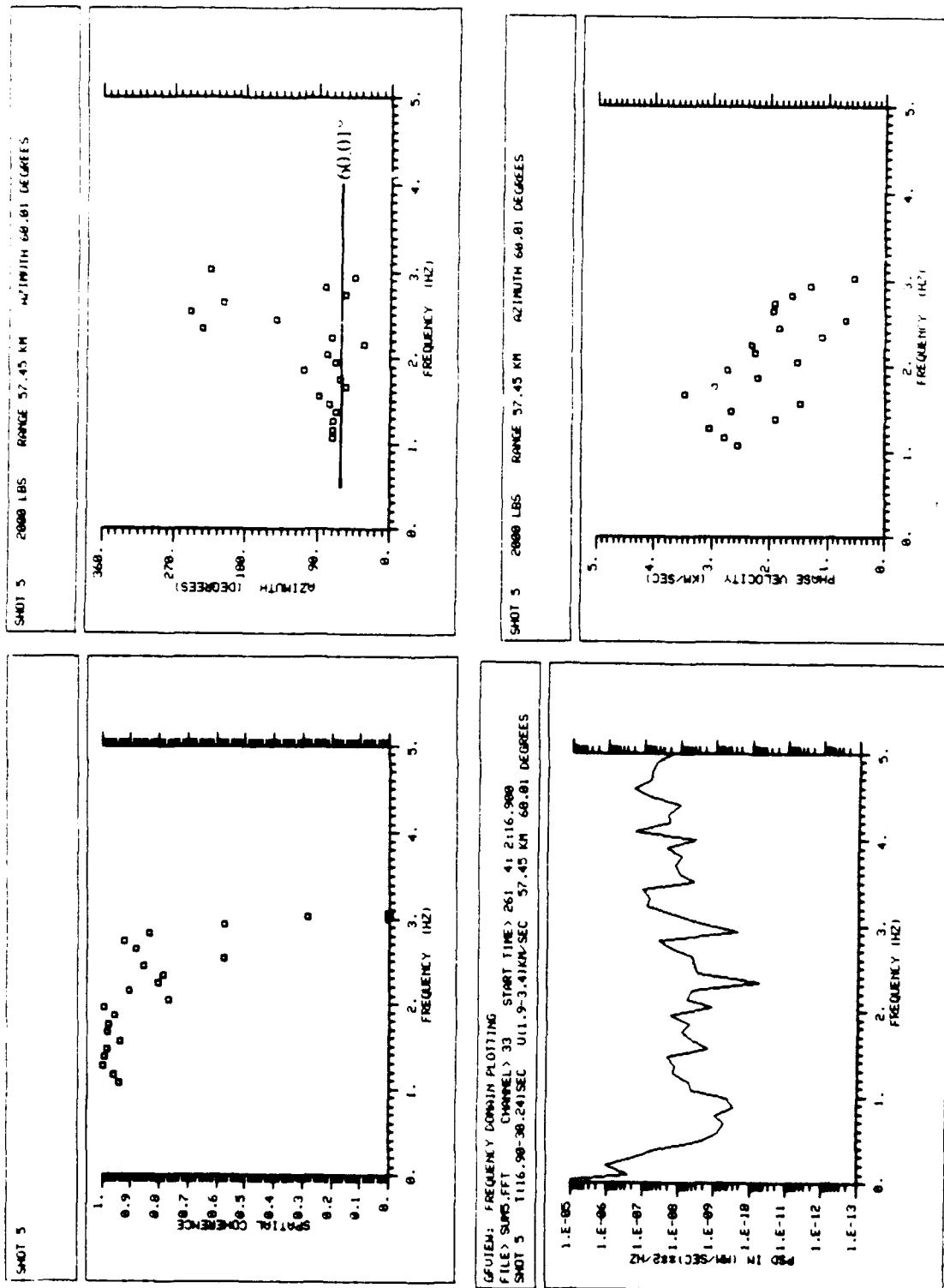


FIGURE 22D

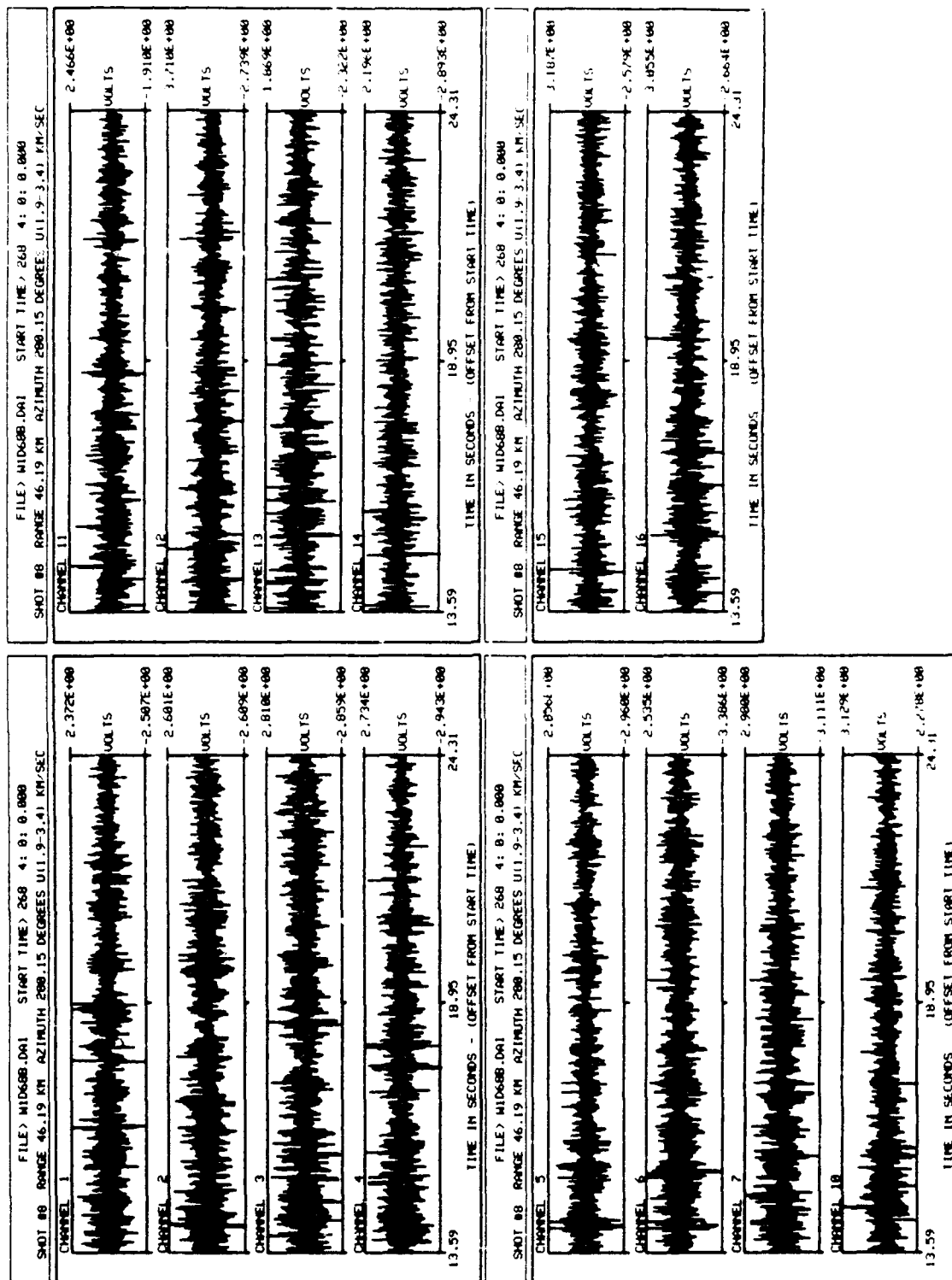


FIGURE 23A

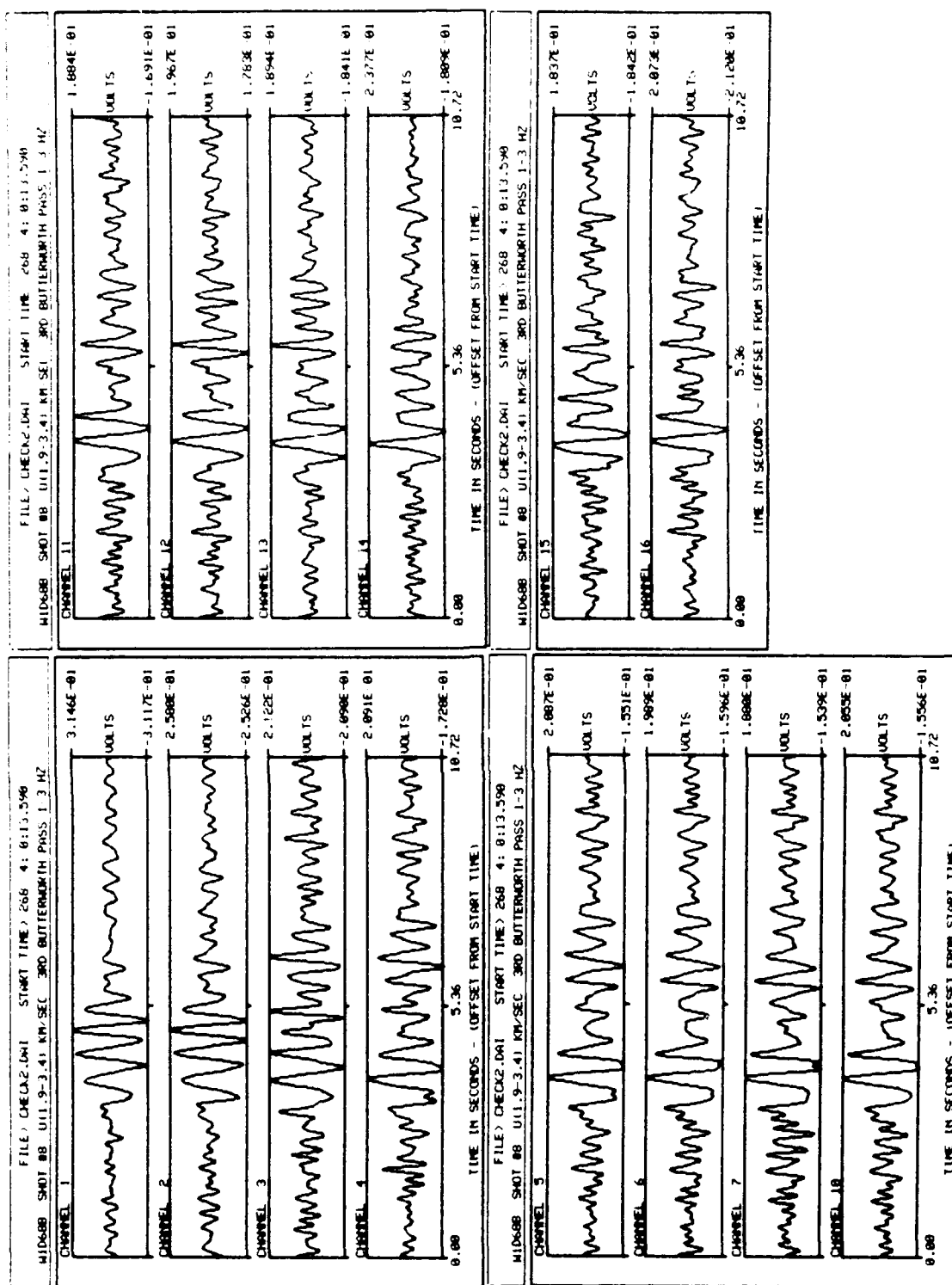


FIGURE 23B

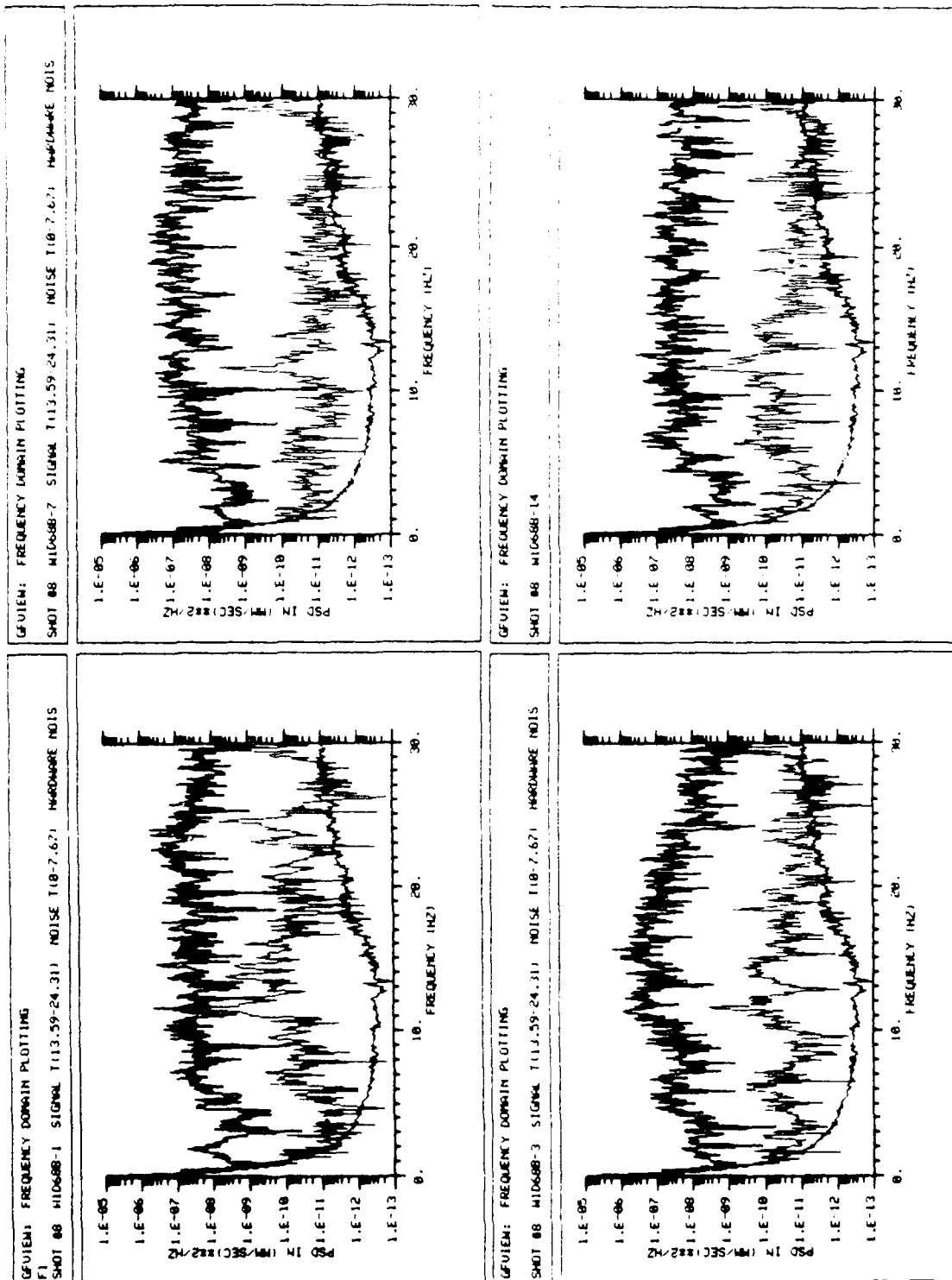


FIGURE 23C

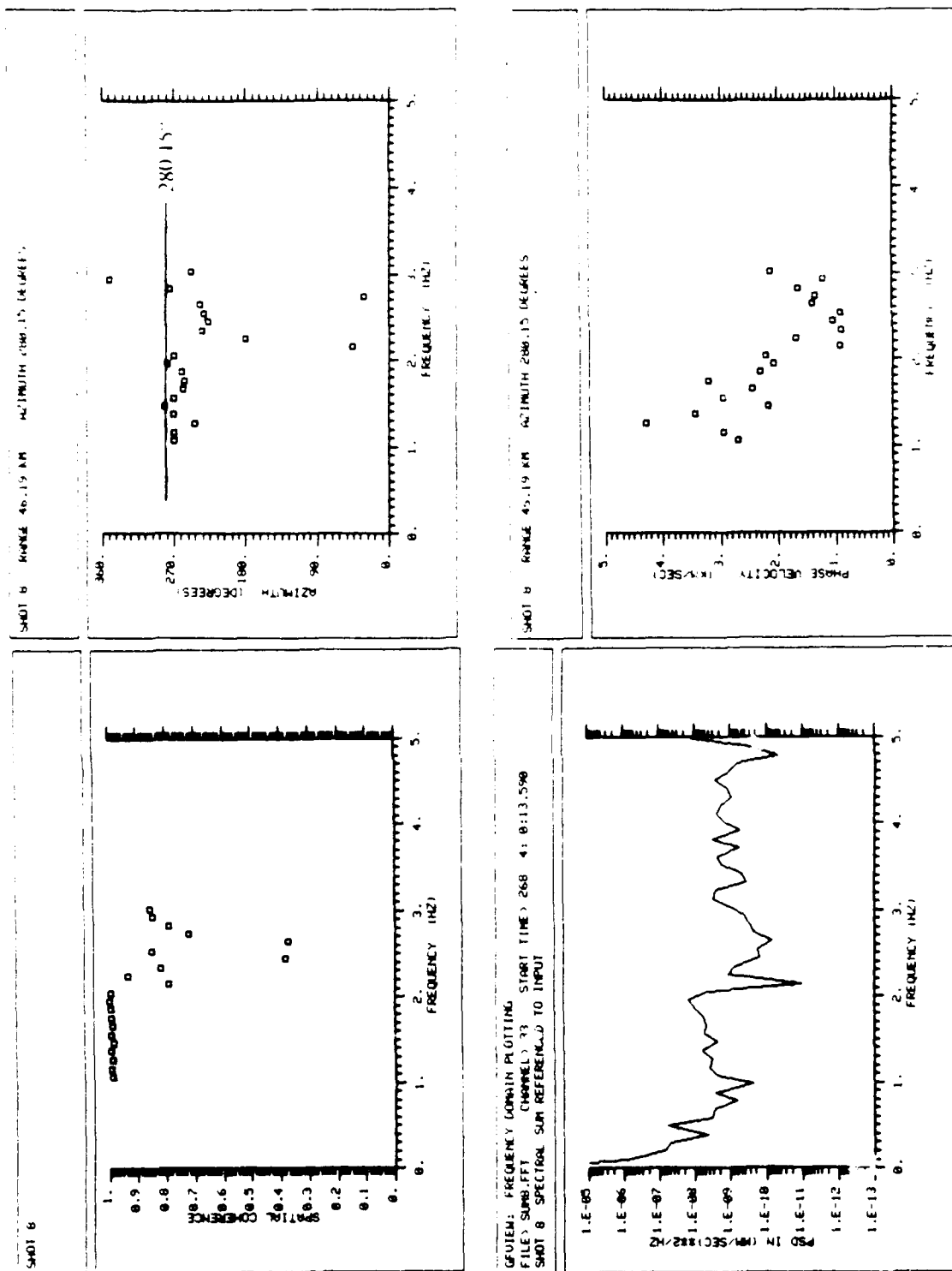


FIGURE 23D

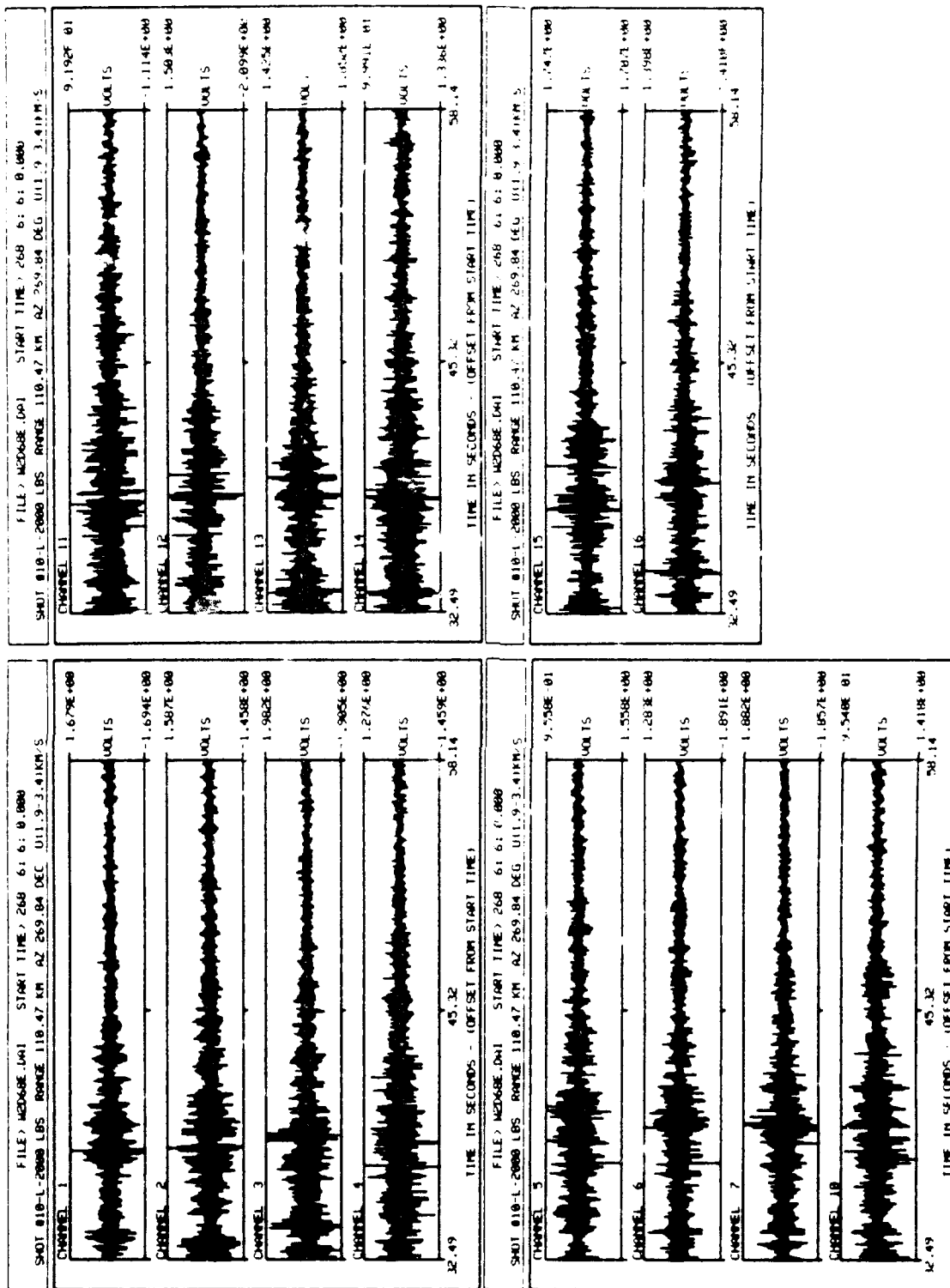


FIGURE 24A

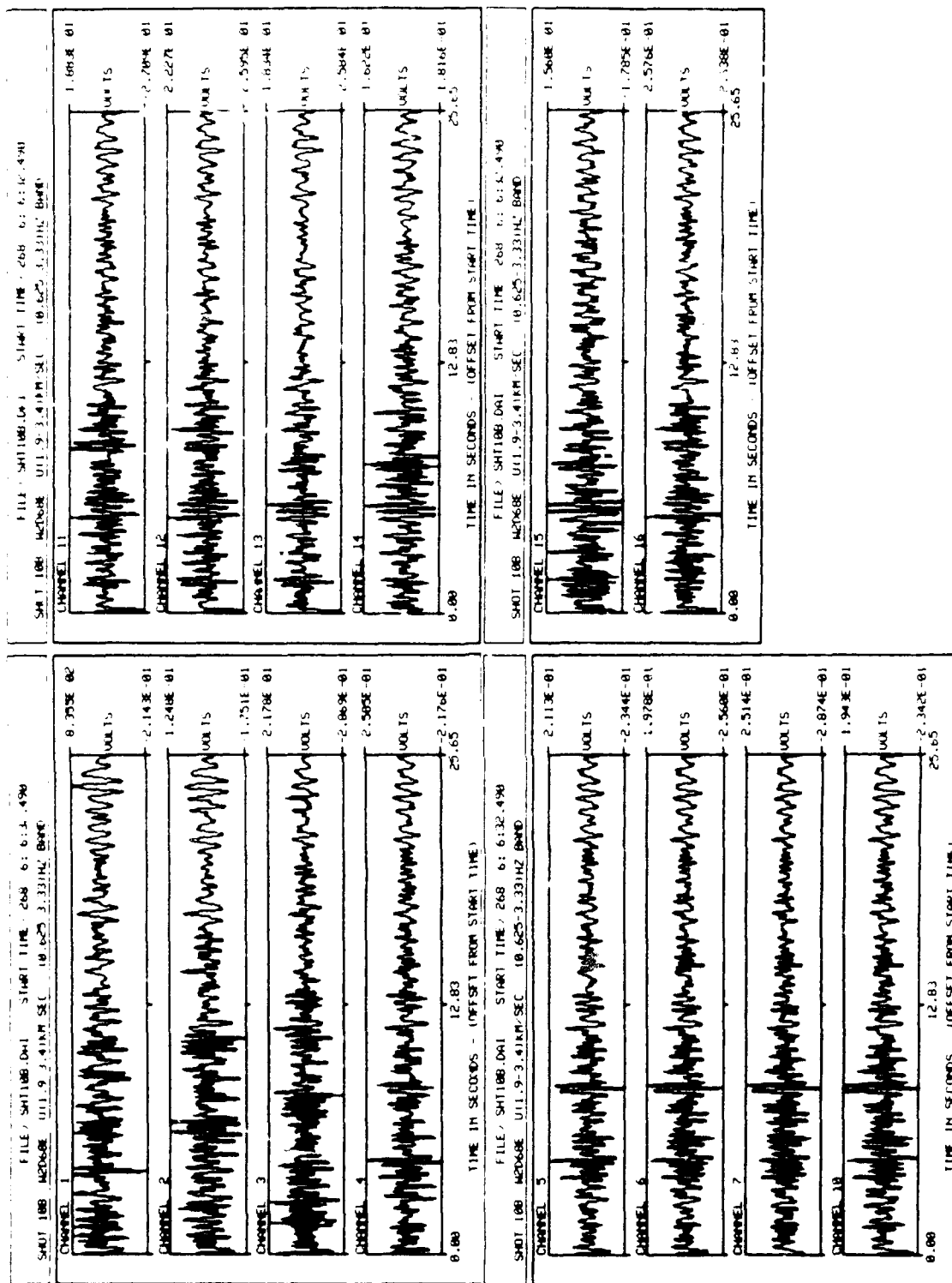


FIGURE 24B

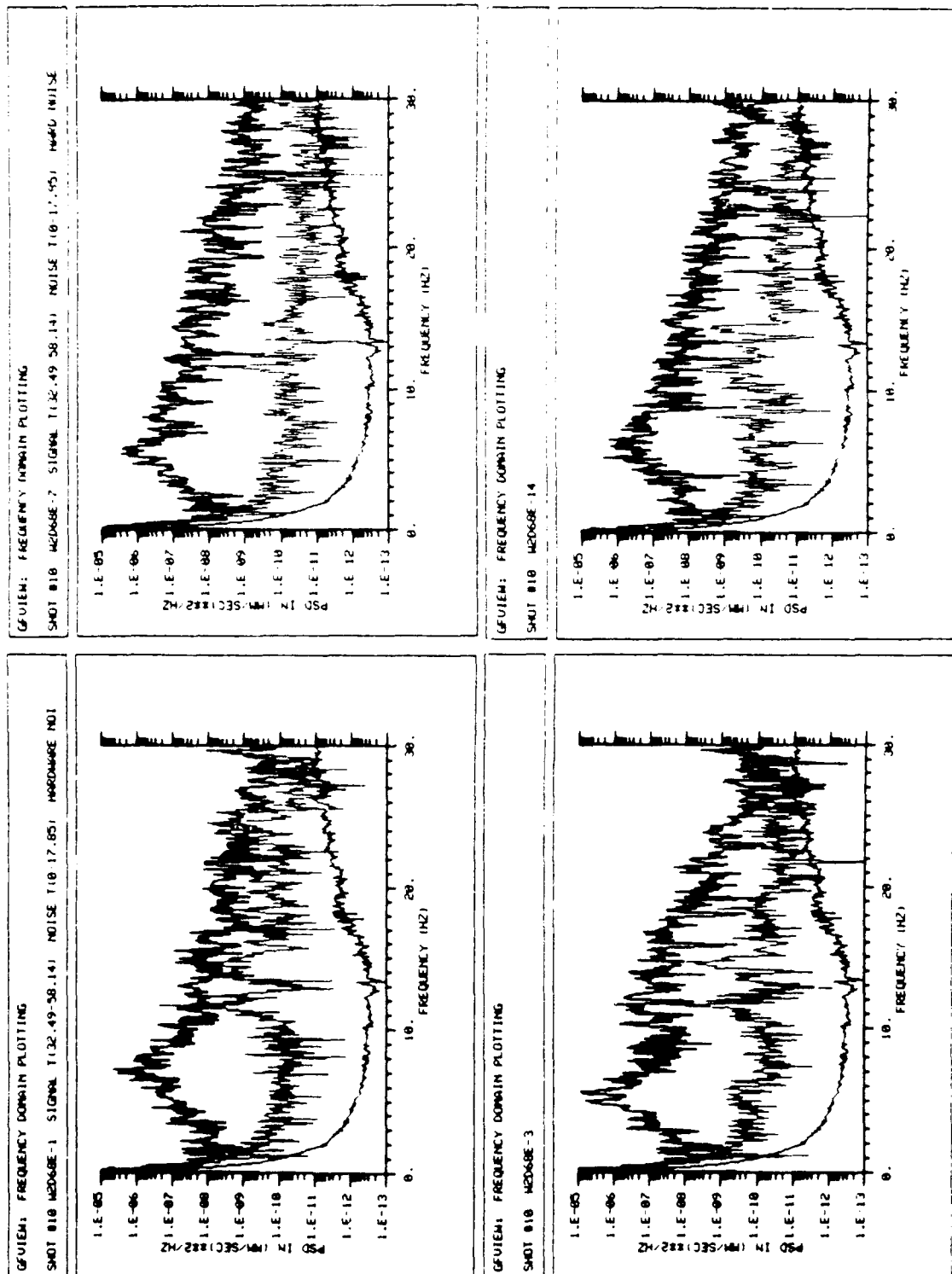


FIGURE 24C

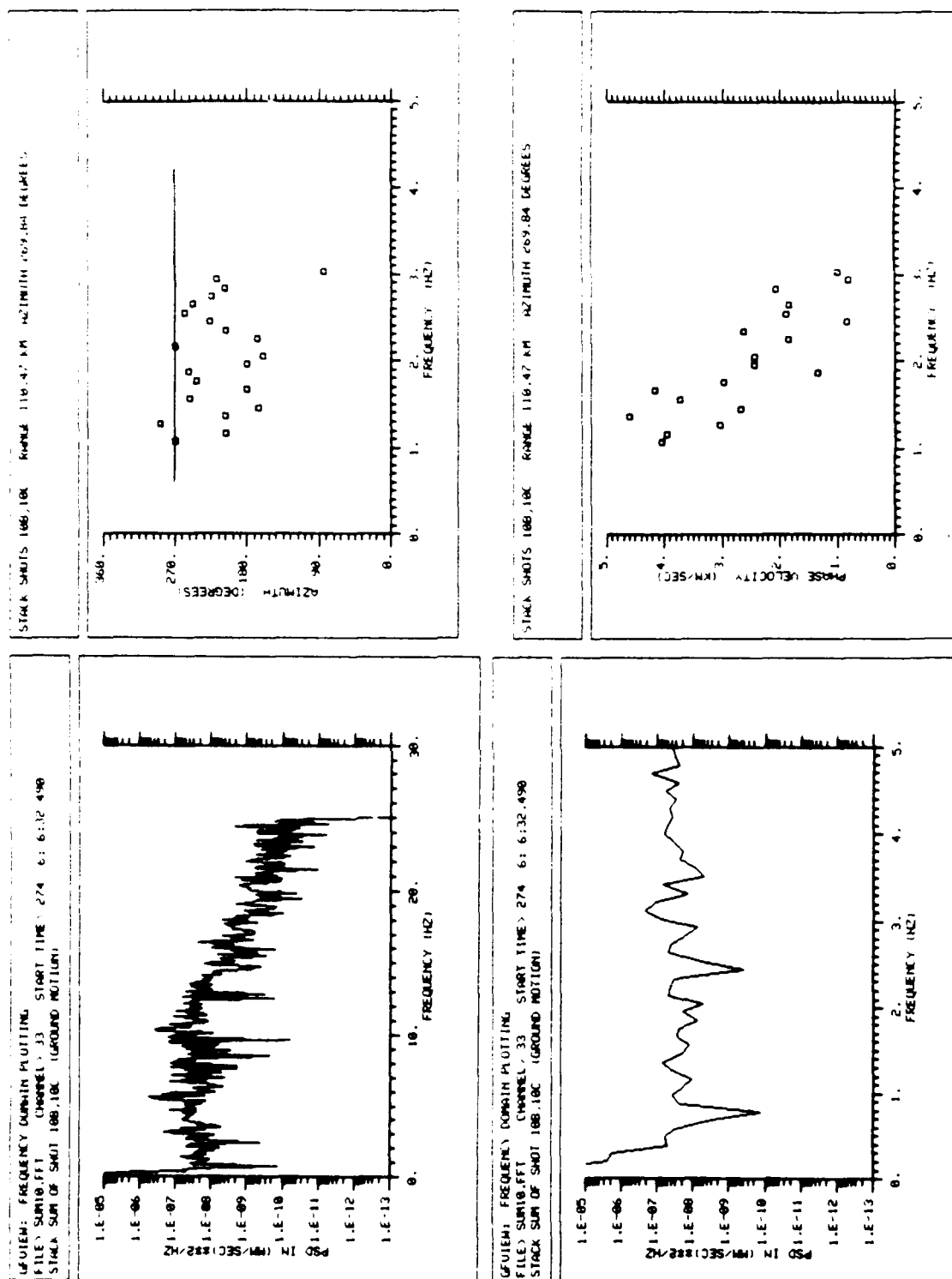


FIGURE 24D

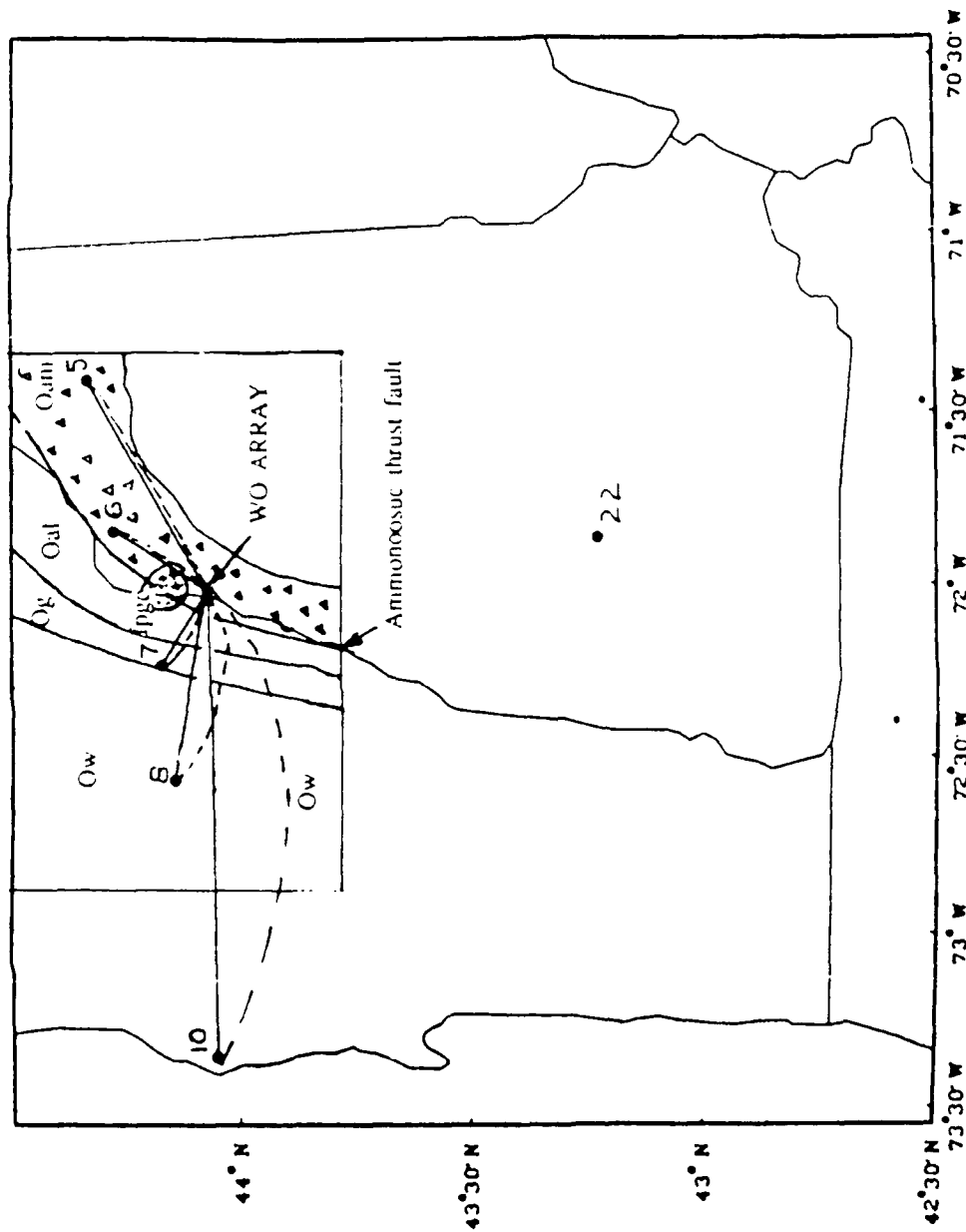


FIGURE 25

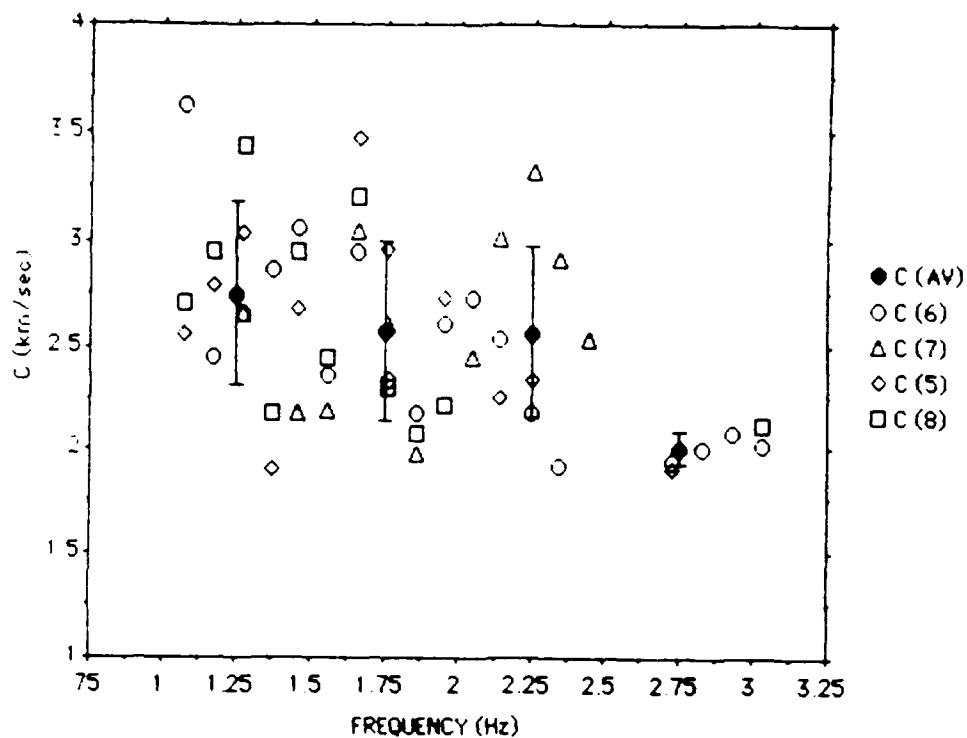


FIGURE 26

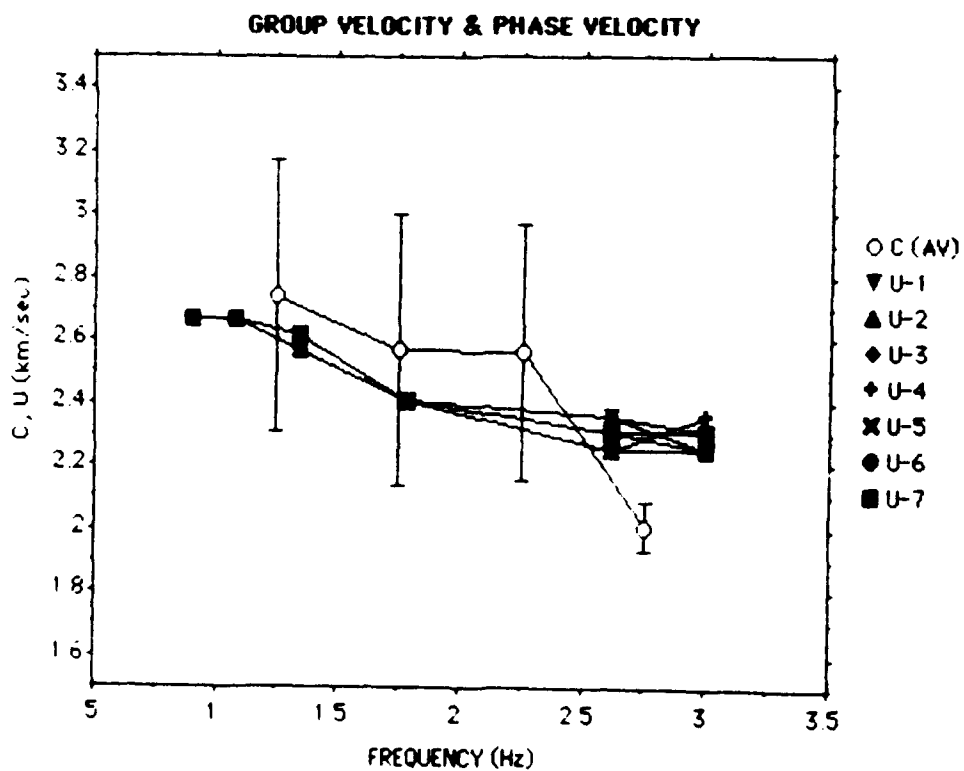


FIGURE 27